

**THE DEFORMATION RATE SENSITIVITIES OF  
ADDITIVELY AND CONVENTIONALLY  
FABRICATED 316L ALLOYS**

**A Thesis Submitted to  
the Graduate School of  
İzmir Institute of Technology  
in Partial Fulfillment of the Requirements for the Degree of**

**MASTER OF SCIENCE**

**in Mechanical Engineering**

**by  
Samed ENSER**

**December 2021  
İZMİR**

## ACKNOWLEDGMENTS

I would like to thank my thesis advisor, Prof. Mustafa GÜDEN for his constant support, fatherly patience, guidance and encouraging approach through the learning and writing process of my master thesis.

Secondly, I would like to express my thanks to especially Dr. Hakan YAVAŞ and the Turkish Aerospace Industry for providing the test samples used in this thesis and allowing us to use them.

More, I would like to thank all the members of DTM-Lab for their friendship, support and assistance throughout the life of my master's degree. Thanks to their making work entertaining, I didn't feel like I was working at all.

I wish to thank my family who deserves the better expression of my gratefulness for their endless support and prayers. This thesis is dedicated to my dear mother, Taibe GENÇER who supported me and affectionately raised me for the whole of my life. I would like to thank my father, Ali ENSER, is the person who always helped me, stand behind and directed me to be successful. Thanks a lot, my little brother Semih ENSER who has got a friend in me.

Last but not least, very special thanks go also to the many others that go unmentioned but have contributed in one way or another to the successful outcome of this work.

## ABSTRACT

### THE DEFORMATION RATE SENSITIVITIES OF ADDITIVELY AND CONVENTIONALLY FABRICATED 316L ALLOYS

The compression stress-strain behavior of a Scanning Laser Melt 316L (SLM-316L) and an annealed and extruded commercial 316L (C-316L) were determined between  $1 \times 10^{-3} \text{ s}^{-1}$  and  $2500\text{-}3150 \text{ s}^{-1}$ . SLM-316L deformed by twinning and slip, while C-316L by martensitic transformation and slip with no fracture until about 0.51 strain. The higher yield strength of SLM-316L than C-316L was attributed to the higher dislocation density of SLM-316L. The higher work hardening rate of C-316L alloy was proved due to the higher resistance of martensite plate than twin boundary to the dislocation motion. As the strain rate increased, both alloys showed increased flow stresses. However, the rate sensitivities declined as the strain increased due to the adiabatic heating at high strain rates. The Johnson and Cook flow stress material models of both alloys were further determined for the adiabatic and isothermal conditions. The martensite formation in C-316L specimens and twinning formation in SLM-316L alloys decreased at high strain rates compared to quasi-static strain rates. The XRD spectra of C-316L also confirmed the reduced martensite formation at high strain rates. The reduced twin and martensite formation at high strain rates were attributed to the increased stacking fault energy due to the adiabatic heating of the test specimens. The increase of stacking fault energy at high strain rates promoted a higher fraction of the deformation by slip. Lastly, the reloading tests revealed a strain-rate history effect in SLM-316L and no strain-rate history effect in C-316L.

## ÖZET

### EKLEMELİ VE GELENEKSEL YÖNTEMLE ÜRETİLEN 316L ALAŞIMLARININ DEFORMASYON HIZI HASSASİYETLERİ

Seçici Lazer Ergitme yöntemi ile eklemeli olarak üretilmiş 316L (SLM-316L) ve ekstrüde edilmiş-tavllanmış ticari 316L (C-316L) alaşımlarının basma testi altındaki gerilim-gerinim davranışı, statik ( $1 \times 10^{-3} \text{ s}^{-1}$ ) ve dinamik ( $2500\text{-}3150 \text{ s}^{-1}$ ) hızlar arasında belirlendi. SLM-316L, ikizlenme ve kayma yoluyla deforme olurken, C-316L martenzitik dönüşümle deforme olmuştur ve her iki alaşım da yaklaşık 0,51 gerinim değerine kadar kırılma olmadan deforme olmuşlardır. SLM-316L'nin C-316L'den daha yüksek akma dayanımı, SLM-316L'nin daha yüksek dislokasyon yoğunluğuna atfedilmiştir. C-316L alaşımının daha yüksek pekleşme (iş sertleşmesi) hızı, martenzit plakalarının, dislokasyon hareketine karşı, ikiz sınırlarına kıyasla, daha yüksek direnç göstermesine atfedilmiştir. Gerinim hızı arttıkça, her iki alaşımın akış gerilmelerinde artış görülmüştür. Ancak, yüksek gerinim hızlarında, gerinim arttıkça artan adyabatik ısınma nedeniyle gerinim hızı hassasiyetleri düşmüştür. Her iki alaşımın Johnson-Cook malzeme model parametreleri, adyabatik ve izotermal koşullar için ayrıca belirlenmiştir. C-316L numunelerindeki martenzit oluşumu ve SLM-316L numunelerindeki ikiz oluşumu statik gerinim hızlarına kıyasla yüksek gerinim hızlarında azalmıştır. C-316L'nin XRD spektrumları da yüksek gerinim hızlarında martenzit oluşumunun azaldığını doğrulamıştır. Yüksek gerinim hızlarında azalan ikizlenme ve martenzit oluşumu, test numunelerinin adyabatik ısınması nedeniyle artan istif bozukluğu enerjisine bağlanmıştır. Yüksek gerinim oranlarında istif bozukluğu enerjisinin artması, kayma ile deformasyonu teşvik etmiştir. Son olarak, yeniden yükleme testleri, SLM-316L'de bir gerinim hızı geçmişi etkisi ortaya koyarken C-316L'de bu etkinin olmadığını ortaya çıkarmıştır.

# TABLE OF CONTENTS

LIST OF FIGURES .....	vi
LIST OF TABLES .....	x
CHAPTER 1. INTRODUCTION .....	1
CHAPTER 2. LITERATURE REVIEW .....	3
2.1. AISI 316L Stainless Steel .....	3
2.2. Additive Manufacturing .....	4
2.3. Microstructural Features of SLM-316L .....	9
2.4. Mechanical Behavior of SLM-316L .....	11
2.5. Deformation Martensite and Twinning .....	13
2.6. The Effect of Strain Rate on the Deformation of C-316L .....	19
2.7. Motivation of Thesis .....	20
CHAPTER 3. MATERIALS, TESTS AND CHARACTERIZATION METHODS .....	21
3.1. Materials .....	21
3.2. Quasi-Static Compression Tests .....	23
3.3. High Strain Rate Compression Tests .....	24
3.4. Material Characterization .....	28
CHAPTER 4. RESULTS AND DISCUSSION .....	33
4.1. Microstructural Characterizations of Untested Specimens .....	33
4.2. Quasi-Static Compression Tests .....	41
4.3. SHPB Tests and the Effect of Strain Rate .....	51
4.4. Constitutive relations and strain rate sensitivity .....	62
4.5. Effect of Strain Rate .....	69
4.6. Unloading-Reloading Compression Tests .....	70
CHAPTER 5. CONCLUSIONS .....	72
REFERENCES .....	74

# LIST OF FIGURES

<b><u>Figure</u></b>	<b><u>Page</u></b>
Figure 2.1. Composition diagram linkages in the AISI stainless-steel family. ....	4
Figure 2.2. Categories of additive manufacturing according to ASTM F42 committee.....	6
Figure 2.3. Schematic representation of the SLM method a) SLM method and b) some process parameters. ....	6
Figure 2.4. Pore types; a) lack of fusion induced pore b) gas induced pore c) residual stress induced pores and d) keyhole pore. ....	7
Figure 2.5. (a) Columnar grains and b) sub-grain structure formed in the SLM method.....	10
Figure 2.6. Optical micrographs of 0.10 strained a) SLM-316L and b) Annealed- 316L. ....	11
Figure 2.7. Scanning strategy types in SLM method.....	13
Figure 2.8. (a)Schematic representation of TRIP deformation (b) and (c) a martensite transformation from TEM analysis with the schematic crystal pattern.....	14
Figure 2.9. Schematic representation of (a) undeform and (b) twinned FCC structure.....	15
Figure 2.10. (a) Deformation twins from TEM analysis and (b) crystal pattern of a twin at the atomic scale.....	16
Figure 2.11. Schematic representation of the strain hardening mechanism in TWIP steels. ....	16
Figure 2.12. Close-packed stacking of atoms in FCC phase and schematically representation of partial dislocation movement.....	17
Figure 2.13. Schematic representation of a stacking fault with Shockley partial dislocations. ....	17
Figure 3.1. (a) Specimens after SLM processing, (b) SLM bar and directions and (c) rotating scanning with biaxial plane.....	22
Figure 3.2. (a) the picture of test machine and (b) the details of test using strain- constraint ring. ....	24

<b><u>Figure</u></b>	<b><u>Page</u></b>
Figure 3.3. The schematic of SHPB test system.....	26
Figure 3.4. The picture of the used Inconel SHPB set-up. ....	27
Figure 3.5. Typical voltage-time readings of a SHPB test (a) with and without using a pulse shaper and (b) with the use of strain constraint ring.....	27
Figure 3.6. The compression tests specimen slicing in three different plane and coding of the planes in Bakelite mounted samples.....	30
Figure 3.7. The intercept method for the determination of average grain size.....	31
Figure 3.8. HV indentation and the measured indentation lengths.....	32
Figure 4.1. The optical microscopy pictures of SLM-316L: normal to the z-axis a) higher laser power and b) lower laser power processed alloy, parallel to the z-axis c) higher laser power and d) lower laser power processed alloy and the SEM picture of sub-grains structure e) higher laser power and f) lower laser power processed alloys. ....	34
Figure 4.2. The optical pictures of C-316L in (a) parallel and (b) perpendicular to the extrusion direction. ....	35
Figure 4.3. The XRD spectra of untested C-316L and SLM-316L.....	36
Figure 4.4. Hardness values in SLM-316L rectangular bar along the build direction. ....	37
Figure 4.5. At different loads, (a) hardness values of SLM-316L and (b) average hardness values of SLM-316L and C-316L.....	38
Figure 4.6. Higher laser power processed specimen at (a) HV0.05 and (b) HV2 hardness test and lower laser power processed specimen at (c) HV0.05 and (d) HV2 hardness test. ....	39
Figure 4.7. SLM-316L processed with higher and lower laser power tested at HV2 and HV0.05 loads.....	39
Figure 4.8. (a) EBSD maps in the tensile axis of 0° and 90° inclined specimens, (b) pole figures for 0° inclined specimen perpendicular to building direction (normal to z-axis), and (c) inverse pole figures showing <110> fiber texture in the z-axis.....	40
Figure 4.9. Quasi-static ( $1 \times 10^{-3} \text{ s}^{-1}$ ) compression true stress-strain curves of SLM and C 316L. ....	41

<b><u>Figure</u></b>	<b><u>Page</u></b>
Figure 4.10. The optic picture of quasi-static tested (a) SLM-316L and (b) C-316L until 0.36 strain. ....	43
Figure 4.11. The SEM picture of quasi-static tested (a) SLM-316L and (b) C-316L until 0.36 strain. ....	44
Figure 4.12. The SEM micrographs showing twinned regions in SLM-316L deformed until about (a) 0.11, (b) 0.22, (c) 0.36 and (d) 0.51 strains.....	45
Figure 4.13. The SEM micrographs showing martensite plates (also lesser number of twins) in C-316L deformed until about (a) 0.11, (b) 0.22, (c) 0.36 and (d) 0.51 strain. ....	45
Figure 4.14. Quasi-static jumping true stress-strain curves of SLM-316L and C-316L.....	46
Figure 4.15. The XRD spectra of quasi-static tested SLM-316L and C-316L.....	47
Figure 4.16. Optically measured martensite volume at (a) 0, (b) 0.11, (c) 0.22, (d) 0.36 and (e) 0.51 true strain in quasi-static test. ....	48
Figure 4.17. The hardness values (HV2) at 0.11, 0.22, 0.36 and 0.51 strain values for quasi-static tests. ....	50
Figure 4.18. Hardness value (HV0.5) of tested SLM-316L and C-316L specimens applied to twin, no-twin, martensite and no-martensite region, respectively.....	50
Figure 4.19. The optical pictures of hardness tests of tested SLM-316L and C-316L specimens applied to (a) twin, (b) no-twin, (c) martensite and (d) no-martensite region, respectively. ....	51
Figure 4.20. (a) compression true stress and true strain curves in the SHPB tests, (b) true stress-true strain curves of (b) SLM-316L and (c) C-316L at quasi-static and dynamic strains rates.....	52
Figure 4.21. The pictures of untested and dynamically tested specimens (a) SLM-316L and (b) C-316L. ....	54
Figure 4.22. Representative work hardening-true strain curves of SLM-316L and C-316L with quasi-static and high strain rate true stress-true strain curves and three distinct regions. ....	55
Figure 4.23. The SEM picture of SHPB tested (a) SLM-316L and (b) C-316L until 0.36 strain. ....	56

<b><u>Figure</u></b>	<b><u>Page</u></b>
Figure 4.24. The optic picture of SHPB tested (a) SLM-316L and (b) C-316L until 0.36 strain. ....	57
Figure 4.25. The XRD spectra (a) of SHPB tested SLM-316L and C-316L and (b) comparison with quasi-static tested specimens. ....	58
Figure 4.26. Opticaly measured martensite volume at (a) 0.11, (b) 0.22, (c) 0.36 and (d) 0.51 true strain value for SHPB tests. ....	59
Figure 4.27. The hardness values (HV2) of SHPB and quasi-static tested SLM-316L and C-316L. ....	61
Figure 4.28. The martensite volume and hardness values of SHPB and quasi-static tested C-316L specimens. ....	61
Figure 4.29. The true stress vs. ln true plastic strain rate at different strains and the variation of c value with strain and strain rate (a) SLM-316L and (b) C-316L and (c) ln true stress vs. ln true plastic strain rate and m values at different strains for SLM-316L and C-316L. ....	64
Figure 4.30. The fitted value of (a) c with strain and (b) compression stress vs. temperature and fitted curve when m=1, for SLM-316L ( $\circ^{101}$ ) and C-316L ( $\bullet^{73}$ ). ....	66
Figure 4.31. Experimental and predicted JC true stress-true strain curves with temperature rise (a) SLM-316L and (b) C-316L. ....	68
Figure 4.32. SHPB reloading tests of previously quasi-static tested (a) SLM-316L and (b) C-316L specimens. ....	71
Figure 4.33. Quasi-static reloading tests of previously SHPB tested (a) SLM-316L and (b) C-316L specimens. ....	71

## LIST OF TABLES

<b><u>Table</u></b>	<b><u>Page</u></b>
Table 2.1. The nominal composition of the stainless steel 316L.....	3
Table 3.1. The chemical composition of the commercial 316L .....	22
Table 4.1. The average hardness of SLM-316L & C-316L.....	37
Table 4.2. The average martensite amount of quasi-static tested C-316L.....	49
Table 4.3. The average martensite amount of SHPB tested C-316L.....	60
Table 4.4. The hardness of SHPB and quasi-static tested C-316L and SLM-316L at 0.51 .....	62
Table 4.5. Activation volume of SLM-316L and C-316L at different strain rate range.	70

# CHAPTER 1

## INTRODUCTION

The austenitic AISI 316L steel is one of the most widely used alloys <sup>1</sup>. It is a ductile metal with a high corrosion resistance and a good fatigue resistance; it has a good weldability and it is also bio-compatible with the human body <sup>2</sup>. The AISI 316L alloy resists high temperature; hence, it is considered also as a high temperature alloy. All these properties make AISI 316L one of the most preferred alloys in the biomedical, marine, chemical, nuclear, aerospace and automotive industries. Commercial 316L (C-316L) is manufactured by using the conventional methods including casting, extrusion, rolling and forging. These methods may further require pre- and post-production processes in the applications that require complex design, mechanical properties and chemical composition. Alternative ways of processing metallic alloys based on the demands of reducing impurities and human factors, rapid prototyping, reducing production costs, and producing complex designs in a single step have emerged and consequently, alternative ways were sought in the production line.

Additive manufacturing (AM) emerged in the 1980s <sup>3, 4</sup>. It was called rapid prototyping at the beginning <sup>5</sup>. A general definition for AM may be a manufacturing process that produces three-dimensional parts by adding two-dimensional layers on the top of each other. It is a method that has the capabilities of producing almost all kinds of materials including polymers, ceramics and metals and their composites. It has met the demands of the industry and started to change the production line radically <sup>5</sup>. Different AM methods have been developed so far <sup>6</sup>. Among them, the Selective Laser Melting (SLM) is the fastest growing one and capable of producing more than one part at once. Moreover, it is the most widely investigated AM method for processing metallic parts both by the academia and industry <sup>6</sup>.

Studies have reported that SLM processed AISI 316L (SLM-316L) exhibit quite different mechanical properties and deformation behavior from C-316L <sup>7, 8</sup>. Until now, the studies have focused on the mechanical properties and deformation behavior of SLM-316L at quasi-static strain rates, examples of which can be found in the refs <sup>9-12</sup>. There have been however few studies<sup>13, 14</sup> in the literature focusing on the strain rate dependent

deformation and flow stress behavior of SLM-316L. The strain rate regime investigated in these studies are also narrower and the effect of strain rate on the deformation behavior has not been fully investigated yet. This thesis is therefore performed in order to clarify and understand the strain rate dependent compressive deformation and the rate sensitive flow stress behavior of an SLM-316L alloy in a wider strain rate regime, spanning from quasi-static to high strain rates. The deformation and rate sensitive behavior of SLM-316L were further compared with those of a C-316L alloy. For these, cylindrical compression test specimens of both alloys were prepared and tested at both quasi-static and high strain rates. The compression tested SLM-316L and C-316L specimens until about prescribed final strains were then examined microscopically by using SEM, optical microscopy, EBDS and XRD in order to clarify the dominant deformation modes and phase transformation at different strain rate regimes. The Johnson and Cook (JC) flow stress constitutive relations of both alloys were determined based on the quasi-static and high strain rate compression tests. Hardness tests were performed on the deformed specimens to determine any strain rate strengthening effect. The strain rate history effects in both alloys were finally investigated by reloading the quasi-statically and dynamically tested specimens to a lower or a higher strain rate.

## CHAPTER 2

### LITERATURE REVIEW

#### 2.1. AISI 316L Stainless Steel

The AISI 316L steel is a member of AISI 300-grade austenitic stainless-steel family (see Figure 2.1). The nominal composition of AISI 316L is tabulated in Table 2.1 and the major alloying elements are 16-20% chromium, 10-14% nickel and 2-3% molybdenum. The AISI 316L steel has a similar composition with AISI 304, except molybdenum. Molybdenum reinforcement contributes to the pitting corrosion resistance<sup>1, 15, 16</sup>. It has also a lower carbon content (0.03%) than AISI 316L. The lower carbon content reduces the sensitization and increases the formability and machinability. The presence of a high percentage of chromium induces a high oxidation and corrosion resistance and nickel stabilizes the austenitic phase. Chromium forms an oxide layer on the surface that protects the underneath alloy from the corrosive environment. As the AISI 316L steel is biocompatible with the human body, it is widely used in the food industry, biomedical tools and prosthesis<sup>1</sup>. The machinability, formability, weldability and high temperature performance make it also useful in the nuclear, aviation and automotive industries<sup>1, 17</sup>.

Table 2.1. The nominal composition of the AISI 316L steel.

(Source: Peckner et al., 1977)

Composition (%)	C	Mn	Cr	Ni	Mo	Fe
316L	0.03 (max)	2	16-18	10-14	2-3	Balanced

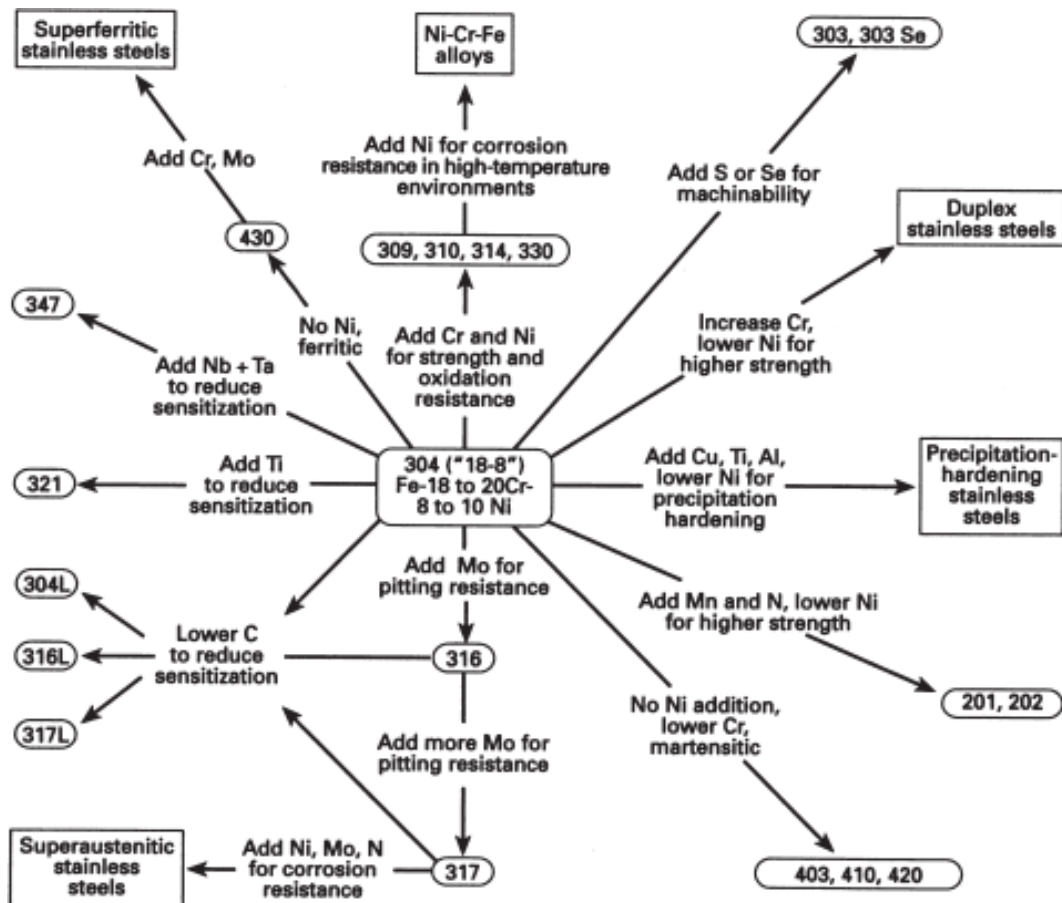


Figure 2.1. Composition diagram linkages in the AISI stainless-steel family.

(Source: Davis et al., 2000)

## 2.2. Additive Manufacturing

The first idea and experimental work on AM were in the 1980s. In these years, the final product prototypes were started to be constructed before the mass production in order to reduce the costs of molds. Hence it was referred to as rapid prototyping<sup>3,4</sup> which is known as AM today. Additive manufacturing methods are distinctly different from conventional methods. In the conventional methods, the final product is manufactured by removing the parts from the previously cast or extruded raw materials, known as subtractive method, while in AM the product is manufactured by sequential melting micron or even nano-sized powder layers<sup>18</sup>. In this way, the raw material consumption is significantly reduced and the complex structures that cannot be manufactured by conventional methods can be produced. As the complex structures can be produced almost exactly as it was designed, so unlike the conventional method, AM products

require either lesser number of or no pre- and post-processes; hence it provides nearly a single-step production <sup>19</sup>. AM reduces greenhouse gas emissions; therefore, it is a more environmentally friendly production method <sup>20</sup>.

Additive manufacturing of metals and alloys is noted to be an emerging technology and has problems that have to be overcome in order to widen its application areas <sup>20</sup>. The cooling rates in AM are extremely very high, ranging from  $10^3$  to  $10^8$  K/s <sup>7</sup>. Heterogeneously distributed residual stresses, porosity, delamination, changes in the microstructure, anisotropy in the mechanical properties and the formation of different micro-defects are frequently detected in AM methods <sup>21-27</sup>.

The categorization of additive manufacturing in the ASTM F42 committee is shown in Figure 2.2 <sup>28</sup>. Some of the commonly used methods for metals are as follows; Binder Jetting (BJ), Powder Bed Fusion (PBF), and Powder Fed or Directed Energy Deposition (DED). The most commonly used PBF methods include SLM, Electron Beam Melting (EBM), Direct Laser Deposition and Laser Powder Fed (LPF). EBM falls under the class of powder-bed and electron-based fusion according to the ASTM F42 committee <sup>23, 28</sup>.

In EBM, an electron discharge beam fuses the metal particles in the powder bed by melting them. Since electrons are used, the atmosphere is under vacuum. Although the vacuum atmosphere is needed to prevent oxidation, it has been reported that elements such as molybdenum can segregate during production <sup>29</sup>. In the BJ method, the final part is produced layer by layer by selectively injecting a liquid binder into metal powders. The produced green part is then sintered in a high-temperature furnace to burn the polymer binder and sinter the metal powders. It is reported that it is difficult with the BJ method to reach the desired densities in the final material <sup>18</sup>. The LPF method is laser-based and falls within the scope of the ASTM F42 committee standard's DED. In the LPF method, the laser is fed directly with the blown powder during the process.

The SLM is a powder bed AM method. It uses laser beam to melt the powders. Different names such as Direct Laser Melting and Laser Beam Powder Bed Fusion are also used for the SLM. Laser Beam Powder Bed Fusion is a recent and most widely accepted name for these processes. The schematic of SLM method is shown in Figure 2.3(a). In the SLM method, as a thin layered powder laid on a platform (heated to  $80^\circ$ ) is selectively melted by scanning in two dimensions with a computer aid by a laser beam <sup>23</sup>. The thickness of powder layer is usually 20–100  $\mu\text{m}$ . Then the powder is laid again and this process is repeated until the final product is formed <sup>23</sup>. In the SLM production method,

there are numerous parameters that affect the final sample, some of which are shown in figure 2.3(b). The spacing between two consecutive laser beams is called hatch spacing or hatch distance. It is measured by a distance from the center of one beam to the center of the next beam. The scan speed of a laser system depends on how fast the laser beam moves on the powder bed. The melting of powder with a laser scan forms a melt pool and the boundaries between individual melt pools is called the melt pool boundary (Figure 2.3(b)).

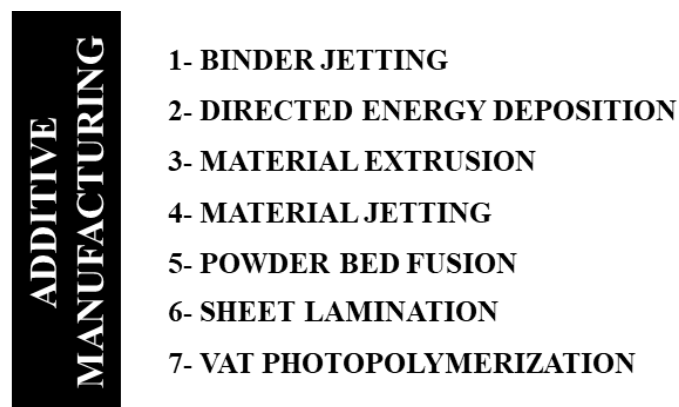


Figure 2.2. Categories of additive manufacturing according to ASTM F42 committee.

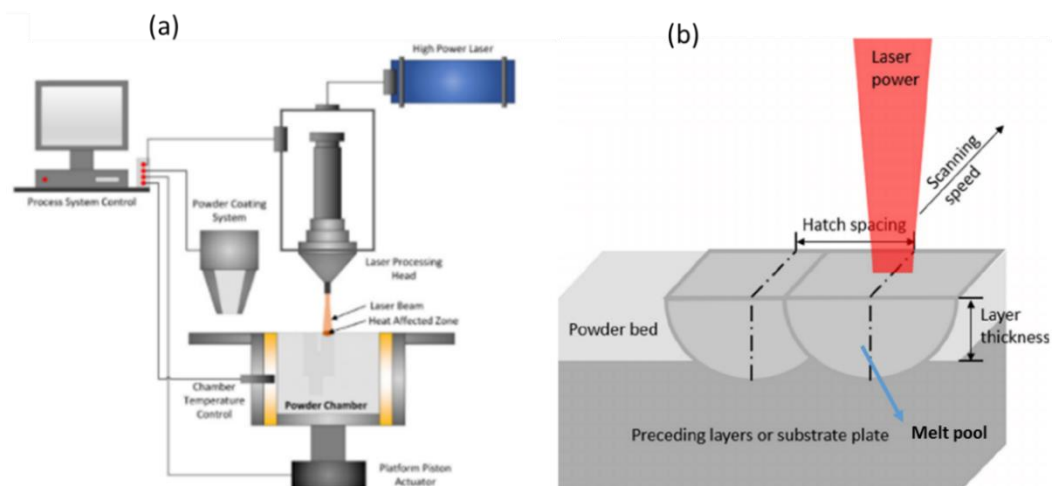


Figure 2.3 Schematic representation of the SLM method a) SLM method and b) some process parameters. (Source: Fayazfar et al., 2018)

If manufacturing parameters are determined properly, a higher specimen density can be achieved in the SLM compared to other AM methods, and multiple parts can be

produced quickly at once <sup>6</sup>. However, the flaws of AM methods such as formation porosity probability, anisotropy, differences of microstructure and interconnected unpredictable manufacturing parameters can also apply to the SLM method. Four types of pores were reported in the SLM processed alloys as depicted in Figures 2.4(a-d). These are the lack of fusion-induced pores, gas-induced pores, residual stresses process-induced pores and key holes <sup>11, 20</sup>. The lack of fusion pores occurs when the selected laser power is not sufficient to melt the powders (Figure 2.4(a)). Gas-induced pores are formed by the compression of the protective gas or the trapping gases during melting (Figure 2.4(b)). A high residual stress also results in pore formations at the melt pool boundaries (Figure 2.4(c)). When a high processing energy is used, irregularly shaped pores called keyholes are formed as shown in Figure 2.4(d) <sup>30, 31</sup>.

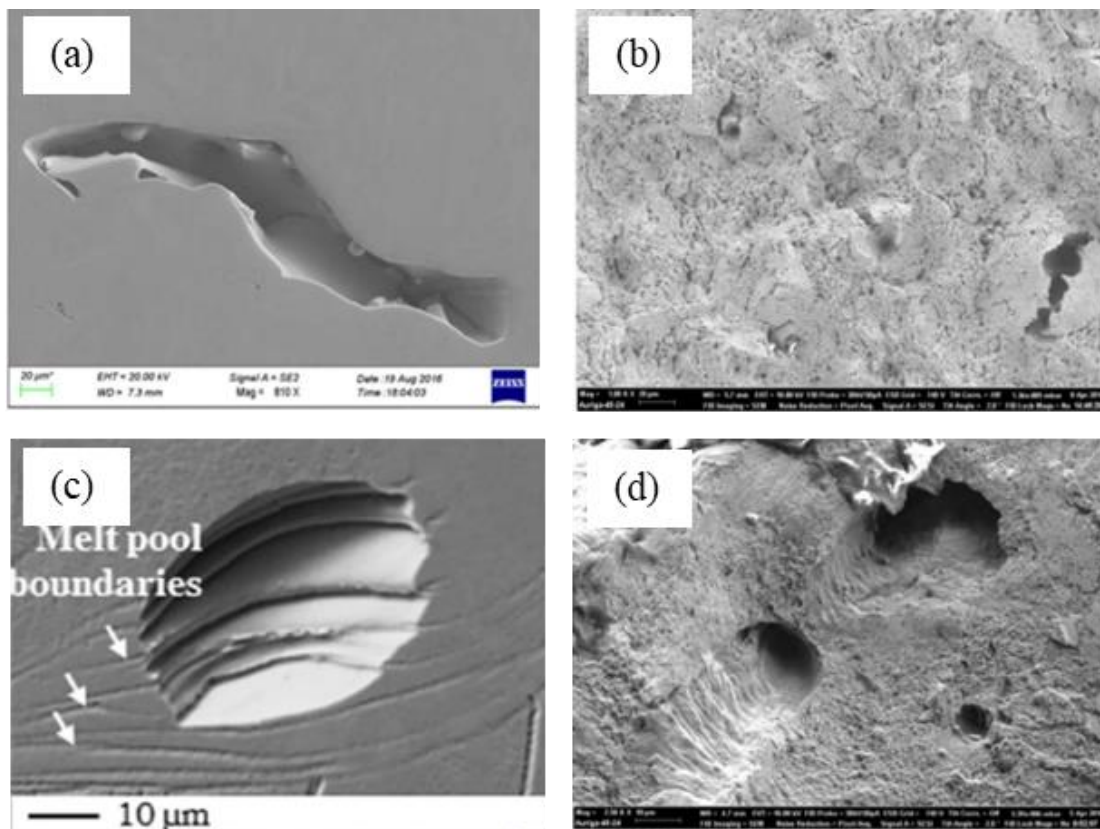


Figure 2.4. Pore types; a) lack of fusion induced pore b) gas induced pore c) residual stress induced pores and d) keyhole pore. (Source: Pham et al., 2017 and Liverani et al., 2017)

In most AM methods, residual stresses are naturally formed because of heterogenous cooling rates involved during processing. These residual stresses can cause

warping of the parts to be produced. Support structures are generally required in order to reduce the extent of residual stresses; hence, the part warpage. The presence of residual stresses may require post-processing such as heat treatment for stress relief.

The surface quality and final form of the final parts are also important and affected by the powder size. The finer metal powders produce sharp and clean final parts, but fine powders are more difficult to spread and lay<sup>20</sup>. Protective gases such as nitrogen and argon are used to form a protective atmosphere for the powders.

The effects of SLM manufacturing parameters on the material properties of metal parts, especially stainless steels, have been extensively studied. The production parameters affecting the microstructure of the alloys produced with SLM are as follows; laser power, layer scanning rate (or velocity) and type, hatch spacing, type of protective gas and powder type, powder size and alloy purity<sup>9, 11, 23</sup>. All these parameters determine the quality of the final SLM-produced alloy. In a study conducted in 2016, the effect of laser power (129, 144, 159 and 189 W) and laser scanning rate (1400, 1540 and 1680 mm s<sup>-1</sup>) on the mechanical properties of 316L stainless steel parts were investigated<sup>9</sup>. During production, the hatch spacing of 50 µm and layer thickness of 30 µm were kept constant. Two scanning strategies, the one-way method and cross-hatching technique, were used. The tensile strength of the specimens decreased with increasing scanning rate. An increase in laser power produced larger melt pools and lower amount of pores, both of which increased the density of the parts produced and hence the tensile strength increased. However, when the energy density increased more than a certain value, it was stated that the porosity increased due to the evaporation of metal from the melt pools.

The energy density  $E$  (J/mm<sup>3</sup>) in the SLM is given as<sup>9</sup>

$$E = \frac{P}{vht} \quad (2.1)$$

where  $P$  is the laser power (W),  $v$  is the scanning rate (mm/s),  $h$  is the hatch spacing (mm), and  $t$  is the layer thickness (mm). The energy density, based on Eqn. 2.1, increases with increasing laser power, but decreases with increasing scanning rate, hatch spacing and layer thickness.

In another study, AISI 316L components produced with SLM using different laser power, scanning rate, hatch spacing and fabrication orientation were characterized in terms of achievable density, tensile strength and fatigue life<sup>11</sup>. Among the process

parameters investigated, laser power was shown to have the strongest effect on the density. Relatively highest densities were achieved at the highest laser powers and at the lowest scanning rates. The building orientation and hatch spacing did not cause any significant effect on the final density. The mechanical behavior of the SLM specimens was comparable to or superior to that of commercial material and was mainly influenced by the building orientation. The strength decreased when the loading axis was 90° to the building direction as compared with the loading axis 45° to the building direction, while the elongation to failure increased up to 50%<sup>11</sup>. A review article on the effects of production parameters on the microstructure and mechanical behavior of SLM-processed specimens has been published<sup>23</sup>. It was reported in the same study that the density of the particle increased as the energy power increased. Highly dense parts were reported to be obtained at low energy densities using high heating depths and low hatching spaces. It was also reported that for steel alloys produced with SLM, the higher layer thickness resulted in low relative densities<sup>23</sup>. The effect of production parameters on the surface quality and the density of a pure tungsten metal, a high melting point metal, was investigated by the SLM method<sup>32</sup>. Specimens were produced using 200-300 W laser power and 200-400 mm s<sup>-1</sup> scanning rate. The surface quality of the parts produced at very high laser powers was found not good and the specimen contained porosities. On the other hand, the specimens processed using a relatively low laser energy density could not be densified<sup>32</sup>. It was also reported that the protective gases used diffused into the material and impaired the mechanical properties<sup>33</sup>.

### **2.3. Microstructural Features of SLM-316L**

There have been many publications on the microstructure development and the related mechanical properties of AISI 316L alloy produced by the SLM. The microstructure of SLM-316L alloy is quite different from that of C-316L<sup>7,25,34</sup>. Columnar grains develop parallel to the build direction in the SLM-316L alloy as shown in Figure 2.5 (a)<sup>35,36</sup>. The formation of planar, columnar and dendritic grains is governed by the shape of the liquid-solid interface, temperature gradient, solidification rate, and solute diffusion coefficient<sup>34</sup>. In addition, micro/nano-sized honeycomb-like sub-grain or sub-cell segregation network structure were observed inside the grains (Figure 2.5 (b))<sup>37-41</sup>. The sub-grains are the regions of high dislocation density (dislocation network) with

higher heavy atoms concentrations of the heavy elements such as Cr and Mo, arising from the extremely fast cooling rates impeding the diffusion of these heavy elements<sup>40</sup>. The sizes of sub-grains ranged 0.5-1  $\mu\text{m}$ <sup>40</sup>. Since, sub-grains have almost the same crystallographic orientation, they are not interpreted as grain boundaries. The arrangement of the cellular structure was shown to be affected by the laser scanning strategy and the long axes of sub-grains are generally parallel to the building direction<sup>40</sup>. Moreover, crystallographic texture was reported in the SLM-316L<sup>38, 42-46</sup>. In a previous study, 316L specimens were prepared by using 0°, 90° and 67° rotation scanning strategies. The growth of columnar grains in the plane perpendicular to the scanning direction resulted in the development of a strong single crystal-like texture. A strong  $\langle 100 \rangle$  and  $\langle 110 \rangle$  single crystal-like texture was observed sequentially in the laser scanning and build directions in the specimens printed with a bidirectional scanning strategy without rotation. Rotating the scans by 67° caused a mismatch of melt pool positions in each layer, which broke the epitaxy of columnar growth and resulted in fiber texture and a random distribution perpendicular to the build direction.

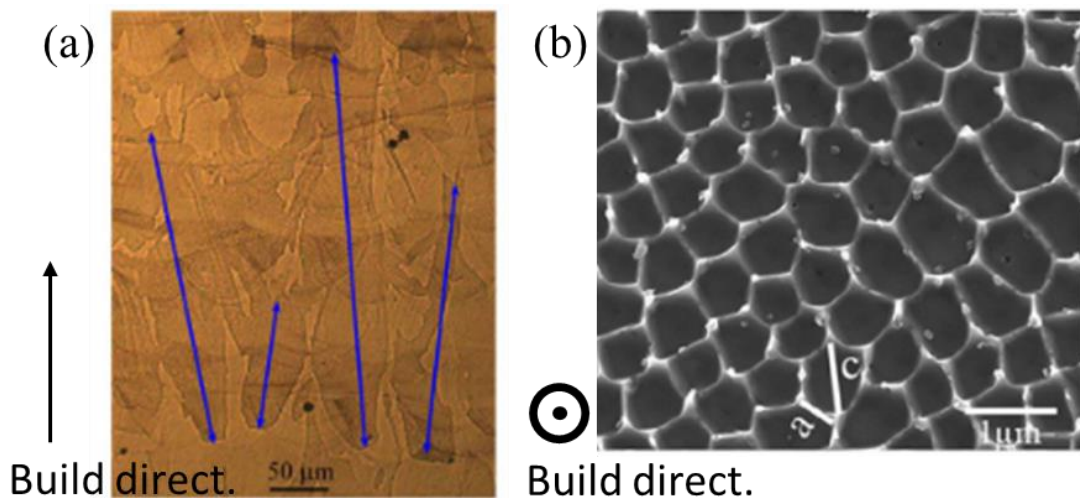


Figure 2.5. (a) Columnar grains and b) sub-grain structure formed in the SLM method.  
(Source: Ma et al., 2017 and Zhong et al., 2016)

To improve the strength and ductility of SLM-316L, attempts were made to manipulate sub-grain spacing and sub-grain growth by adjusting the scanning parameters and strategies in the SLM method<sup>47</sup>. The development of the sub-grain network structure was shown to be affected by the temperature gradient direction. Sub-grain spacing was reported to increase with increasing the scanning rate but increased scanning rate resulted

in lower densities. It was also suggested in the same study that sub-grain boundaries might act as obstacles for dislocations and hence increase the strength<sup>47</sup>. In another study, the effect of scanning rate on the texture formation of AISI 316L was studied<sup>48</sup>. The AISI 316L specimens were manufactured using a high, medium and low scanning rate. The specimen produced at the lowest scanning rate exhibited a cubic texture. The texture became more and more random as the scanning rate increased<sup>48</sup>. The effects of production parameters on the melt pool shape, cooling rate and columnar grain size of a SLM-316L were investigated<sup>49</sup>. During solidification, the cooling rate affected the grain sizes. Increasing laser power decreased the cooling rate of the melt pool from  $10^6$  to  $10^2$   $\text{K s}^{-1}$  and increased the length of columnar grains<sup>49</sup>. The microstructure and mechanical behavior of SLM-316L processed using a high and low laser power were further investigated together with the effect of hot isostatic pressing (HIP) post-processing<sup>50</sup>. A low-power laser resulted in higher cooling rates and thus a fine sub-grain microstructure. The finer sub-grain microstructure was reported to result in higher hardness and strength<sup>50</sup>. The effect of protective gas flow direction on the morphological and crystallographic structure of a 316L alloy was further investigated<sup>43</sup>. Specimens were prepared with different scanning angles of  $0^\circ$  and  $90^\circ$ . In the specimen scanned along the gas flow direction, the melt pool depth was reduced by 33% without affecting the melt pool width<sup>43</sup>.

## 2.4. Mechanical Behavior of SLM-316L

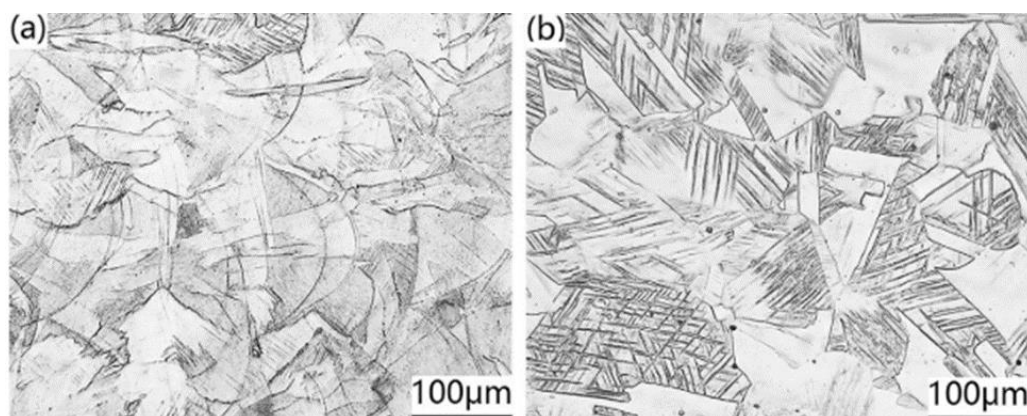


Figure 2.6. Optical micrographs of 0.10 strained a) SLM-316L and b) Annealed-316L.

(Source: Hong et al., 2019)

The yield strength of SLM-316L alloy was reported to be higher than that of C-316L alloy, which was attributed to the relatively higher dislocation density of the SLM-316L alloy<sup>37</sup>. SLM-316L is deformed by the twin-induced plasticity (TWIP), while the main deformation mechanism of C-316L is transformation-induced plasticity (TRIP) as shown in Figures 2.6(a) and (b), respectively<sup>31,51</sup>. TWIP deformation was also seen in a surface mechanical grinded 316L alloy<sup>52</sup>.

The tensile yield and ultimate tensile strength (UTS) and ductility of SLM-316L are reported sequentially 450-590 MPa, 640-700 MPa and 33-59% while these values are sequentially 160-365 MPa, 450-555 MPa and 30-43 % for C-316L<sup>20</sup>. It was also reported that the yield strength is higher perpendicular to the build direction, while the ductility is higher parallel to the build direction<sup>37,38</sup>. In a previous study, SLM-316L specimens were tested parallel to  $\langle 100 \rangle$ ,  $\langle 110 \rangle$  and  $\langle 111 \rangle$  crystallographic orientations<sup>38</sup>. Tensile test specimens with different orientation were processed using a unidirectional scanning strategy to obtain a single crystal-like orientation. The SLM-316L specimens showed similar strengths when tested in the  $\langle 100 \rangle$  and  $\langle 110 \rangle$  orientations, the strength was reported higher when the specimen tested in the  $\langle 111 \rangle$  orientation. The  $\langle 110 \rangle$  oriented specimen had the highest ductility and the ductility of the  $\langle 100 \rangle$  oriented specimens were the lowest. This was attributed to the different Schmid factors of different crystallographic orientations. The superior ductility of the  $\langle 110 \rangle$  and  $\langle 111 \rangle$  orientations can be rationalized by the extra strain hardening ability owing to the TWIP effect<sup>38</sup>. The effect of the scanning strategy of SLM-316L stainless steel was determined in a study<sup>53</sup>. Four different scanning strategies (stripe with contour, meander, stripe with no contour and checkerboard strategy as shown in Figure 2.7) were used to manufacture tensile specimens. The strip with the contour style generated the smallest sub-grain and grain sizes ( $610 \pm 19 \mu\text{m}$  and  $45 \pm 3 \mu\text{m}$ , respectively), while the checkerboard strategy generated the largest ( $887 \pm 15 \mu\text{m}$  and  $64 \pm 7 \mu\text{m}$ ).

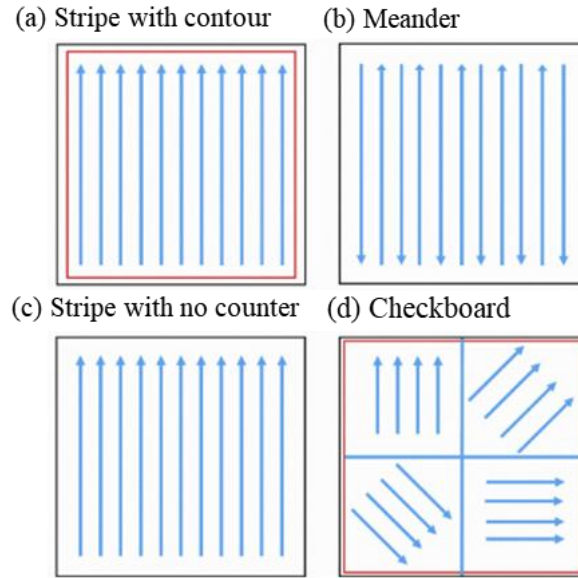


Figure 2.7. Scanning strategy types in SLM method.

(Source: Salman et al., 2019)

## 2.5. Deformation Martensite and Twinning

TRIP behavior is basically a diffusion-less change of crystal phase as a result of the deformation of the alloy in the austenite phase<sup>54, 55</sup>. The alloy transforms, during deformation, from a Face Centered Cubic (FCC) austenitic phase into a Body Centered Tetragonal or Body Centered Cubic (BCC) (its structure depends on the carbon content of the alloy<sup>55</sup>)<sup>56</sup>. Figure 2.8(a) schematically shows the transformation from the FCC phase to the BCC phase under stress. Figures 2.8(b) and (c) show martensite deformation in TRIP steel. Figure 2.8(b) shows the change in the crystalline structure at the atomic scale and the pattern just below<sup>57, 58</sup>. Although martensite formation occurs in a single step, in some cases, two-step martensite formation has also been reported. A transformation mechanism observed for main  $\alpha'$  martensite formation involves a two-step reaction. Here the  $\alpha'$  phase is formed from an intermediate  $\epsilon$  martensite phase. This formation includes two components. The first component includes a lattice displacement of  $\frac{a}{18} \langle 112 \rangle$  FCC achieved by an array of Shockley partial dislocations averaging one over every third (111) slip plane. The second component includes a displacement of  $\frac{a}{12} \langle 112 \rangle$  FCC and  $\frac{a}{8} \langle 110 \rangle$  BCC achieved by Shockley partials averaging one every second (111) plane. If the partial dislocations associated with the first component that are piled

up at the intersection of the second component structure could cross the uniformly distorted planes, the result will be the formation of a BCC structure<sup>59</sup>.

The diffusion-less nature of the martensitic transformation means that the resulting transition in the crystalline structure is accomplished by a consistent deformation of the FCC phase. To minimize the strain energy, martensite develops as thin plates in certain crystallographic planes, called habit planes<sup>60</sup>. These planes are the interface between the austenite and martensite and are flat for unconstrained transformations. Experimental observations indicate irrational orientation relationships, similar to the Kurdjumov-Sachs orientation<sup>61</sup>:

$$(111)_{\text{FCC}} \parallel (011)_{\text{BCC}} \quad , \quad \langle 101 \rangle_{\text{FCC}} \parallel \langle 111 \rangle_{\text{BCC}}$$

TRIP steels have a higher hardening rate compared to TWIP, so the deformability in TRIP wears off more quickly. However, TWIP steels have greater ductility, which provides a better ability for energy absorption and toughness<sup>55</sup>.

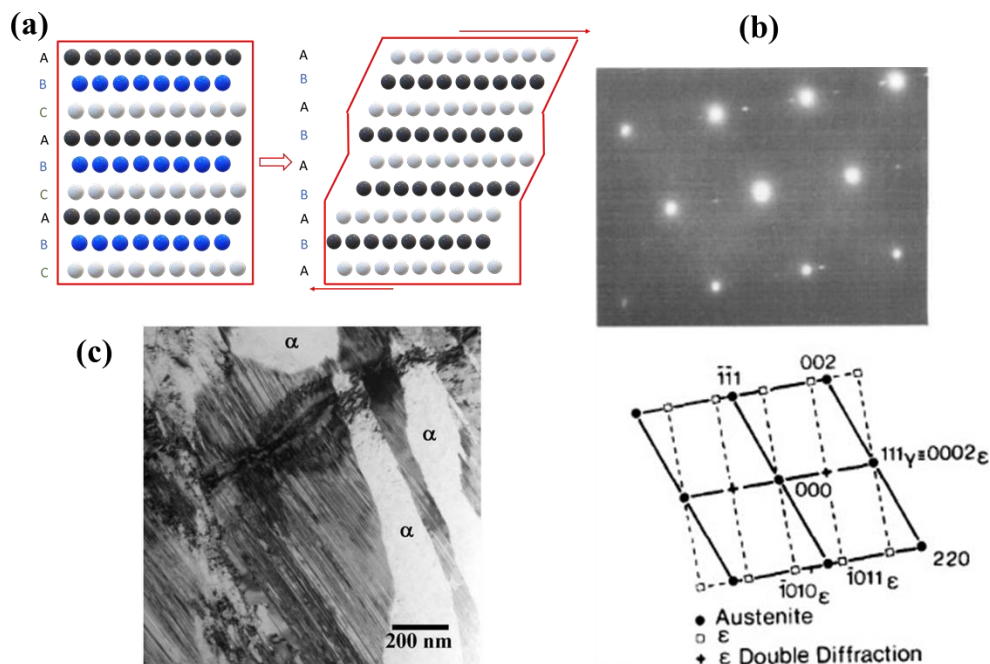


Figure 2.8. (a) Schematic representation of TRIP deformation (b) and (c) a martensite transformation from TEM analysis with the schematic crystal pattern.

(Source: (b) Remy et al., 1976 and (c) Pozuelo et al., 2009)

The deformation twinning is the refraction of the atomic orientation in the crystalline structure along a band. The initial unidirectional crystal structure splits into two different orientations that share a common plane. The crystal phase does not change, only its orientation changes. Twinning becomes a dominant deformations mechanism when the slip by the dislocation motion becomes difficult. If a shear stress is applied to the untwined crystal structure in Figure 2.9(a), the crystal plane is sheared without the phase transformation as seen in Figure 2.9(b). Every atom twinned in a lattice is moved by a distance that is proportional to the separation of the atoms from the twin plane <sup>62</sup>

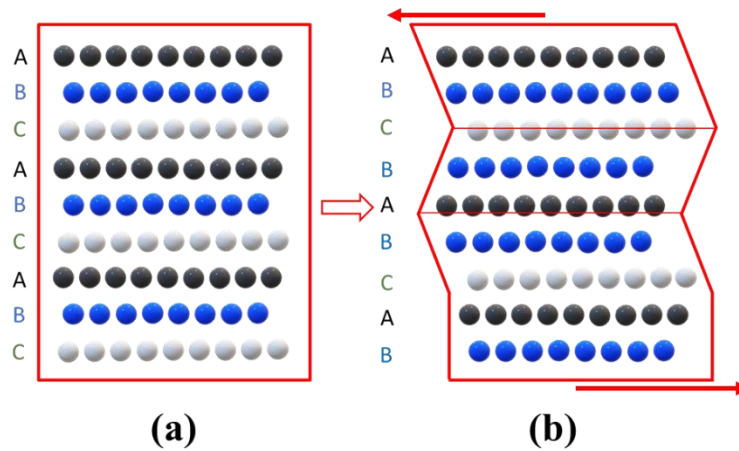


Figure 2.9. Schematic representation of (a) undeformed and (b) twinned FCC structure.

Although the atomic orientation above and below is the same in slip by dislocation, twinning changes the crystal orientation along the twin plane. Figures 2.10(a) and (b) show sequentially the twin deformation planes indicated by yellow arrows and a twinned crystal at the atomic scale in TWIP steel. The distance taken in twinning is much smaller than an atomic distance and twins have a 60° orientation with the crystal matrix <sup>55</sup>. Twin boundaries act as grain boundaries for dislocations, preventing slip. The strain hardening mechanism of TWIP steels is defined by the dynamic Hall-Petch relationship. The formation of twin deformation depends on the grain size and is also expressed by a Hall-Petch type equation as <sup>58</sup>

$$\sigma_T = \sigma_{T0} + K_T \times d^{-1/2} \quad (2.2)$$

where  $\sigma_T$  is the twin stress,  $\sigma_{T0}$  is the twin stress in a single crystal,  $K_T$  is the Hall-Petch constant for twinning and  $d$  is the grain size. In the dynamic Hall-Petch process,

deformation twins are formed continuously during deformation. As a result of twinning formation, the path the dislocations move becomes shorter and shorter, thus increasing the flow stress (Figure 2.11). As a result of increasing twinning formation, a high work hardening is observed in TWIP steels.

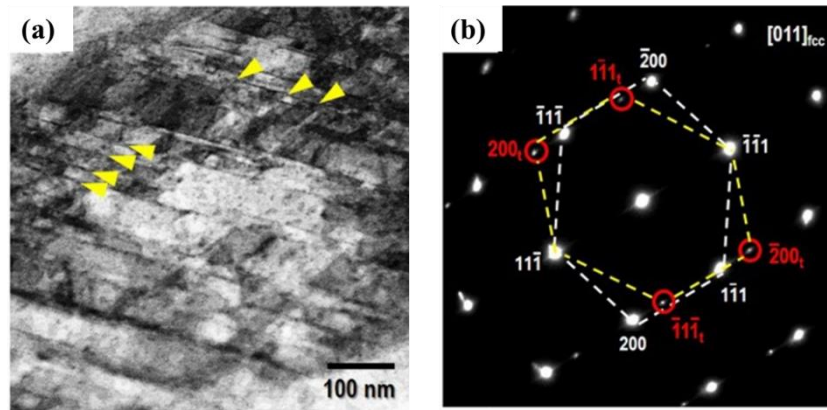


Figure 2.10. (a) Deformation twins from TEM analysis and (b) crystal pattern of a twin at the atomic scale. (Source: Woo et al., 2020)

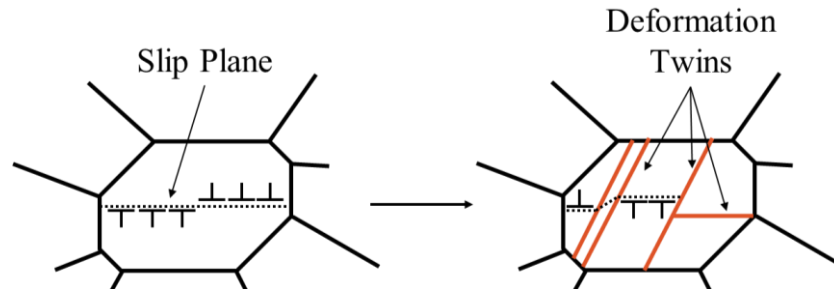


Figure 2.11. Schematic representation of the strain hardening mechanism in TWIP steels.

In FCC structures are formed by a certain stacking sequence of layer by layer. If the first close-packed layer is A (Figure 2.12), the next layers are the B and C layers A. If the stacking repeats every two layers (ABABAB...), the HCP or BCC structure is formed. However, in FCC structure stacking of layers repeats every three layers (ABCABC...) and each layer becomes the (111) plane of the final crystal structure.

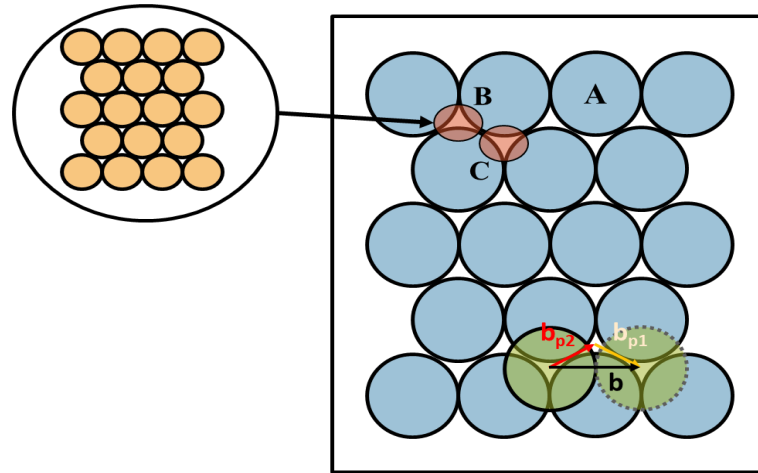


Figure 2.12. Close-packed stacking of atoms in FCC phase and schematically representation of partial dislocation movement.

Stacking layers are not perfect, the errors and discontinuities occur. Stacking faults are produced by local places in the crystal matrix where the normal stacking composition has been interrupted. Consider a stacking order for FCC phase (ABCABC...) and the first layer called A in Figure 2.12. The next atomic layer must be placed in the position B. But having two separate layers available such as B and C for sequencing is able to cause a stacking fault in the FCC. These are referred to as either intrinsic or extrinsic stacking faults. The stacking fault occurs with partial dislocation motion called a Shockley partial dislocation. Shockley partial dislocations are those associated with slip and the Burgers vector of the dislocation lies in the plane of the fault. The reason for the formation of two partial dislocations is that the dislocation, which occurs at one-step, is divided into two separate dislocations with a more suitable configuration in terms of energy as seen in Figure 2.13.

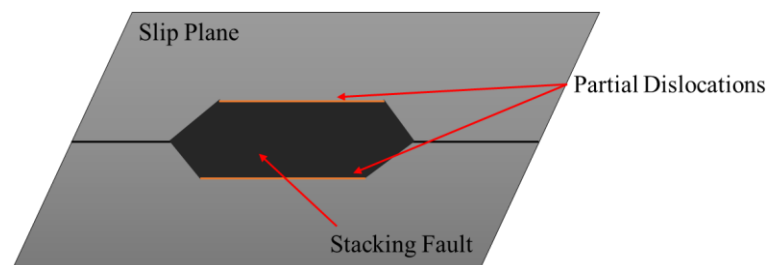


Figure 2.13. Schematic representation of a stacking fault with Shockley partial dislocations.

The favored slip plane for the dislocation motion is the plane with the highest atomic density. And the slip direction is the closest distance in the slip plane. Therefore, the FCC austenite slip system is  $\frac{a}{2} \langle 110 \rangle$  directions in  $\{111\}$  planes. As depicted in Figure 2.12, the slip of the green atom in one step is more difficult than the slip with the zig-zag movement through the grooves of the A-plane. The dissociation of the dislocation with the Shockley partial dislocation in (111) plane is as follows

$$\frac{a}{2} \langle 110 \rangle \rightarrow \frac{a}{6} \langle 211 \rangle_{\text{trailing}} + \frac{a}{6} \langle 121 \rangle_{\text{leading}} \quad (2.3)$$

The movement of a Shockley partial dislocation introduces an intrinsic stacking fault. Since the atoms on either side of a stacking fault are in positions that they would not normally occupy in a perfect lattice. A stacking fault has a stacking fault energy (SFE)<sup>63</sup>. The total surface energy increases with the distance between the partials as

$$E_{\text{SF}} = \gamma_{\text{SF}} L \times d \quad (2.4)$$

where  $E_{\text{SF}}$  is the surface energy of the stacking fault,  $\gamma_{\text{SF}}$  is the stacking fault energy of per unit area,  $L$  is the dislocation length and  $d$  is the separation between the partial dislocations. Therefore, the force ( $F$ ) opposing the repulsion of the partial dislocations is

$$F = \frac{-\partial E_{\text{SF}}}{\partial d} = -\gamma_{\text{SF}} \times L \quad (2.5)$$

Based on the above, the equilibrium was derived for a relationship for the separation of a stacking fault to be<sup>64</sup>

$$w = \frac{-Gb^2}{4\pi\gamma_{\text{SF}}} \quad (2.6)$$

where  $w$  is the width of the stacking fault,  $G$  is the shear modulus and  $b$  is the Burgers vector of the Shockley partial dislocations. There is an inverse relation between SFE and Stacking fault width. Therefore, if SFE decreases, stacking fault width increases. When the fault width increases, the cross-slip gets difficult and dominant deformation mechanism shifts from dislocation motion to TWIP or TRIP.

Twinning occurs when the shear stress reaches a critical shear stress in the twinning plane as similar with dislocation slip<sup>62</sup>. The critical shear stress for twinning ( $\sigma_{TW}$ ) is given as<sup>65</sup>.

$$\sigma_{TW} = \frac{2\gamma_{eff}}{m_{TW} b_1} \quad (2.7)$$

where,  $\gamma_{eff}$  is the effective SFE,  $m_{TW}$  is the Schmid factor for the deformation twinning and  $b_1$  is the Burgers vector of a partial dislocation. The effective SFE is given as<sup>66</sup>.

$$\gamma_{eff} = \gamma_{sf} + \frac{(m_2 - m_1)}{2} \sigma b_1 \quad (2.8)$$

where,  $\gamma_{sf}$  is the SFE before applying stress,  $\sigma$  is the applied stress and  $m_1$  and  $m_2$  are the Schmid factor for the leading [121] and [211] trailing partial dislocations, respectively<sup>67</sup>. If the  $m_1$  higher than the  $m_2$ ,  $\gamma_{eff}$  will decrease while the  $m_2$  higher than the  $m_1$ ,  $\gamma_{eff}$  will increase.

## 2.6. The Effect of Strain Rate on the Deformation of C-316L

In an earlier study in 1985, the mechanical response of 316H alloy at increasing strain rates was reported<sup>68</sup>. Specimens were quasi-statically loaded and unloaded at  $0.004 \text{ s}^{-1}$ , and then dynamically reloaded at  $500 \text{ s}^{-1}$  by using a Split Hopkinson Pressure Bar (SHPB) test apparatus. The alloy showed a strain rate sensitive flow stress behavior without any strain rate history effect. A strain rate-sensitive flow stress behavior of C-316L was also reported between  $0.02 \text{ s}^{-1}$  and  $100 \text{ s}^{-1}$ <sup>69</sup>. The adiabatic shear band formation in annealed and rolled C-316L alloys was investigated by dynamically testing hat-shaped specimens in the SHPB<sup>70, 71</sup>. The annealed C-316L alloy showed adiabatic shear band formation after considerable work hardening. In the cold-rolled C-316L alloy, the deformation twins were seen inside the shear bands. In another study, compression test was applied to a biomedical grade and a sintered 316L alloy between  $10^{-3} \text{ s}^{-1}$  and  $7.5 \times 10^3 \text{ s}^{-1}$ , and between  $1 \times 10^3$  and  $5 \times 10^3$ , respectively<sup>72-74</sup>. A biomedical C-316L alloy was further tested in a temperature range of 25-800 °C. The results showed that the yield

strength increased with the increase of strain rate from quasi-static to dynamic rates in the sintered and the biomedical grade 316L alloys. It was also reported that the work hardening rate decreased at increasing temperature<sup>72,73</sup>.

## 2.7. Motivation of Thesis

Until now, the studies have been focused mechanical properties and deformation behavior of SLM-316L at quasi-static strain rates, examples of which can be found in the refs<sup>9-12</sup>. There have been however few studies<sup>13, 14</sup> in the literature investigating the effect of strain rate on the deformation and flow stress behavior of SLM-316L. In a previous study, the strain rate sensitivity of an SLM-316L alloy was reported to be lower than that of a C-316L alloy between quasi-static to dynamic strain rates ( $2000 \text{ s}^{-1}$ )<sup>13</sup>. Another study reported a higher strain rate sensitivity of SLM-316L than coarser-grained C-316L alloy between  $5 \times 10^{-5}$  and  $10^{-1} \text{ s}^{-1}$ <sup>14</sup>. The deformation activation volume of the SLM-316L alloy was reported 3 times smaller than that C-316L alloy. In above the strain rate regime investigated in above studies are narrower and the effect of strain rate on the deformation behavior has not been comprehensively investigated yet. This thesis is therefore performed in order to clarify and understand the strain rate dependent compressive deformation and the rate sensitive flow stress behavior of an SLM-316L alloy in a wider strain rate regime, spanning from quasi-static ( $1 \times 10^{-4} \text{ s}^{-1}$ ) to high strain ( $\sim 2500\text{-}3000 \text{ s}^{-1}$ ) rates. The compression tests on SLM-316L were performed perpendicular to the building direction. The deformation and rate sensitive behavior of SLM-316L were further compared with those of an annealed-extruded C-316L. For these, cylindrical compression test specimens of both alloys were prepared and tested at both quasi-static and high strain rates. The compression tested SLM-316L and C-316L specimens until about prescribed strains were then examined microscopically by using SEM, optical microscopy, EBDS and XRD in order to clarify the dominant deformation modes and phase transformation at different strain rate regimes. The Johnson and Cook (JC) flow stress constitutive relations of both alloys were determined based on the quasi-static and high strain rate compression tests. Hardness tests were also performed on the deformed specimens to determine any strengthening. The strain rate history effects in both alloys were finally investigated by reloading the quasi-statically and dynamically tested specimens to a lower or a higher strain rate.

## CHAPTER 3

# MATERIALS, TESTS AND CHARACTERIZATION METHODS

### 3.1. Materials

The SLM-316L compression test specimens were extracted from the rectangular bars. Rectangular bars (Figures 3.1(a) and (b)) which were procured from the Turkish Aerospace Industry were fabricated in a Laser-powder bed fusion AM Concept Laser M2 Cusing device using gas atomized 316L powder used for the first time with an average size of 40  $\mu\text{m}$  under protective nitrogen atmosphere. A multidirectional scanning (biaxial scanning) laser-pattern was used to construct the specimens. Following parameters were used: the power of the incident beam=370 W, the hatching space=115  $\mu\text{m}$ , the spot size=160  $\mu\text{m}$ , the scanning rate= 900  $\text{mm s}^{-1}$  and layer thickness=30  $\mu\text{m}$ . In a few fabricated bars which are produced with different process parameters, formed different sizes of sub-grains when keeping a constant grain size were noticed. In these bars parameters, the power, hatching space, spot size and scanning rate of the incident beam were changed to 180 W, 95  $\mu\text{m}$ , 140  $\mu\text{m}$  and 700  $\text{mm s}^{-1}$ , respectively. These bars manufactured different parameters were solely used to determine the effect of sub-grain size on the hardness values. The SLM-316L bars had the dimensions of 130x13x6 mm. The height (130 mm) of the bar is the building (z)-direction, the width (13 mm) is the y-direction and the thickness (6 mm) is the x-direction (Figure 3.1(b)). The schematic of the used biaxial scanning is shown in Figure 3.1(c). The laser scan is rotated 90° between adjacent layers. The scanned plane is called biaxial plane and x and y directions are making 45° with the scanning as shown in Figure 3.1(c). Cross-sections of biaxial melt pools are seen in the x-z and y-z planes perpendicular to the scanning plane.

The prepared SLM-316L rectangular bars were reduced to 5 mm by machining 0.5 mm on both sides. Then, 5mm diameter and 5 mm length of sizes of cylindrical compression specimens were extracted along the x-direction from the bars using an electro-discharge machine. The picture of a compression test specimen is shown in Figure 3.1(b).

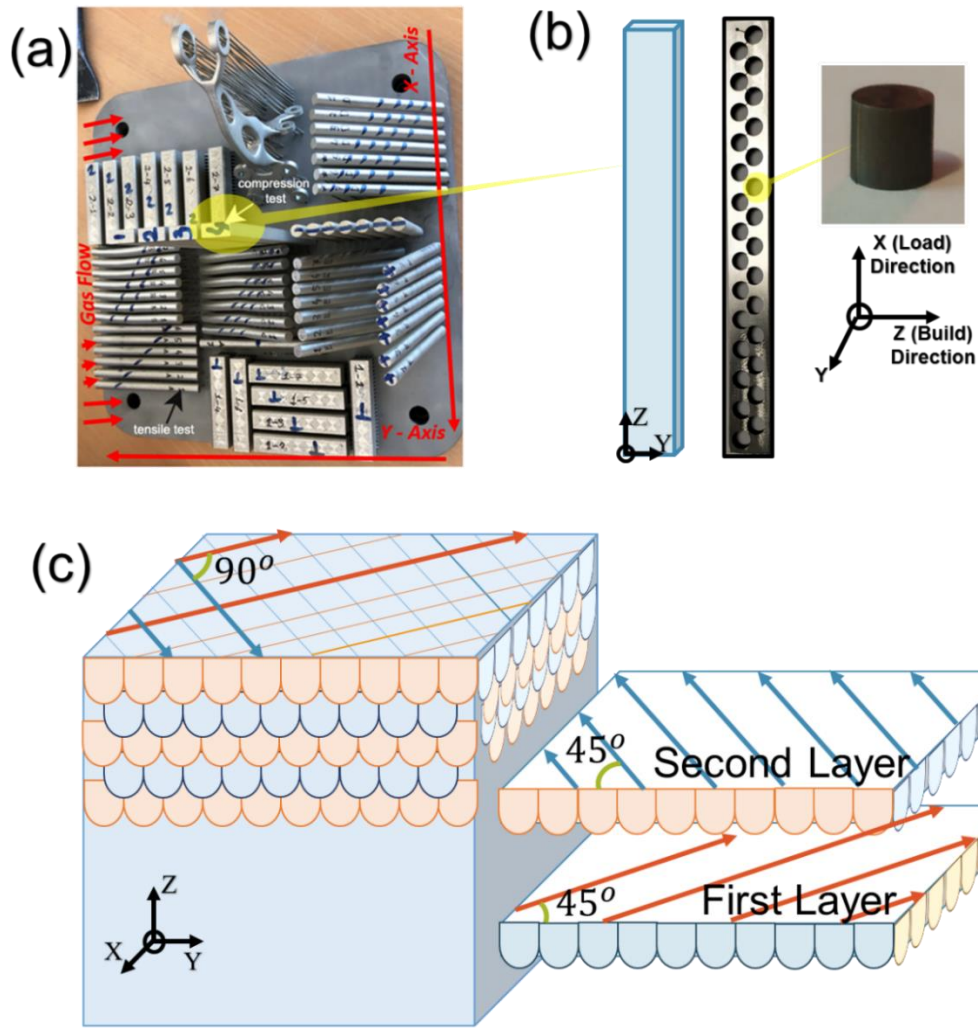


Figure 3.1. (a) Specimens after SLM processing, (b) SLM bar and directions and (c) rotating scanning with biaxial plane.

The compressive load was applied in the x-direction. The tested C-316L alloy was produced by Viraj Impoexpo. The alloy bar, 18 mm in diameter, was an annealed-extruded bar. The compression tests specimens having the same dimensions as SLM-316L were machined through the extrusion direction; hence, the compressive loading axis was the extrusion direction. The producer supplied chemical composition of C-316L alloy is given in Table 3.1

Table 3.1. The chemical composition of the commercial 316L

316L Steel	C	Mn	Si	S	P	Ni	Cr	Mo	Cu	N	Co
Commercial	0.022	1.40	0.45	0.021	0.034	10.04	16.30	2.05	0.38	0.069	0.19

### 3.2. Quasi-Static Compression Tests

The quasi-static compression tests were performed in a Shimadzu AG-X universal test machine (Figure 3.2(a)). The compression test specimens of SLM-316L and C-316L were tested at  $1 \times 10^{-4}$ ,  $1 \times 10^{-3}$  and  $1 \times 10^{-2} \text{ s}^{-1}$ . The tests were performed until about prescribed engineering strains of 10, 20, 30 and 40% in order to determine the deformation microstructure as function strain. The schematic of the use of tool steel strain constraint ring in the compression test is shown in Figure 3.2(b). The ring was placed around the test specimen and when the upper platen starts to compress the ring, the force increased sharply; then the test was stopped. The 10 mm inner diameter of the ring allowed the expansion of the test specimen laterally. The height of the used rings was 4.5, 4, 3.5 and 3 mm sequentially for 10, 20, 30 and 40% engineering strains. Strain rate jump tests were also performed at  $1 \times 10^{-4}$ ,  $1 \times 10^{-3}$  and  $1 \times 10^{-2} \text{ s}^{-1}$ . During the jumping tests, without removing the force on the specimen, the strain rate was increased from  $1 \times 10^{-4}$  to  $1 \times 10^{-3} \text{ s}^{-1}$  and from there to  $1 \times 10^{-2} \text{ s}^{-1}$ . Tests were performed up to 10% strain at  $1 \times 10^{-4} \text{ s}^{-1}$ , up to 20% strain at  $1 \times 10^{-3} \text{ s}^{-1}$  and up to 30% strain at  $1 \times 10^{-2} \text{ s}^{-1}$ .

At least three tests were performed for each group of specimens at the same strain rate and a thin layer of lubricant was applied to the bottom and top of the specimens to reduce frictional forces. In the compression tests, the specimen displacement was recorded by using a video extensometer (Figure 3.2(a)). The labels of the extensometer were placed at the edge of the compression test bottom and upper platens, as shown in Figure 3.2(b), to merely measure the specimen compression displacement. The engineering strain ( $\epsilon_{eng}$ ) and stress ( $\sigma_{eng}$ ) were calculated as

$$\epsilon_{eng} = \frac{\Delta L}{L_s} \quad (3.1)$$

$$\sigma_{eng} = \frac{P}{A_s} \quad (3.2)$$

where  $\Delta L$  is the extensometer displacement,  $P$  is the applied load and  $L_s$  and  $A_s$  are the length and area of test specimen. The calculated engineering strains and stresses were converted to true strain ( $\epsilon_{tr}$ ) and true stress ( $\sigma_{tr}$ ) by using the following equations,

$$\varepsilon_{tr} = -\ln(1 - \varepsilon_{eng}) \quad (3.3)$$

$$\sigma_{tr} = \sigma_{eng}(1 + \varepsilon_{eng}) \quad (3.4)$$

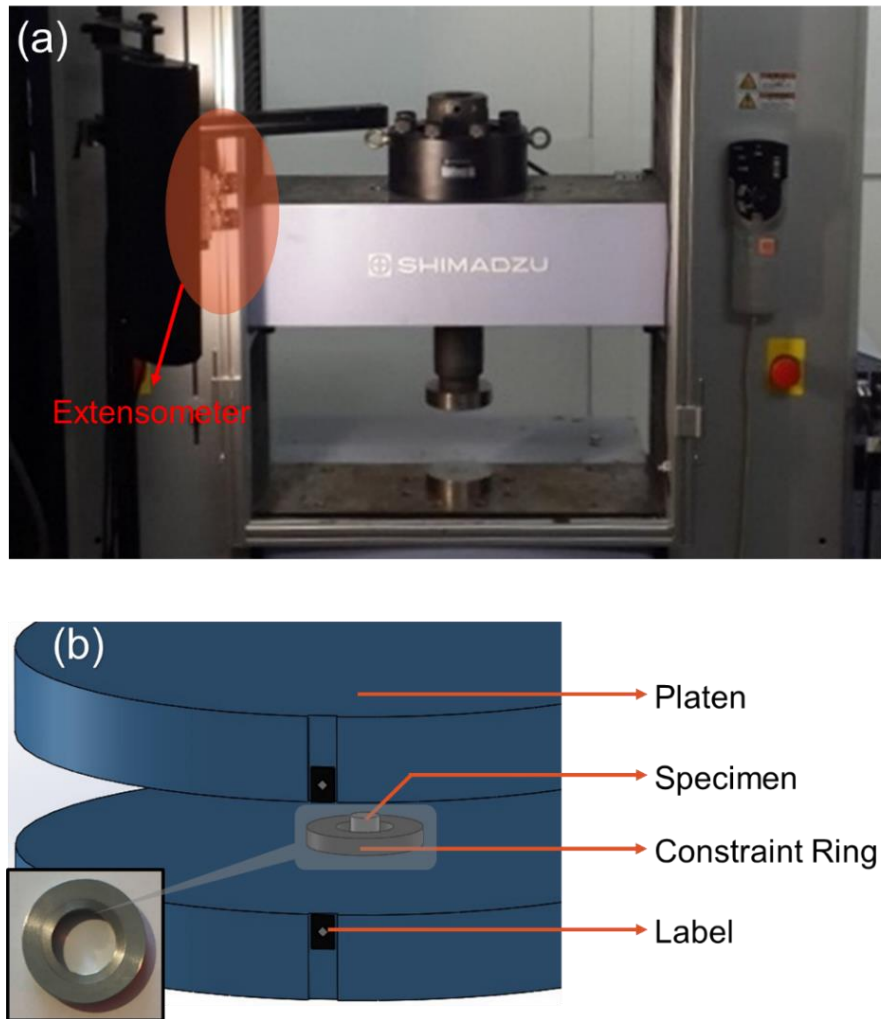


Figure 3.2. (a) the picture of test machine and (b) the details of test using strain-constraint ring.

### 3.3. High Strain Rate Compression Tests

High strain rate compression tests were performed in a compression type Split Hopkinson Pressure Bar (SHPB). The schematic of the used SHPB test system is shown in Figure 3.3. In a typical test, the specimen is sandwiched between incident and transmitter bars. Then, the gas gun is pressurized; upon releasing the gas pressure the

striker bar hits the end of incident bar, creating rectangular pulse on the incident bar. The pulse then proceeds at the bar/specimen interface where it is reflected as a tensile pulse to the incident bar and the rest is transmitted to the transmitter bar. The magnitudes of reflected and transmitted pulse depend on the mechanical impedance difference between specimen and bar. The strains on the bars are then measured using the strain gages mounted on incident and transmitter bars. The used SHPB set-up consisted of a 19.80 mm diameter Inconel 718 bar: 2000 mm-long incident bar, 1800 mm-long transmitter bar and is shown in Figure 3.4. The gas gun was filled with nitrogen using gas cylinders. The properties of bar material are as follows: elastic modulus=204 GPa, density=8200 kg m<sup>-3</sup> and yield strength= ~700 MPa. The stresses on the bars were measured by a full Wheatstone-bridge configuration of 350 Ω foil strain gages. After recording the waves using a oscilloscope and amplifies, the strain ( $\epsilon_s$ ), stress ( $\sigma_s$ ) and strain rate ( $\dot{\epsilon}_s$ ) of the specimen were using the following relations

$$\epsilon_s(t) = -\frac{2C_b}{L_s} \int_0^t \epsilon_R(t) dt \quad (3.5)$$

$$\sigma_s(t) = \frac{A_b}{A_s} E_b \epsilon_T(t) \quad (3.6)$$

$$\dot{\epsilon}_s(t) = -\frac{2C_b}{L_s} \epsilon_R(t) \quad (3.7)$$

where  $L_s$ ,  $A_b$ ,  $A_s$ ,  $E_b$ ,  $C_b$  and  $t$  are the length of specimen, the cross-sectional area of bar and specimen, elastic modulus and wave velocity of bar and time, respectively.  $\epsilon_R$  and  $\epsilon_T$  are sequentially the reflected and transmitted strains. In order to induce a gradually-rising incident wave, pulse shaping method is widely used. In this method, a thin layer of a ductile material is placed at the front of the incident bar (Figure 3.3) so that the deformation of the thin-metal layer in between the striker and incident bar shapes the incoming incident bar stress. In the present study, a copper sheet in 10x10x1 mm size was placed at the front of the incident bar by applying a thin layer of lubricant. In order to constrain the final strain of specimen, a tool steel ring was also used in the SHPB tests. Figure 3.3(a) shows typical voltage-time readings of a SHPB test with and without using a pulse shaper and Figure 3.3(b) with the use of the strain constraint ring. The pulse-shaper induces, as seen in Figure 3.3(a), a more gradually rising stress wave on the

incident bar and also results in lesser variations of the strain rate during the testing. In classical SHPB tests, the strain gages on the incident and transmitter bar are placed at an equal distance from the specimen/bar interfaces so that the reflected and transmitter pulses start at the same point in the time domain. This requires a separate record of incident and reflected pulses. The use of pulse shaper however increases the time duration of the incident pulse, resulting in an interaction of the end of the incident pulse and the start of the reflected pulse. In order to measure the incident and reflected wave separately a strain gage 1 in Figure 3.3(a) is placed on the incident bar to measure the incident and reflected pulse separately. In this case, the strain gage 1 reading is shifted in the time axis to the starting time of the transmitter pulse in order to make classical SHPB data reduction (Figure 3.3(a)). The use of two strain gages on the incident bar of the used SHPB allows to measure the wave dispersion of pulse. The similar pulse profiles measured from two strain gages show negligible pulse dispersion effect on the Inconel bar. After the specimen is compressed until about the prescribed strain level, the ring and specimen are deformed together as depicted in Figure 3.3(b). Since the impedance of the tool steel ring is large, an elastic strain is formed on the specimen when the tool steel is compressed together with specimen. As soon as the ring is compressed as seen in Figure 3.3(b), the reflected wave becomes zero; incoming wave is fully transmitted to the transmitter bar. By this way, the specimen was deformed until about 10, 20, 30 and 40% engineering strains in the SHPB tests.

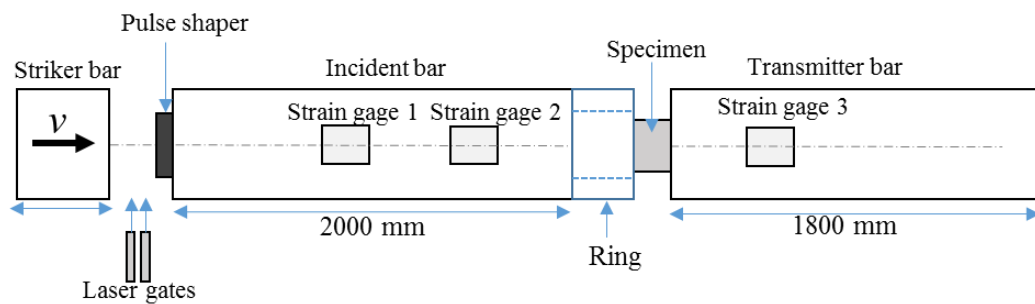
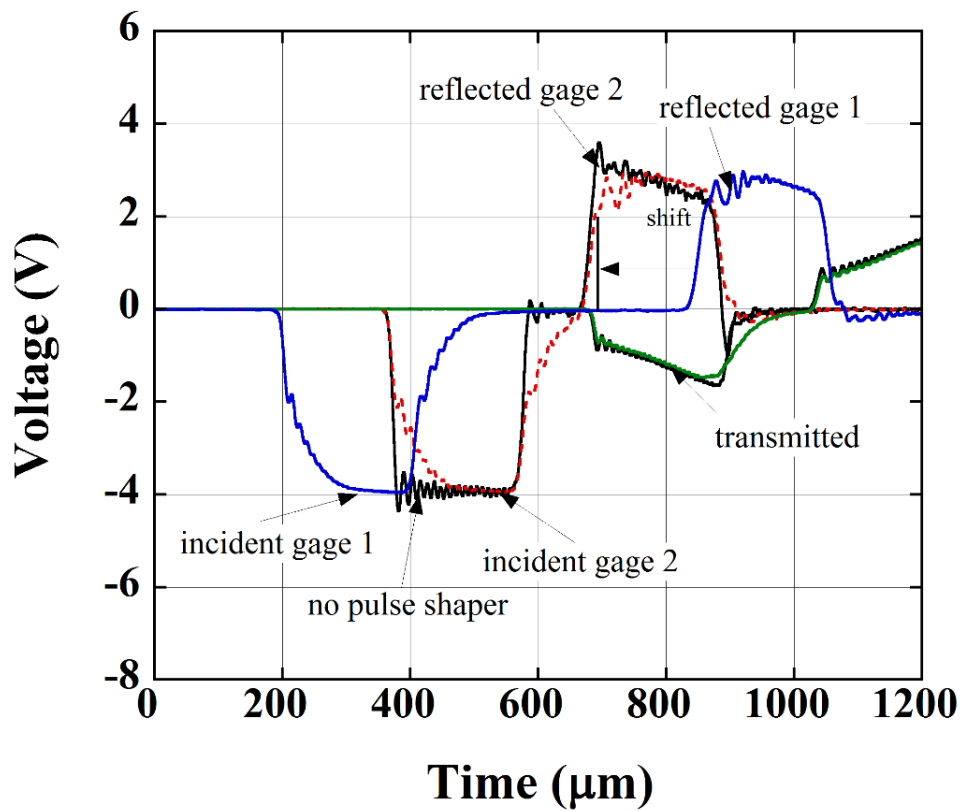


Figure 3.3. The schematic of SHPB test system.



Figure 3.4. The picture of the used Inconel SHPB set-up.



(a)

(cont. on next page)

Figure 3.5. Typical voltage-time readings of a SHPB test (a) with and without using a pulse shaper and (b) with the use of use strain constraint ring.

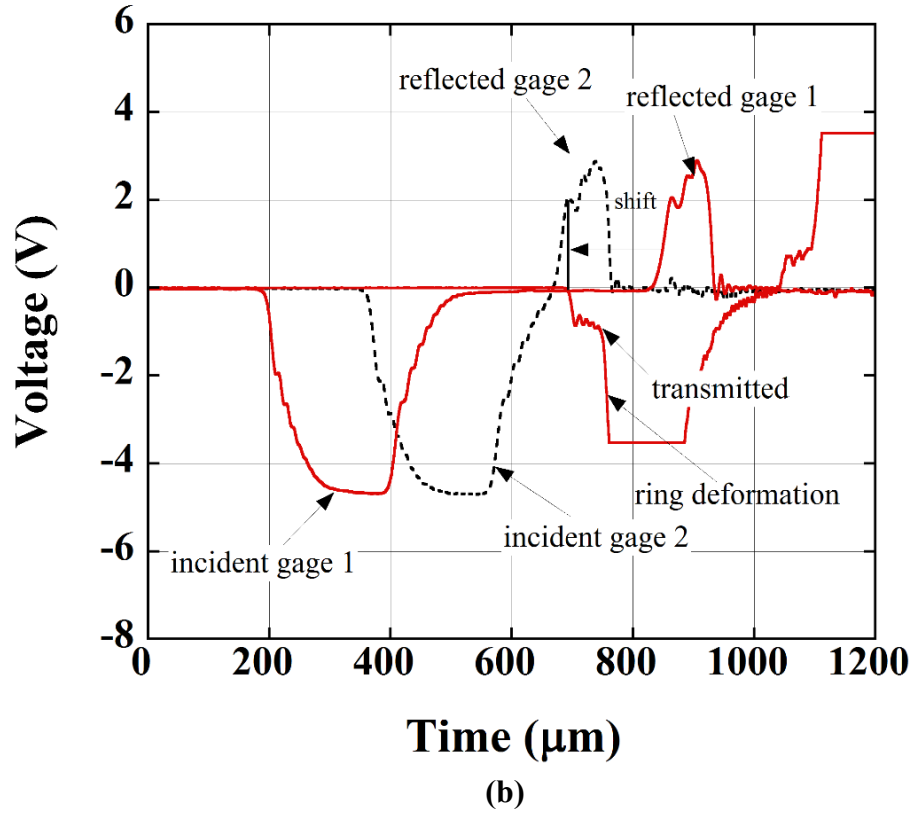


Figure 3.5. (cont.)

### 3.4. Material Characterization

The density of SLM-316L and C-316L specimens were determined by the Archimedes method as

$$\rho = \frac{w_{air}\rho_{water}}{w_{air} - w_{water}} \quad (3.8)$$

where,  $\rho$  is the density and  $w$  is the weigh. The percent porosity of SLM-316L (%P) was calculated as

$$\%P = 100 \times \left(1 - \frac{\rho}{\rho_b}\right) \quad (3.9)$$

where,  $\rho_b$  is the density of bulk C-316L specimen.

X-ray Diffraction (XRD) was used to determine the crystallographic structure and phase quantification of untested and compression tested SLM-316L and C-316L specimens. XRD analysis was performed in a Philips X'Pert Pro X-Ray Diffraction device using CuK $\alpha$  radiation ( $\lambda=1.54 \text{ \AA}$ ) at 40 kV. The XRD analysis was carried from 40 to 150° interval at a 0.02°s<sup>-1</sup> scanning rate. The weight percentage of the martensite in C-316L specimens was determined by the Rietveld profile refinement method <sup>75</sup> using a High Score X'pert program <sup>76</sup>. This method is based on monitored intensities in an XRD pattern. A least-squares approach is used to refine a theoretical background profile until it matches the measured pattern profile. The integrated intensities of individual peaks for each phase in the alloy or mixture are determined to calculate weight percentages. The dislocation density and lattice micro-strain of SLM-316L and C-316L specimens were measured using Williamson-Hall method <sup>77</sup>.

$$\beta - \beta_{ins} = \delta_{hkl} \cos\theta_{hkl} = \frac{\lambda}{D} + 4\epsilon \sin\theta_{hkl} \quad (3.10)$$

where,  $\lambda$  is the XRD wavelength (0.154 nm),  $D$  is the grain size,  $\epsilon$  is the lattice microstrain,  $\delta_{hkl}$  is the broadening of full width at half maximum (FWHM) of XRD spectra peak,  $\theta_{hkl}$  is the diffraction angle and  $\beta_{ins}$  is the broadening of instrument. The broadening of instrument was calculated through the XRD of an unstrained Si powder and determined 0.38. If the strain value gets equate from the equation, the slope of the equation curve gives the lattice micro-strain as

$$\epsilon = \frac{FWHM \cos\theta_{hkl}}{4 \sin\theta_{hkl}} \quad (3.11)$$

The dislocation density ( $\rho_{disloc}$ ) was calculated using the formula given below <sup>78</sup>

$$\rho_{disloc} = k \frac{\epsilon^2}{b^2} \quad (3.12)$$

where,  $k$  is a constant (16.1 for FCC) and  $b$  is the Burgers' vector ( $2.55 \times 10^{-10}$  m for FCC iron) <sup>78</sup>.

The untested and tested specimens were cut by using the IsoMet 4000 precision saw under a continuous flow of water for metallographic analysis. The cylindrical

compression tests specimens were cut through three different planes (normal to z-, y- and z-axis), as shown in Figure 3.6, in order to determine the direction-dependent microstructural development and also to make hardness tests in each plane. The cut slices were then mounted in Bakelite. Mounted samples were the grinded by using 2500P grit grinding paper and then sequentially polished down to  $0.25\ \mu\text{m}$  using diamond suspensions. The metallographic samples were etched using a solution composing of 2% HF and 8%  $\text{HNO}_3$ . The polished samples were immersed into etchant for 20 min.

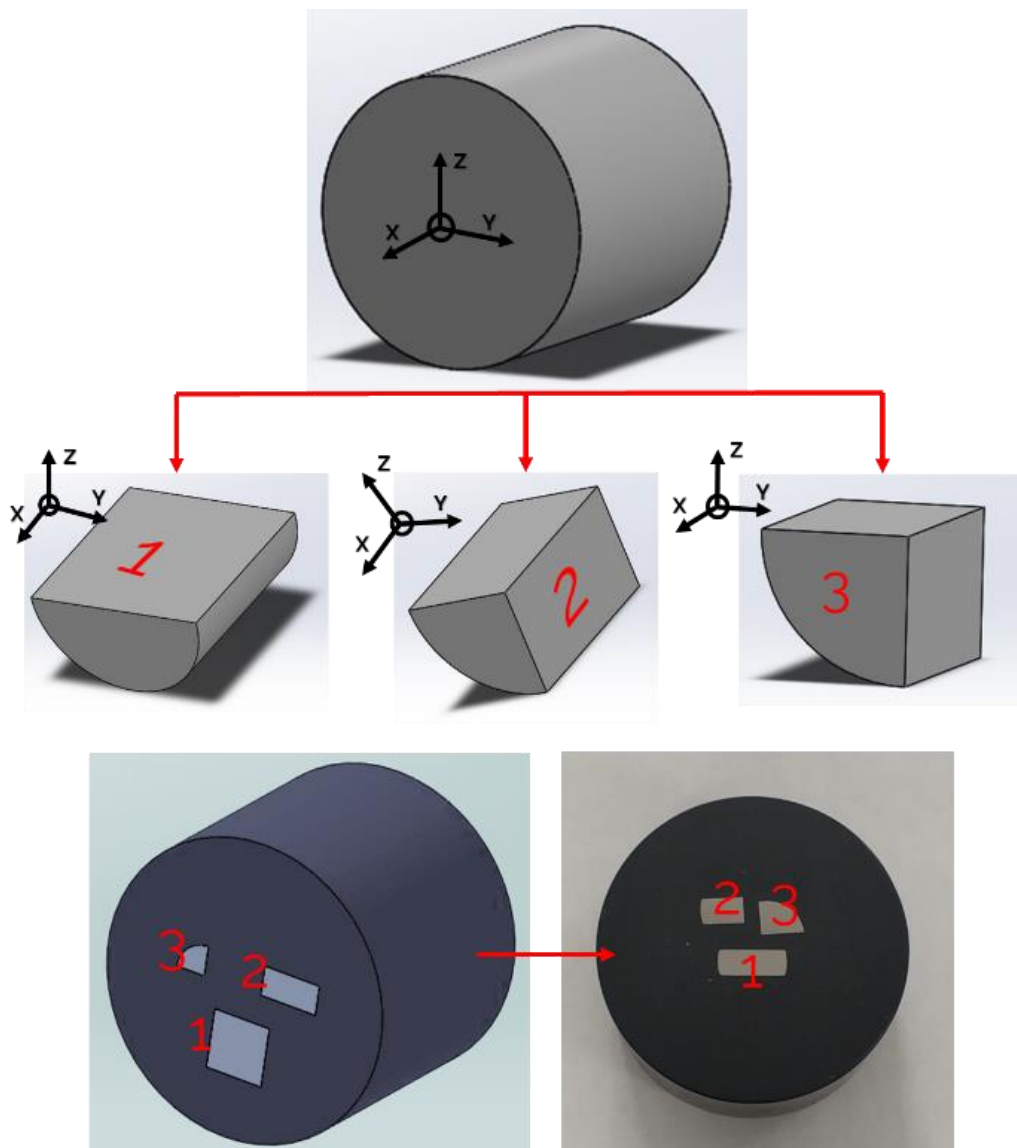


Figure 3.6. The compression tests specimen slicing in three different plane and coding of the planes in Bakelite mounted samples.

After polishing and before etching process of the specimens, Electron backscatter diffraction (EBSD) analyzes were performed by Central Laboratory at METU. The raw data obtained from EBSD were analyzed using ATEX software <sup>79</sup>. The microstructural observations were performed using a Meiji IM7 100 optical microscope and an FEI QUANTA 250 FEG Scanning Electron Microscope (SEM) in Backscattered electron (BSED) mode using Circular Backscatter Detector (CBS).

The grain sizes of the alloys were determined by the Heyn Intercept Method <sup>80</sup>. In this method, horizontal lines are drawn in the optical images taken from randomly selected polished-etched surfaces so that there are at least fifty intersections in total. Then the number of intercepts of the lines with grain boundaries are counted. An example of the used method is shown in Figure 3.7. The total number of intercepts was finally divided by the total length of the lines to determine the average grain size.

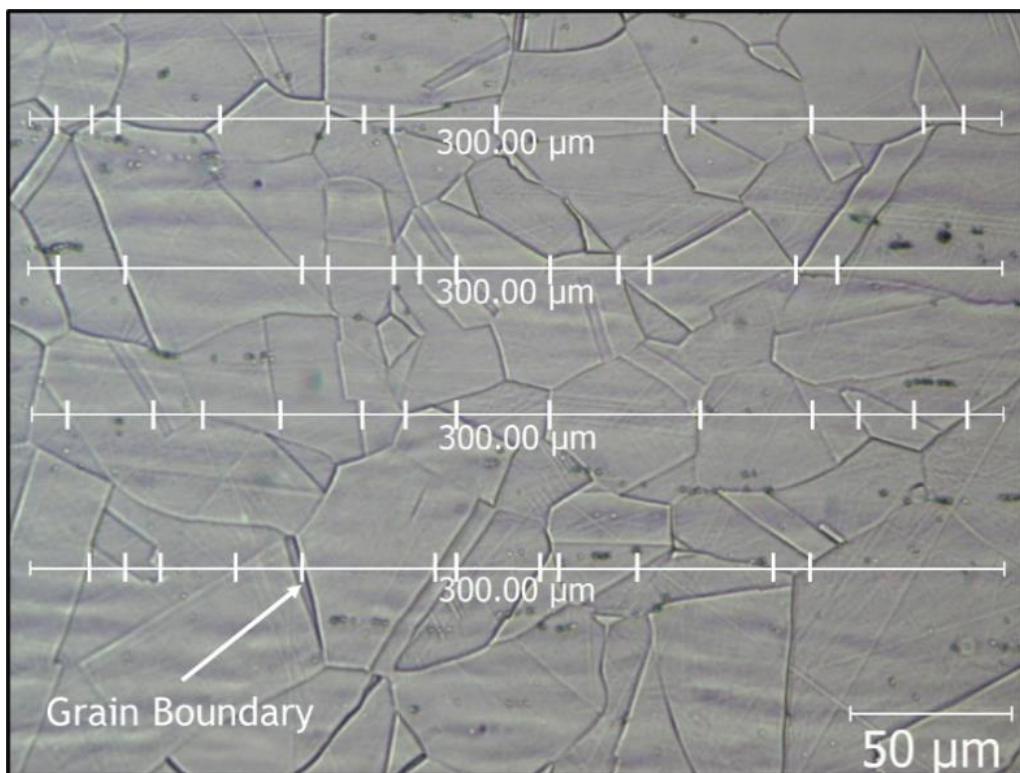


Figure 3.7. The intercept method for the determination of average grain size.

Hardness Vickers (HV) tests were performed in a Shimadzu Micro Vickers Hardness Tester both on the polished and polished-etched surfaces of the metallographic specimens. The tests were performed between 0.49N (HV0.05) and 19.61 N (HV2) for 10 ms and repeated 10 times. The optical image of indentation was transferred to an image

program in which the lengths of the indentation diagonals were measured (Figure 3.8). The HV was calculated as

$$HV = 0.189 \frac{P}{\left(\frac{L_1+L_2}{2}\right)^2} \quad (3.13)$$

where,  $L_1$  and  $L_2$  are the length of the diagonals (Figure 3.8) and  $P$  is the applied load.

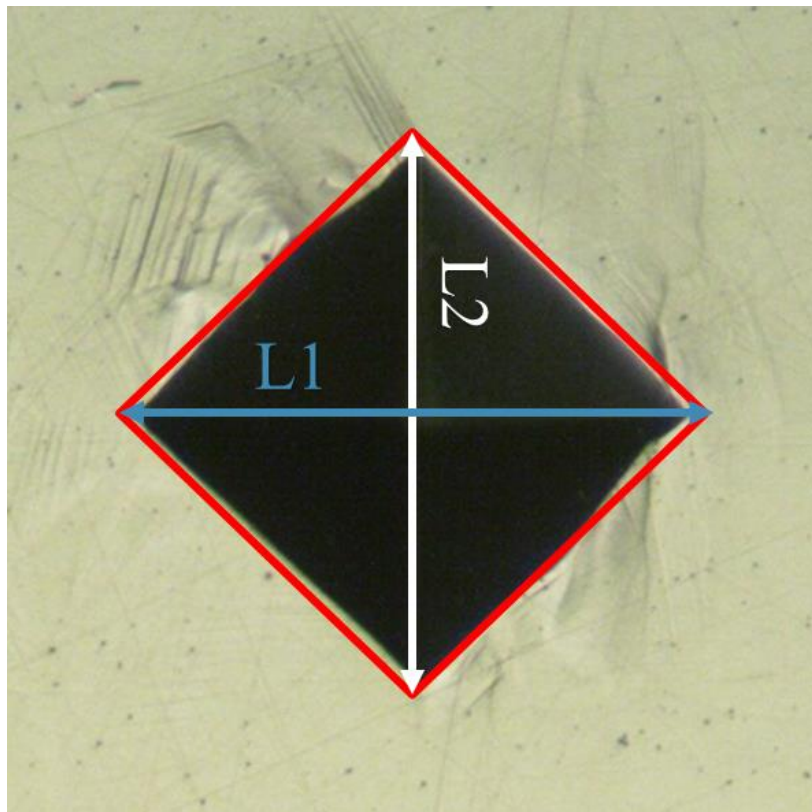


Figure 3.8. HV indentation and the measured indentation lengths.

## CHAPTER 4

### RESULTS AND DISCUSSION

#### 4.1. Microstructural Characterizations of Untested Specimens

The average densities of SLM-316L and C-316L specimens were calculated  $7821 \pm 5$  and  $7838 \pm 5 \text{ kg m}^{-3}$ , respectively. The percent porosity of SLM-316L was determined 0.22%. A relative density over 99.5% was reported for an SLM-316L alloy processed using the similar processing parameters <sup>14</sup>.

The optical microscope pictures of the microstructures of SLM-316L processed by higher and lower laser power in the perpendicular to the building direction samples are shown in Figures 4.1 (a-b), respectively. The higher laser power processed alloy has a hatch spacing of  $115 \text{ }\mu\text{m}$  and the lower laser processed alloy has a hatch spacing of  $95 \text{ }\mu\text{m}$ . In the biaxial plane, as seen in the Figure 4.1 (a), two neighboring layers are  $90^\circ$  to each other, resulting from the biaxial scanning strategy. Nearly equal-axed  $20\text{-}60 \text{ }\mu\text{m}$  size grains were observed inside the melt pools of the biaxial plane. As the new melted layer solidifies at the top of the already solidified layer, a columnar grain structure was observed in the building direction. This results in a crystallographic fiber texture of  $\langle 100 \rangle$  in the building direction <sup>38,43,45</sup>. Rotating scanning breaks the epitaxy of columnar growth <sup>81</sup>. The broken columnar grains of the studied SLM-316L alloy are shown by dotted lines across the melt pools in Figures 4.1(c) and (d). The average width of these broken grains (grain size) was determined by intercept method, almost the same for the higher and lower laser power processed SLM-316L alloys,  $30.3$  and  $29.3 (\pm 1.5) \text{ }\mu\text{m}$ , respectively. A sub-grain structure is formed inside broken columnar grains, which is resulted from the rapid cooling <sup>38,39,82</sup> in the SLM process as shown in Figures 4.1 (e) and (f). The average size of sub-grains was determined by measuring at least 100 sub-grains and found  $1.05 \pm 0.2$  and  $0.65 \pm 0.1$  for the higher and lower laser power processed alloys, respectively. Sub-grains are also noted to cross the melt pool boundaries, as also reported previously <sup>47,53</sup>. Sub-grains are the high dislocation density regions and contains a high density of solute atoms such as Cr and Mo <sup>82</sup>. Moreover, these sub-grains were reported to be weak obstacles to dislocation motions <sup>38,47</sup>.

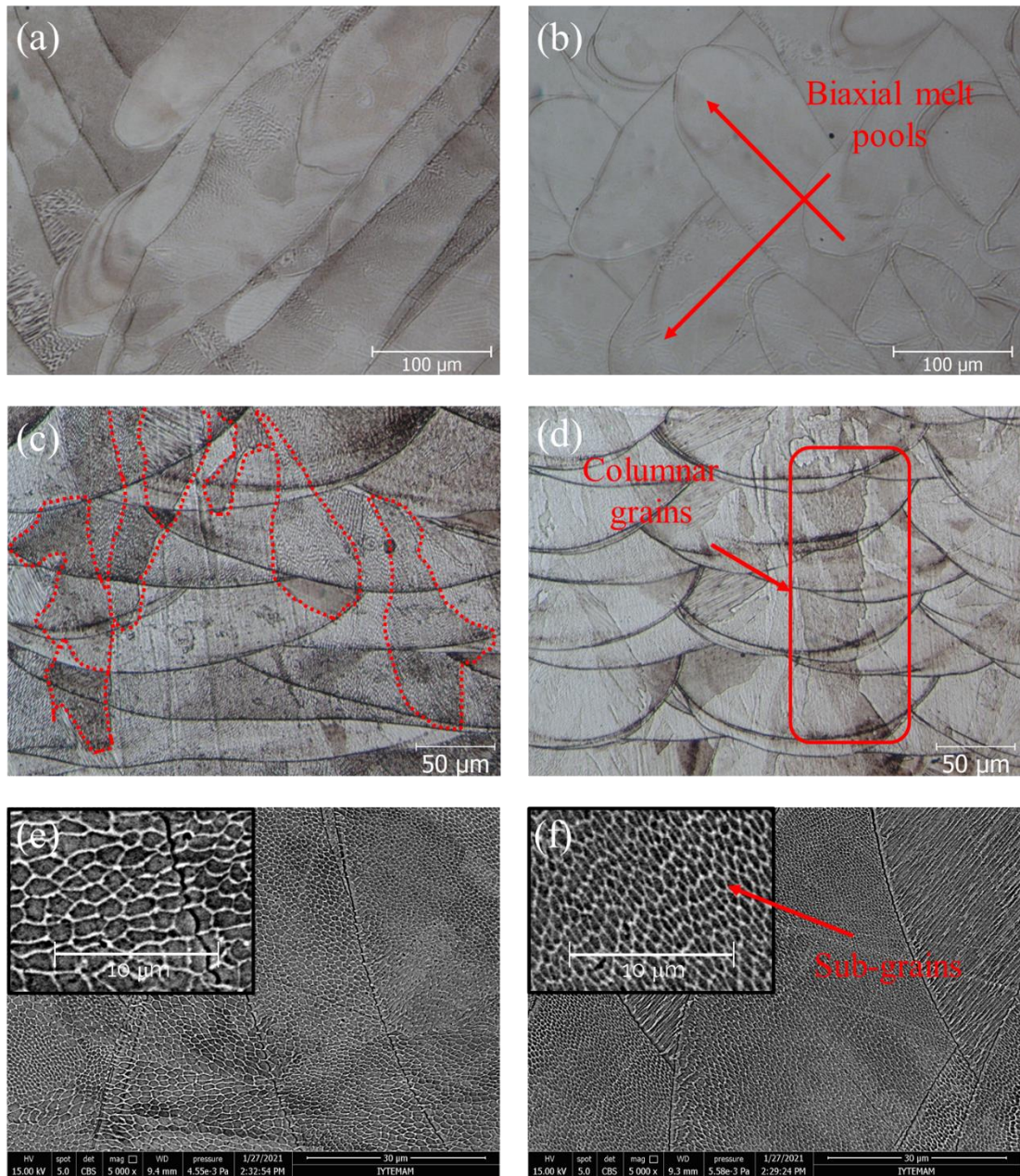


Figure 4.1. The optical microscopy pictures of SLM-316L: normal to the z-axis a) higher laser power and b) lower laser power processed alloy, parallel to the z-axis c) higher laser power and d) lower laser power processed alloy and the SEM picture of sub-grains structure e) higher laser power and f) lower laser power processed alloys.

The optical microscope pictures of the microstructure of C-316L in parallel and perpendicular to the extrusion direction are seen in Figures 4.2(a-b). The microstructure is composed of polygonal grains, with almost the same grain sizes in parallel and perpendicular to the extrusion direction. The average grain size of C-316L was determined 24.3  $\mu\text{m}$  by the linear intercept method.

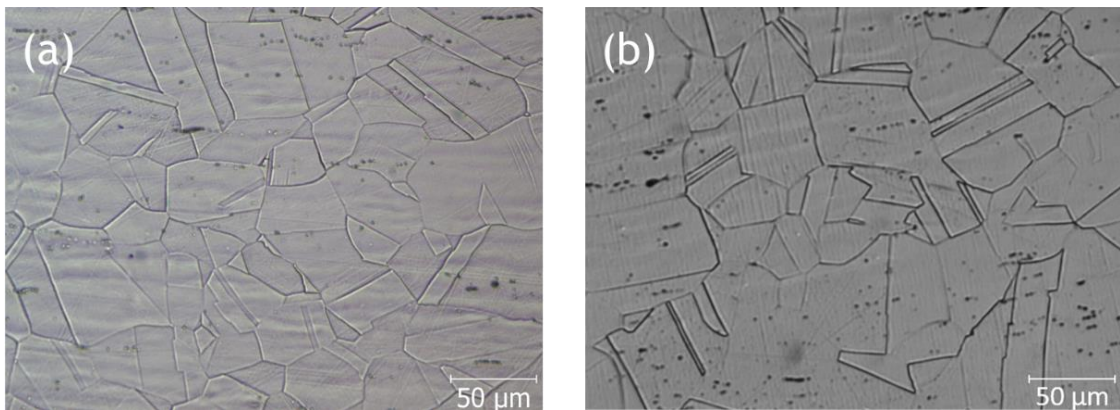


Figure 4.2. The optical pictures of C-316L in (a) parallel and (b) perpendicular to the extrusion direction.

The untested XRD spectra of SLM-316L and C-316L alloys are shown together in Figure 4.3. Both alloys have an austenitic ( $\gamma$ ) structure, while C-316L alloy contains 2.6 wt% martensite in the as-received form determined by the Rietveld method. The martensite phase ( $\alpha'$ ) is presumably formed during annealing following the extrusion process. Furthermore, the relatively high peak intensity of the (111) plane of SLM-316L alloy (Figure 4.3) is consistent with the previously reported XRD spectra of an SLM-316L alloy processed by a similar rotating scanning strategy<sup>11, 12, 41</sup>. The residual strain calculated using Williamson and Hall method is found 0.23% as shown in the inset of Figure 4.3. The dislocation density was calculated using Eqn. 3.11 and determined  $1.04 \times 10^{15} \text{ m}^{-2}$ . A slightly higher dislocation density,  $1.18 \times 10^{15} \text{ m}^{-2}$ , was previously determined in an SLM-316L as-built specimen which was fabricated using a multidirectional biaxial scanning laser pattern rotated  $70^\circ$  between adjacent layers<sup>82</sup>. Another study reported a similar dislocation density,  $\sim 1.14 \times 10^{15} \text{ m}^{-2}$ , for an SLM-316L alloy processed by a bidirectional scanning strategy at a  $100 \text{ J mm}^{-3}$  laser energy density<sup>37</sup> which is slightly smaller than that of the present study ( $120 \text{ J mm}^{-3}$ ).

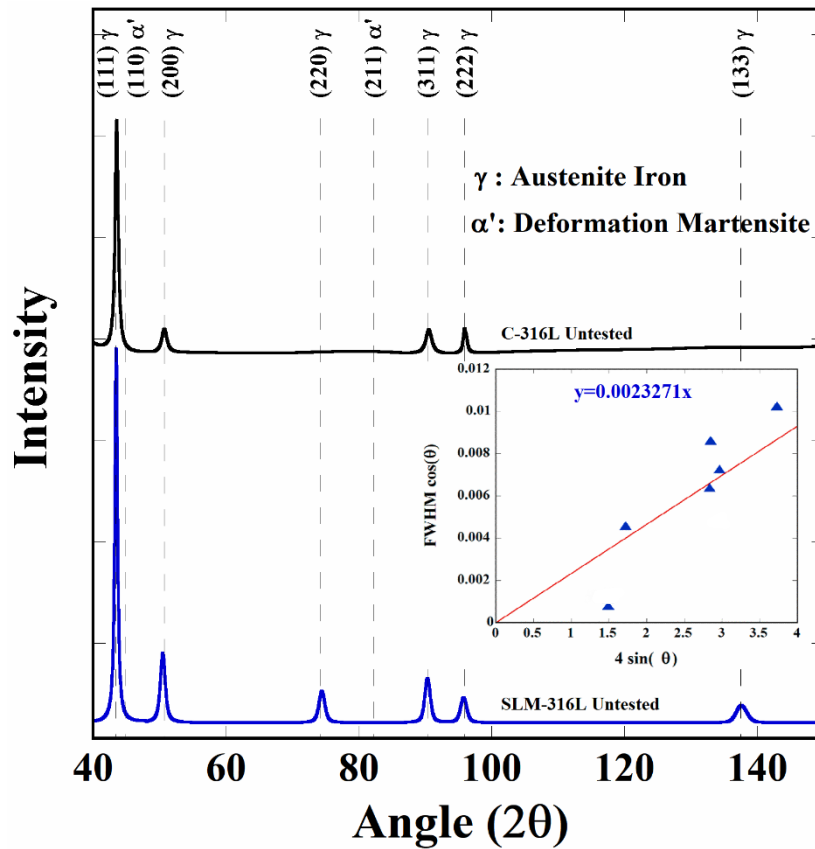


Figure 4.3. The XRD spectra of untested C-316L and SLM-316L.

The average hardness of untested SLM-316L and C-316L alloys in different directions are tabulated in Table 4.1. The hardness of SLM-316L specimens in the x- and z-direction are different as seen in the same table; a higher hardness is found in the x-direction than the z-direction, showing an anisotropy between x- and z-direction. The anisotropy is likely due to the texture, the difference in the grain morphologies and sizes<sup>12</sup>. As will be elaborated next section, a strong  $\langle 110 \rangle$  fiber texture formed along the building direction, which made both the slip and twin deformation easier in the building direction. The columnar grain width in the x-direction is also smaller than in the z-direction. The hardness of SLM-316L processed by higher and lower laser power are however quite similar to each other in the x-direction, the former one shows a slightly higher average hardness (2305 MPa) than the latter one (2285 MPa). Despite the similar grain sizes, the hardness of SLM-316L alloy is considerably higher than that of C-316L as tabulated in Table 4.1. In previous investigations, it was reported that the high hardness of additively manufactured 316L as compared with C-316L was due to the initial higher dislocation density<sup>37, 38</sup>. Also, the hardness of C-316L alloy in the perpendicular and

parallel to the extrusion direction are very much similar to each other (2099 and 2092 MPa, respectively), proving nearly isotropic properties of the tested C-316L alloy.

The variations of average hardness and the hardness calculated from diamond indentation lengths (L1 in the y-axis and L2 in the z-axis) along the height of the SLM-built rectangular bar are shown in Figure 4.4. The average hardness values seen in the same table are higher in the layers near the support (bottom). The faster cooling rate in the part near the bottom support may result in higher hardness as also mentioned elsewhere <sup>11</sup>. But the average hardness almost become the same along the height of the bar after a 25 mm from the bottom, as depicted in Figure 4.4. It is noted that the hardness values of L1 and L2 are almost the same at the bottom layers, but they differ at the upper sections. The higher hardness of the y-axis than that of the z-axis is clearly seen in the upper sections. This further confirms the anisotropy between the x- and z-directions.

Table 4.1. The average hardness of SLM-316L & C-316L.

Specimen & Direction	HV2 (MPa)
SLM-316L - normal to the z-axis	2173±75
SLM-316L (higher power) - parallel to the z-axis	2307±91
SLM-316L (lower power) - parallel to the z-axis	2284±77
C-316L - perpendicular to the extrusion direction	2099±48
C-316L - parallel to the extrusion direction	2092±57

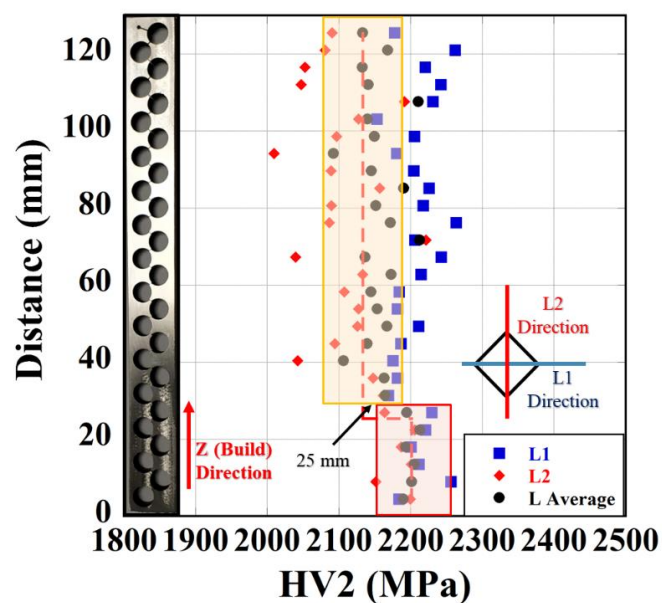


Figure 4.4. Hardness values in SLM-316L rectangular bar along the build direction.

The hardness of SLM-316L at different hardness loads are drawn as function of the depth of penetration (DoP) in Figure 4.5(a) for the x- and z-axis. As the DoP decreases the hardness increases for both directions. A higher hardness in the z-direction than perpendicular to the z-direction is seen in the same figure. A similar trend of increased hardness with the decrease of DoP is also seen in the average hardness values of C-316L, but the average hardness of C-316L alloy approaches the average hardness of SLM-316L alloy at lower DoP in the x-direction as seen in Figure 4.5(b).

In order to see the effect of sub-grains and grain size on the hardness, hardness tests were performed in the x-direction at two different loads, HV2 and HV0.05, on the SLM-316L specimens processed with the higher and lower laser power. The pictures of HV indentation are shown in Figures 4.6(a-d). The lower HV load imposes an indentation within a grain, while the higher HV load over several grains as shown in Figures 4.6(a-d). The hardness variations with the DoP are shown in Figure 4.7. The average HV2 hardness are  $2306 \pm 91$  and  $2284 \pm 77$  MPa for the alloy processed with the higher and lower laser power, respectively. The average HV0.05 hardnesses are  $2806 \pm 64$  and  $2770 \pm 166$  MPa for the alloy processed with the higher and lower laser power, respectively. These results clearly indicated that both SLM-316L structures have similar hardness despite the fact that they have different sub-grain sizes,  $1.05 \pm 0.2$  and  $0.65 \pm 0.1$   $\mu\text{m}$ , respectively.

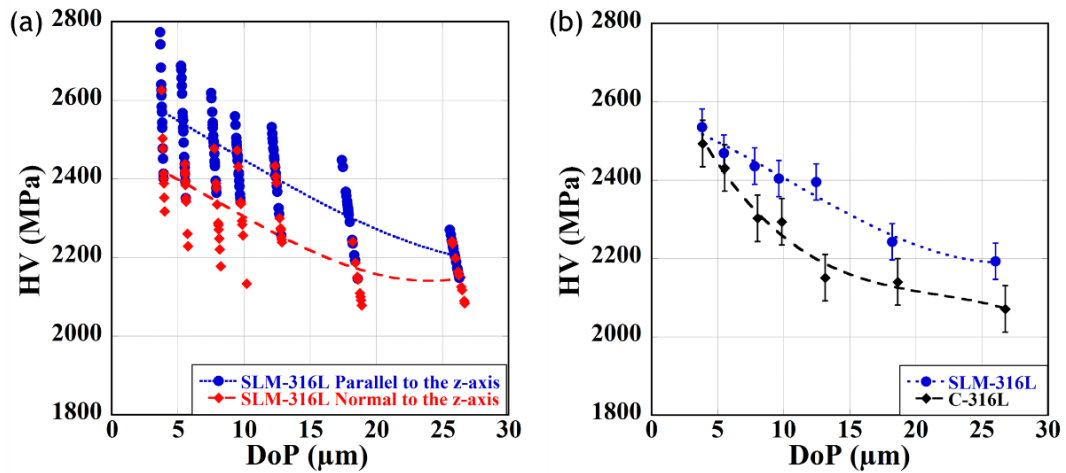


Figure 4.5. At different loads, (a) hardness values of SLM-316L and (b) average hardness values of SLM-316L and C-316L.

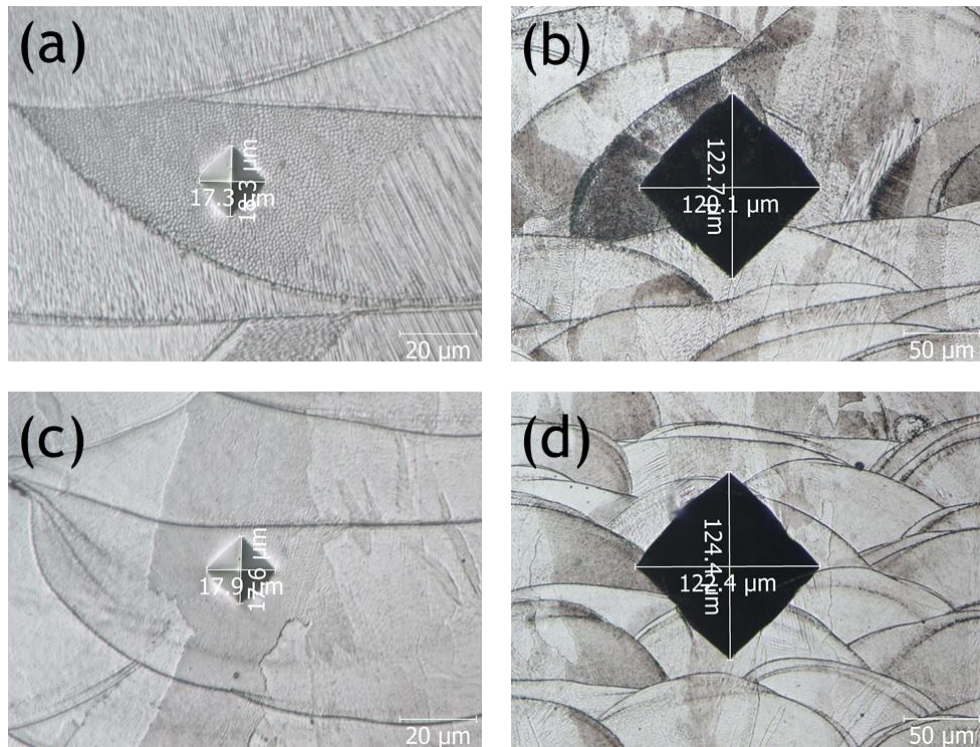


Figure 4.6. Higher laser power processed specimen at (a) HV0.05 and (b) HV2 hardness test and lower laser power processed specimen at (c) HV0.05 and (d) HV2 hardness test.

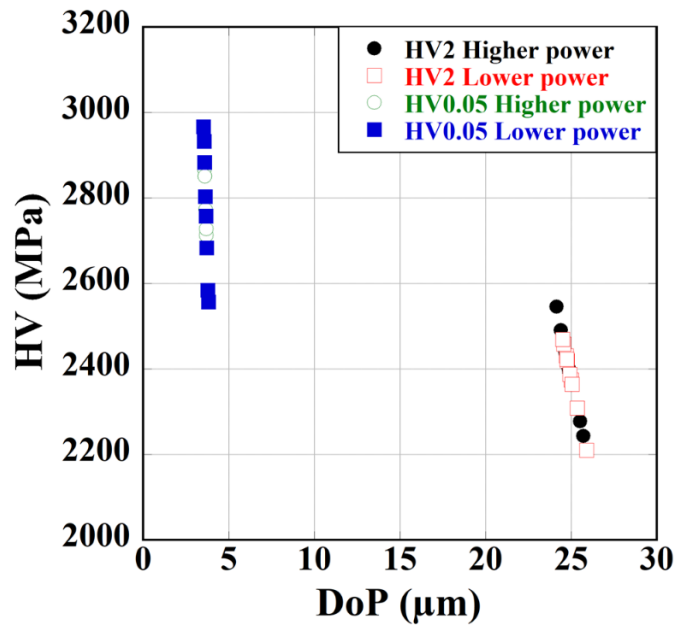


Figure 4.7. SLM-316L processed with higher and lower laser power tested at HV2 and HV0.05 loads.

The EBSD maps of specimens perpendicular and parallel to the build direction are shown in Figure 4.8(a). In a previous study, a strong fiber texture of  $\langle 110 \rangle$  along the build direction (z-axis) and a weak  $\langle 111 \rangle$  texture or random distribution of perpendicular to the building direction (x- and y-axis,  $\pm 45^\circ$  to the scanning directions) of SLM-316L specimens were shown for rotating scanning strategy<sup>12</sup>. Similarly, fiber texture is also found in this study. A strong  $\langle 110 \rangle$  fiber texture along the building direction, while a weak  $\langle 111 \rangle$  texture or nearly random distribution of directions are shown in the x- and y-axis as depicted in Figures 4.8(b) and (c). The average grain sizes in perpendicular to the build direction and parallel to the build direction were determined 32.5 and 22  $\mu\text{m}$  in the EBSD analysis respectively, which are comparable with the grain size measured by the intercept method.

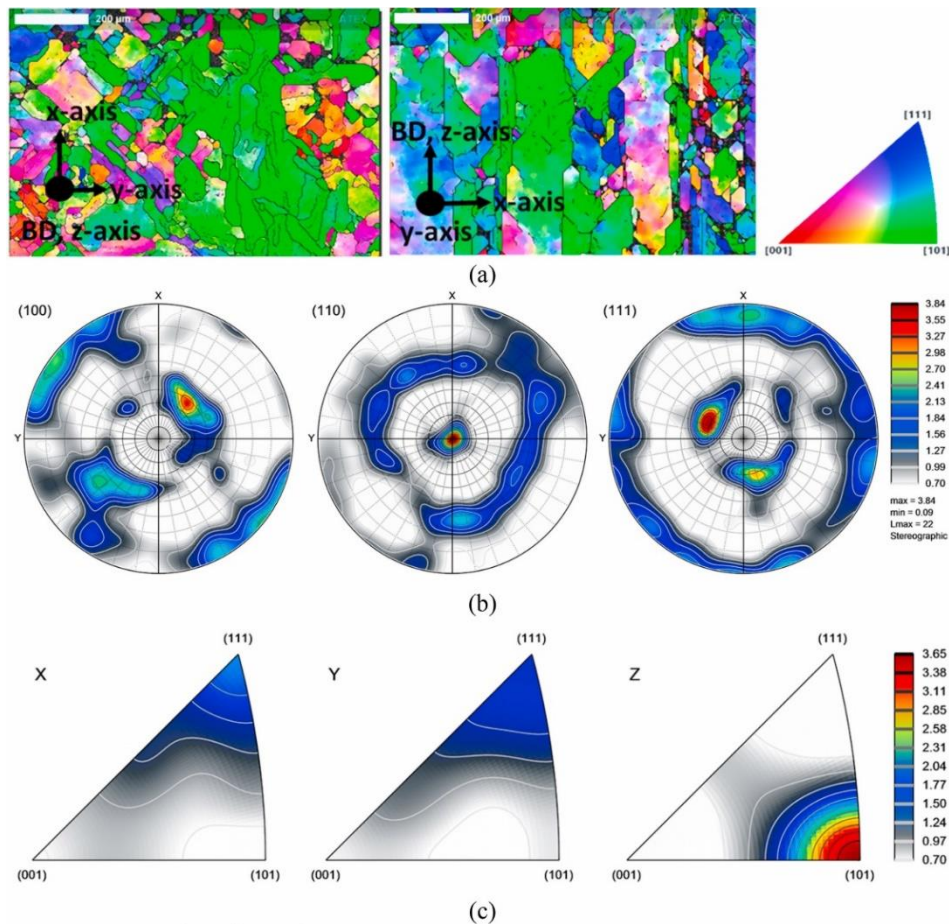


Figure 4.8. (a) EBSD maps in the tensile axis of  $0^\circ$  and  $90^\circ$  inclined specimens, (b) pole figures for  $0^\circ$  inclined specimen perpendicular to building direction (normal to z-axis), and (c) inverse pole figures showing  $\langle 110 \rangle$  fiber texture in the z-axis.

## 4.2. Quasi-Static Compression Tests

Quasi-static compression true stress-strain curves of SLM-316L and C-316L are shown together in Figure 4.9. As noted, and shown by arrows in the same figure, the deformation stops, when the ring deformation starts at the final true plastic strains of 0.11, 0.22, 0.36 and 0.51, sequentially corresponding to 0.1, 0.2, 0.3 and 0.4 engineering strains. Both alloys show similar compression true stress-true strain behavior, following an elastic region, the specimens are deformed plastically until about 0.51 true plastic strain without cracks and failure. However, the work hardening rate of C-316L is higher than that of SLM-316L as noted in Figure 4.9. And the stresses of C-316L approach to those of SLM-316L at the strains above about 0.51. The higher work hardening of C-316L was also noted in previous studies and this was ascribed to the differences in the deformation behavior between SLM-316L and C-316L<sup>13,36</sup>. On the other side, SLM-316L specimens have a higher average yield strength,  $510 \pm 10.2$  MPa, than C-316L,  $360 \pm 11.6$  MPa. A higher yield strength of SLM-316L was also previously reported<sup>31,37</sup>.

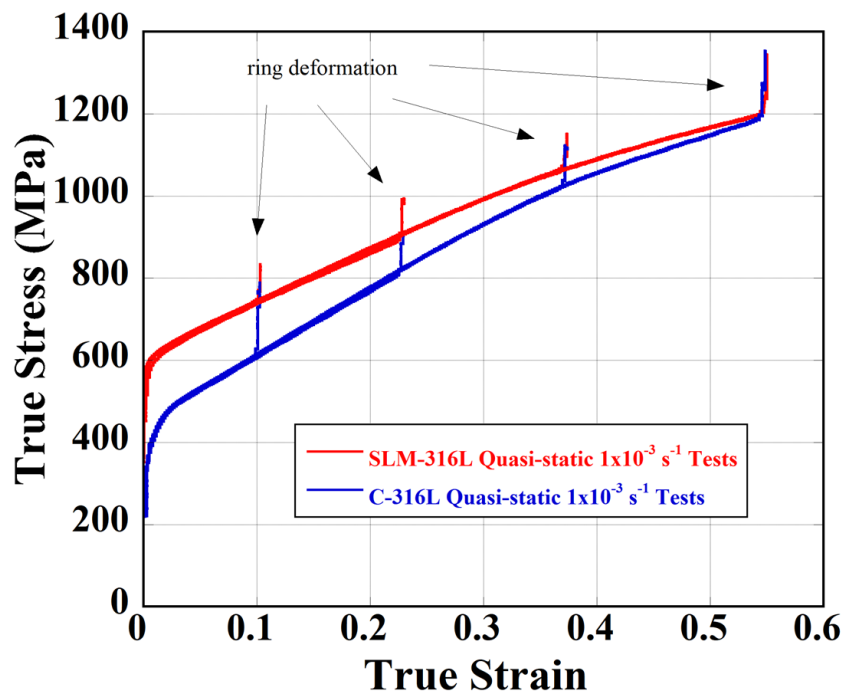


Figure 4.9. Quasi-static ( $1 \times 10^{-3} \text{ s}^{-1}$ ) compression true stress-strain curves of SLM and C 316L.

Figures 4.10(a-b) and Figures 4.11(a-b) show the optical and SEM pictures of SLM-316L and C-316L specimens deformed until about 0.36 strain, respectively. As clearly seen in these pictures, SLM-316L by the twin-dominated deformation and C-316L deforms by the martensite-dominated deformation. Note that deformation twins and martensite are very similar morphologically. As seen in Figures 4.11(a-b), both deformation types do not pass the grain boundaries. While twin deformation exceeds the sub-grain boundaries and melt pool boundaries, even it bends the sub-grain boundaries as seen in Figure 4.10(a) and Figure 11(a). The distance between twinned regions and the distance between twins and martensite were measured as function of true strain from the SEM micrographs. The distance between twinned regions decreases from 6.5-8  $\mu\text{m}$  with a thickness of  $\sim 1 \mu\text{m}$  at 0.11 strain, to 3.5-4  $\mu\text{m}$  with a thickness of  $\sim 1.2 \mu\text{m}$  at 0.22 strain, to 1.5-2.5  $\mu\text{m}$  with a thickness of  $\sim 1 \mu\text{m}$  at 0.36 strain and to less than 0.7  $\mu\text{m}$  at 0.51 strain (Figures 4.12(a-d)). The distance between twinned regions slightly decreases as the strain increases. The fraction of twinned grains also increases with increasing strain. The distance between martensite plates was measured  $\sim 1 \mu\text{m}$  and did not change with strain (Figures 4.13(a-d)).

The dislocation density strengthening of was calculated using the Taylor equation given below

$$\sigma = M\alpha Gb\sqrt{\rho} \quad (4.1)$$

In Equation 4.1,  $M$  is Taylor factor (2.9),  $\alpha$  is empirical constant (0.23) and  $G$  is shear modulus (85 GPa)<sup>83</sup>. By taking the average dislocation density of C-316L alloy  $3.8 \times 10^{14} \text{ m}^{-2}$ <sup>84</sup>, the dislocation density strengthening was determined 261 MPa using Eqn. 4.1. The high yield strength and hardness of the studied SLM-316L alloy as compared with the yield strength of C-316L may be therefore considered due to the process-inherited higher dislocation density.

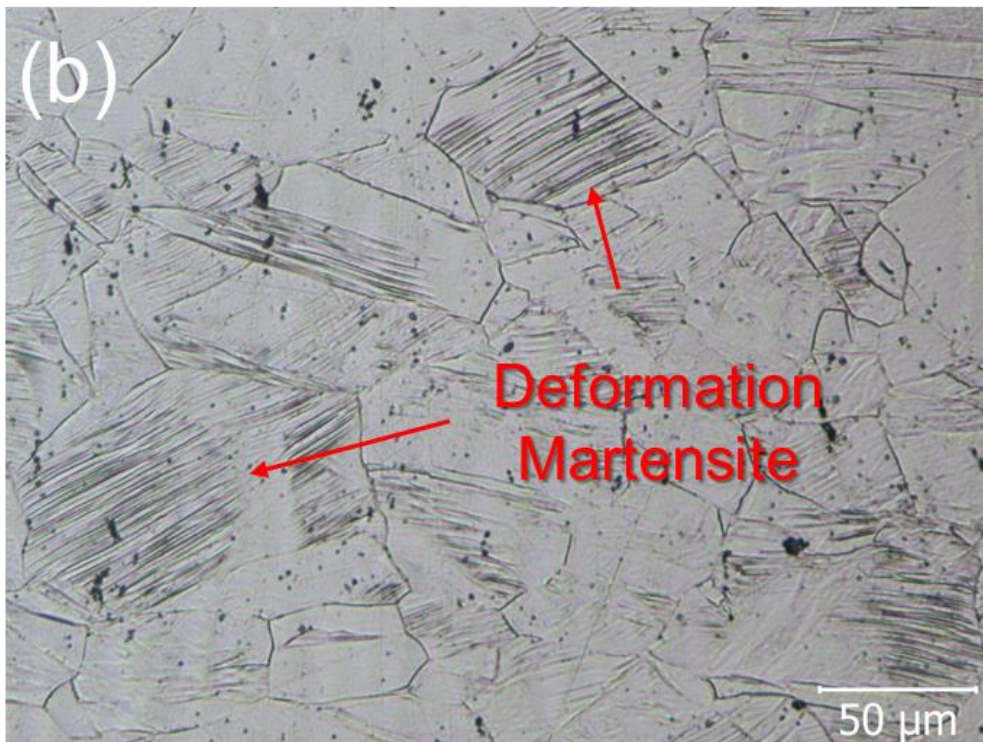
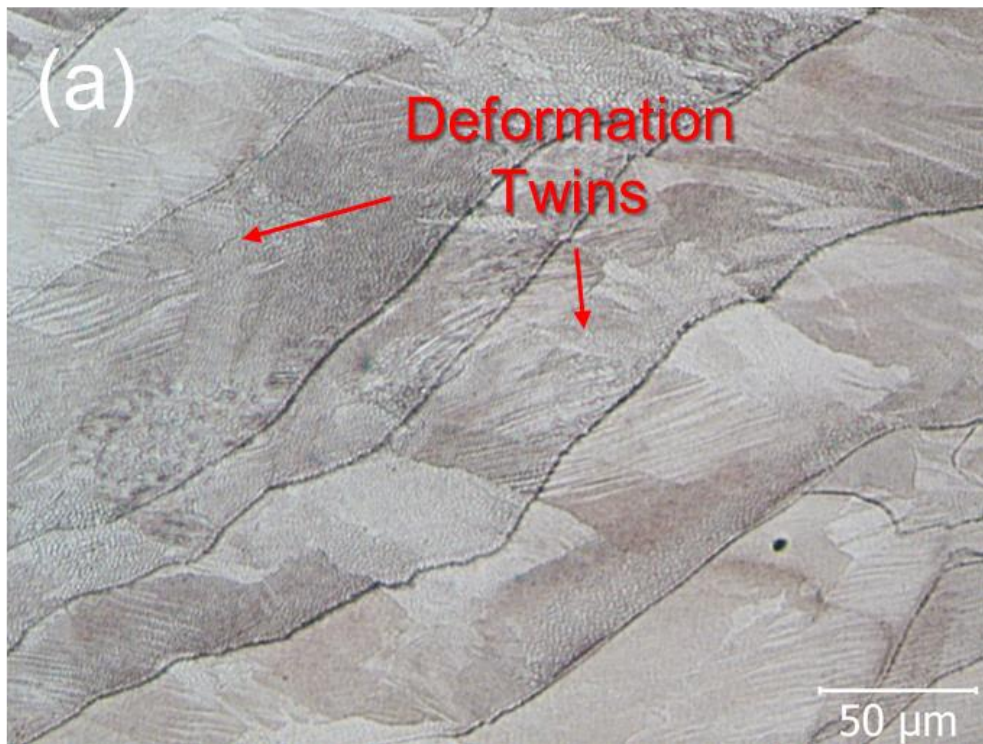


Figure 4.10. The optic picture of quasi-static tested (a) SLM-316L and (b) C-316L until 0.36 strain.

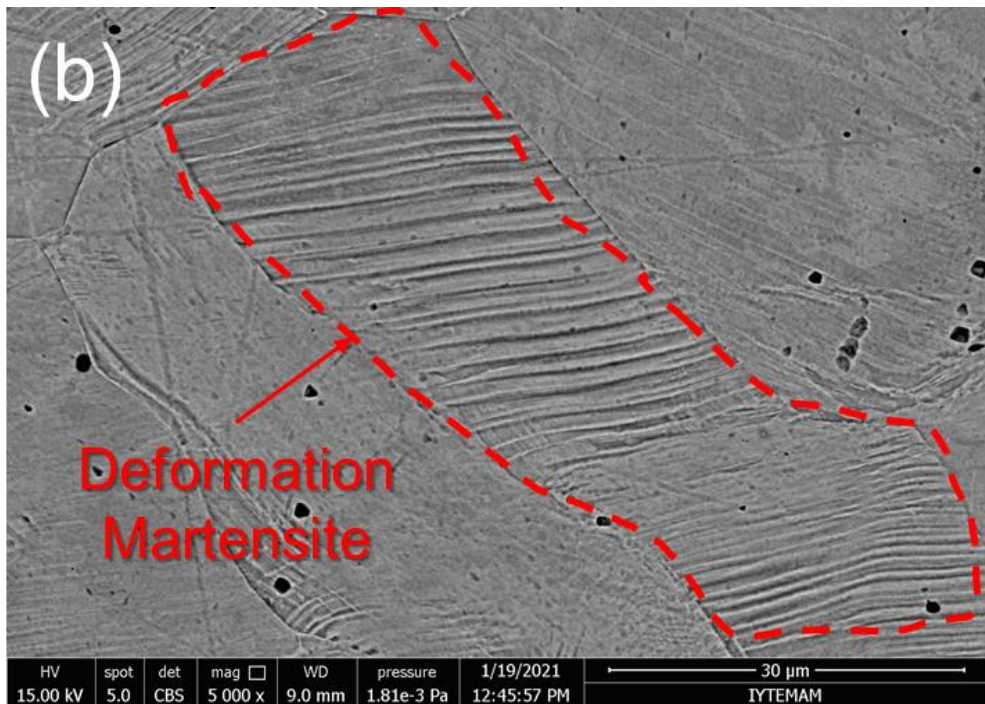
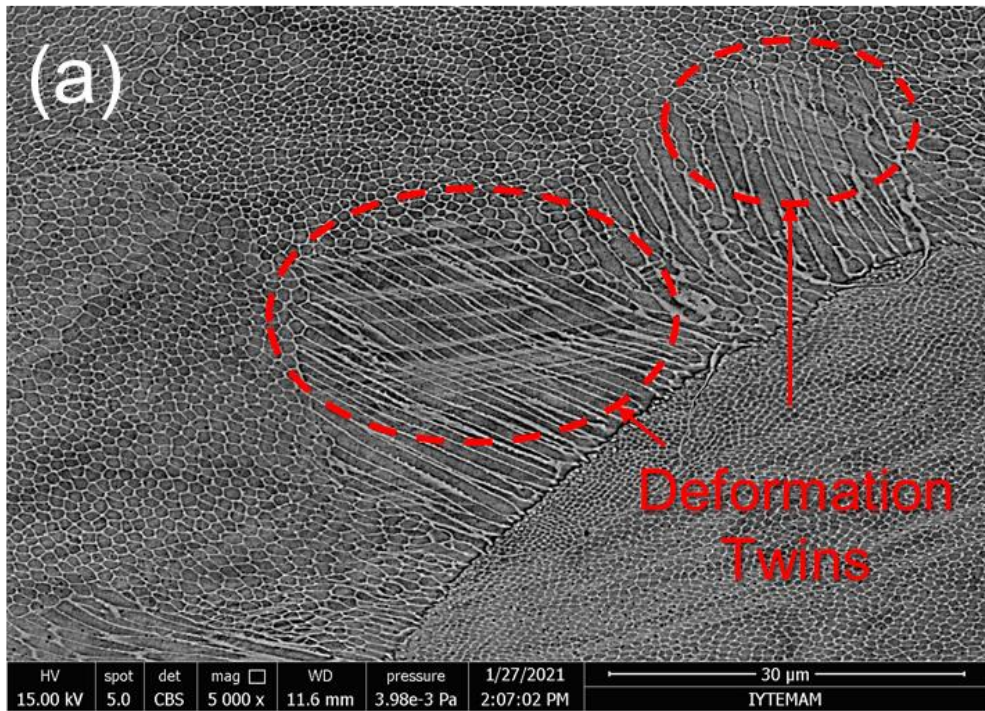


Figure 4.11. The SEM picture of quasi-static tested (a) SLM-316L and (b) C-316L until 0.36 strain.

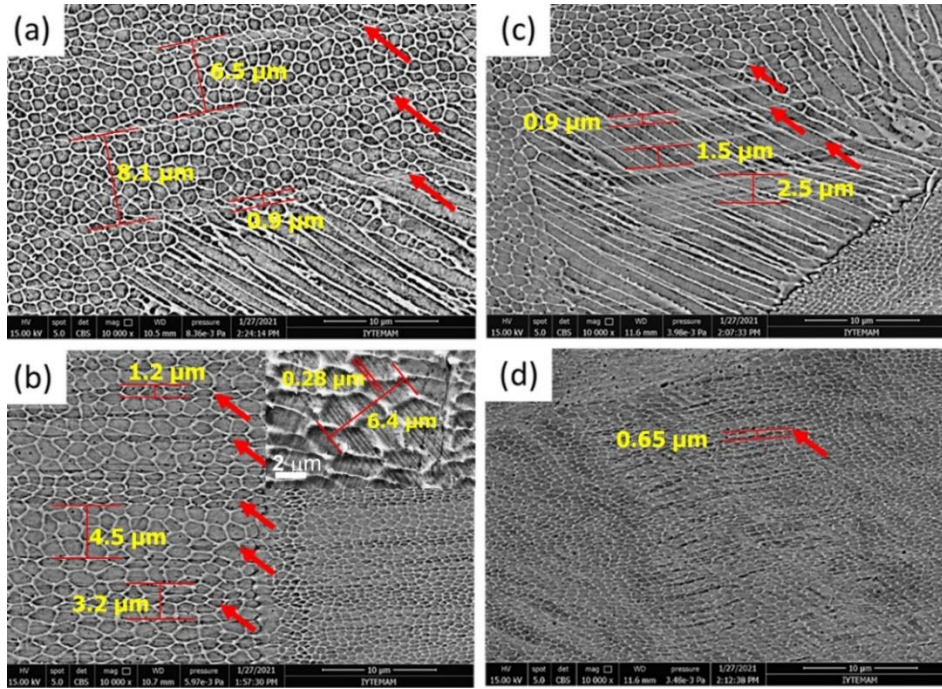


Figure 4.12. The SEM micrographs showing twinned regions in SLM-316L deformed until about (a) 0.11, (b) 0.22, (c) 0.36 and (d) 0.51 strains.

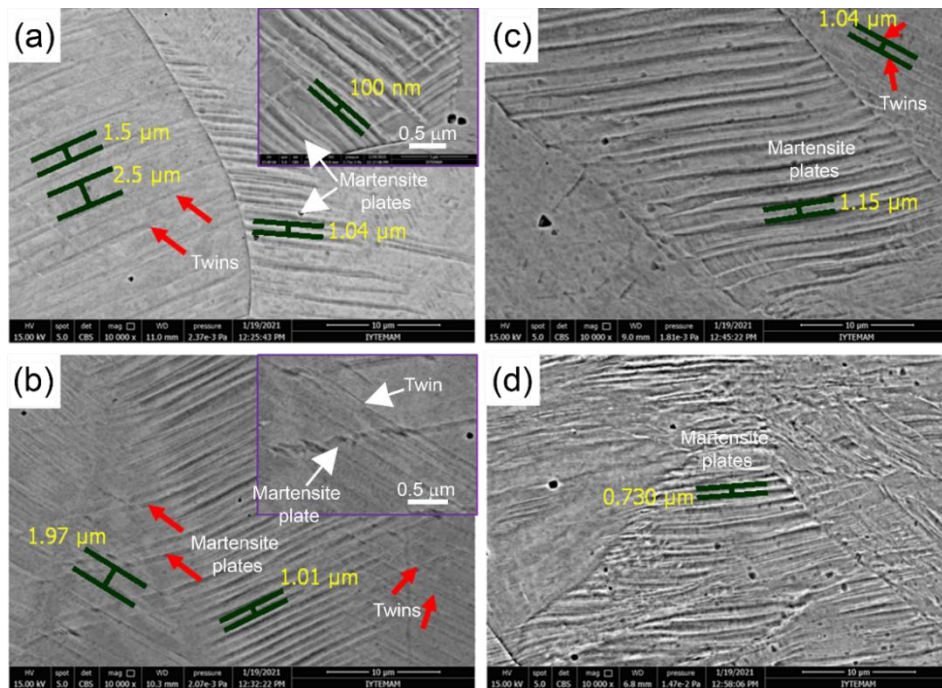


Figure 4.13. The SEM micrographs showing martensite plates (also lesser number of twins) in C-316L deformed until about (a) 0.11, (b) 0.22, (c) 0.36 and (d) 0.51 strain.

The quasi-statically tested SLM-316L specimens deform via twinning and slip similar to TWIP steels and C-316L martensitic transformation and slip similar to TRIP steels<sup>85</sup>. A similar observation was made in a recent study on the tensile behavior of an SLM-316L and C-316L alloy<sup>37</sup>. Increasing twin and martensite densities resulted in work hardening of SLM-316L and C-316L, respectively. The formation of mechanical twinning and martensite was proposed to depend on the applied stress and the SFE<sup>86</sup>. The typical range of SFEs for slip was reported as  $>45 \text{ mJ m}^{-2}$ , for twinning  $20\text{--}45 \text{ mJ m}^{-2}$  and/or phase transformation  $<20 \text{ mJ m}^{-2}$  for stainless steels<sup>87</sup>. The low values of SFE induce a large separation between the Shockley partials which prevents the cross-slip<sup>88</sup>. Therefore, the cross-slip is not considered as the rate controlling in the investigated alloys. A slight positive temperature dependency<sup>89</sup> or no temperature and strain rate dependency<sup>90</sup> were also reported for the twinning stress and the martensitic transformation is a diffusion-less process<sup>91</sup>. By considering also large grains sizes of both alloys, the deformation rate controlling step in both alloys is determined the dislocation emission from the twin and martensite boundaries<sup>92</sup>.

Quasi-static jumping test true stress-strain curves of SLM-316L and C-316L are shown in Figure 4.14. As seen in Figure 4.14, increasing strain rate within the quasi-static increases the flow stresses of both alloys. An increase of strain rate from  $1 \times 10^{-4}$  to  $1 \times 10^3 \text{ s}^{-1}$  increases the flow stress of SLM-316L by 20 MPa and C-316L by 15 MPa. The increase of the flow stress when the strain rate is jumped to  $1 \times 10^{-2} \text{ s}^{-1}$  is 30 and 20 MPa for SLM-316L and C-316L, respectively. These results show that both alloys have a rate sensitive flow stress behavior even at quasi-static strain rates.

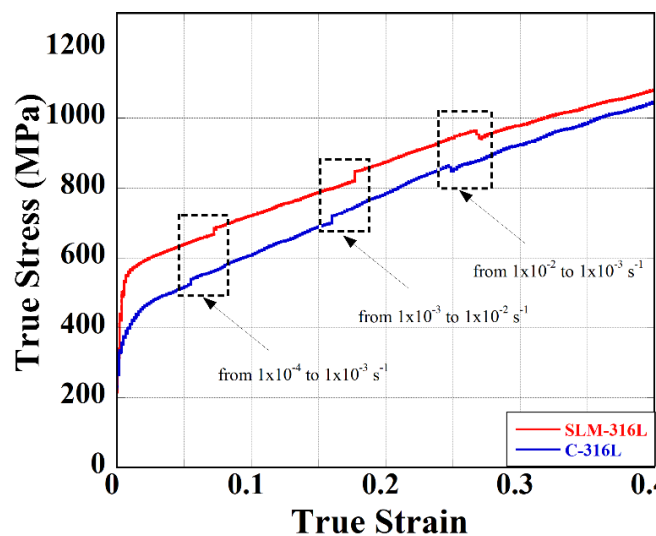


Figure 4.14. Quasi-static jumping true stress-strain curves of SLM-316L and C-316L.

The XRD spectra of quasi-statically tested C-316L and SLM-316L specimens until about different final strains are shown in Figure 4.15. As seen in Figure 4.15, both alloys show austenite peaks, while martensite  $\alpha'$  (110) peak intensity increases in C-316L alloy as the strain increases. The amount of martensite formation was determined by using an image program on the optical microscope pictures of the deformed specimens and using the Rietveld method from the XRD data. The measurements made using optical microscope pictures are shown in Figures 4.16(a-e), sequentially for the specimen deformed until 0, 0.11, 0.22, 0.36 and 0.51 strains. For each strain, measurements were repeated at least in three different regions. The blue lines seen in Figures 4.16(a-e) are martensite lathes and the areal density of these lathes were converted into mass fraction of martensite. In the calculations the areal densities of grain boundaries were subtracted from the areas of martensite. The results of martensite contents measured by the optical microscope pictures and XRD data are further tabulated together in Table 4.2. As tabulated in same table, the martensite percentage increases; 5.6, 12.1, 15.4 and 35.5% and 16, 18, 33 and 45.9% sequentially for the optical and XRD measurements. Both optical and XRD measurements show a similar trend of increasing martensite content with strain. The differences between the optical and XRD measurement are due to the difference in the measurement methods. In the optical pictures, the measurements are made in 2D, while XRD data measure the phase distribution in 3D.

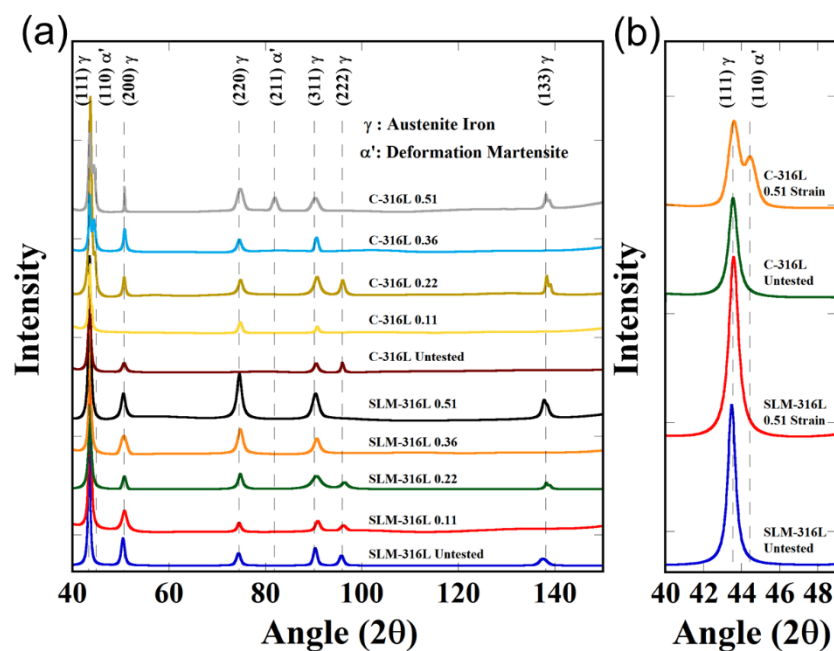
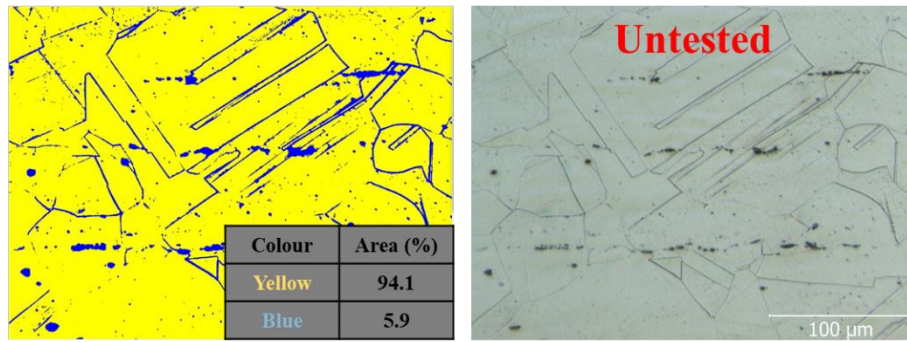
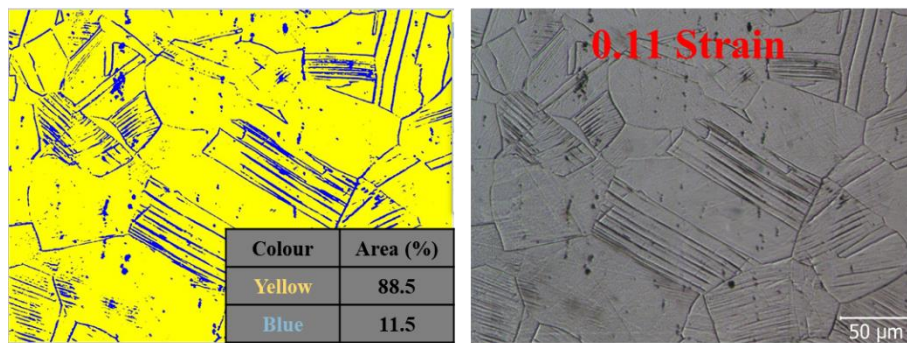


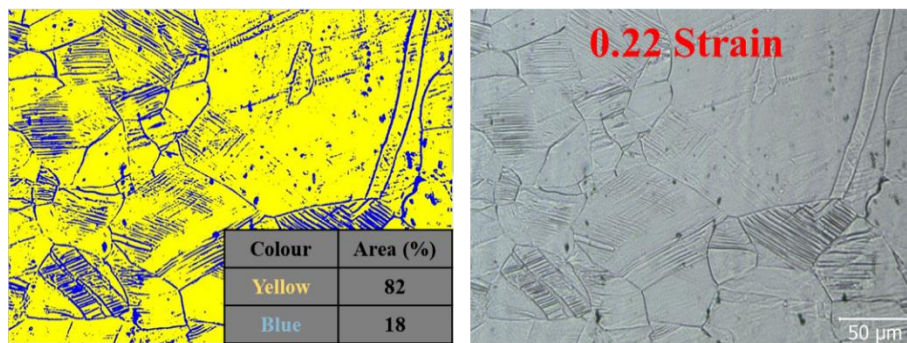
Figure 4.15. The XRD spectra of quasi-static tested SLM-316L and C-316L.



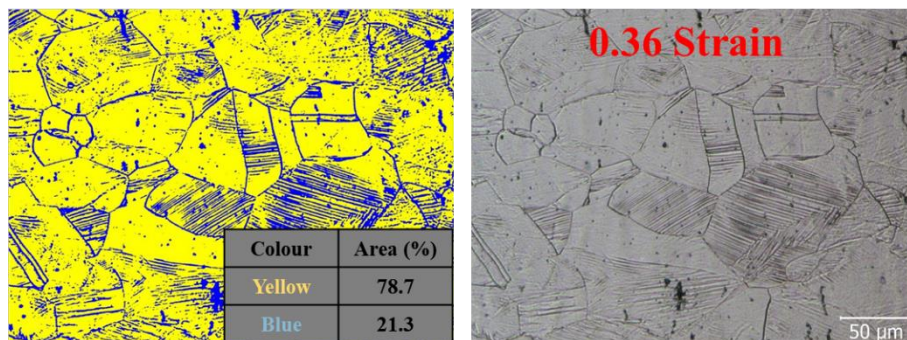
(a)



(b)



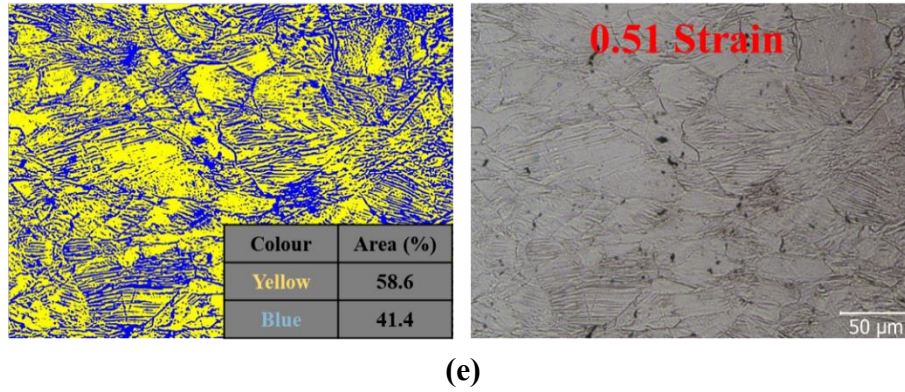
(c)



(d)

(cont. on next page)

Figure 4.16. Optically measured martensite volume at (a) 0, (b) 0.11, (c) 0.22, (d) 0.36 and (e) 0.51 true strain in quasi-static test.



(e)  
Figure 4.16. (cont.)

Table 4.2. The average martensite amount of quasi-static tested C-316L.

Martensite Amount	Optical Picture (area%)	XRD Result (wt%)
C 316L Untested	5.9 (Grain Boun.)	2.6
C-316L 0.11 Strain	5.6	16
C-316L 0.22 Strain	12.1	18
C-316L 0.36 Strain	15.4	33
C-316L 0.51 Strain	35.5	45.9

Figure 4.17 shows the variations of the hardness of the recovered SLM and C-316L specimens after the prescribed compression strain. The higher work hardening (WH) of C-316L is also reflected in the same figure in which the hardness of C-316L increase over those of SLM-316L after about 0.5 strains. To account for the effect of twinning and martensite on the strength, hardness tests were performed in the regions of heavy twins and no twins in SLM-316L and heavy martensite and no martensite region in C-316L after about 0.11 strain. A higher hardness increase in the martensite transformation is seen in Figure 4.18, while the increase in hardness in twinning is moderate. Twin planes act as an obstacle to the dislocation motion and have an influence on the flow stresses similar to the grain size, Hall-Petch relation<sup>86</sup>. As the deformation twins are continuously formed with increasing strain, the distance between twin planes decreases; hence, the distance taken by the dislocations and this results in an increase in the flow stress. The higher WH of C-316L than SLM-316L is probably due to the higher resistance of the martensite plate than the twin boundary to the dislocation motion. Both the presence of twin and martensite plates induce a more nonhomogeneous indentation as compared with the regions of no twin and no martensite, as seen in Figures 4.19(a-d).

The regions with twins and martensite (Figures 4.19(a) and (c)) also show lesser numbers of slip lines as compared with the regions with no twin and no martensite (Figures 4.19(a) and (b)).

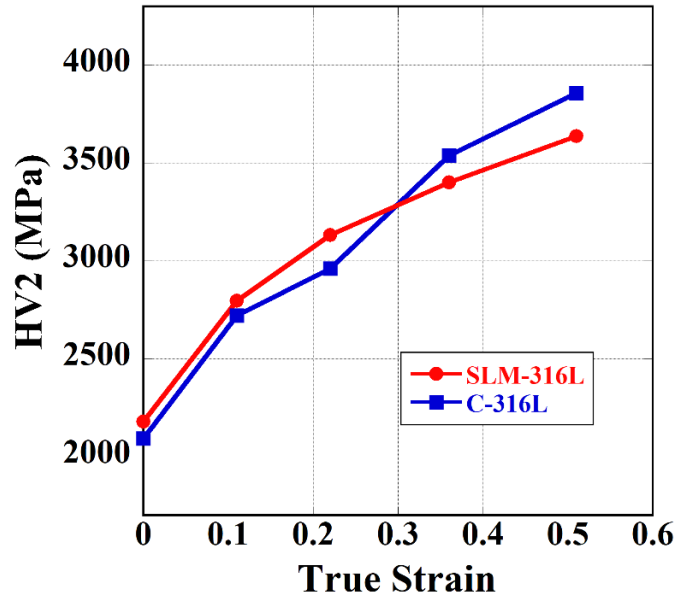


Figure 4.17. The hardness values (HV2) at 0.11, 0.22, 0.36 and 0.51 strain values for quasi-static tests.

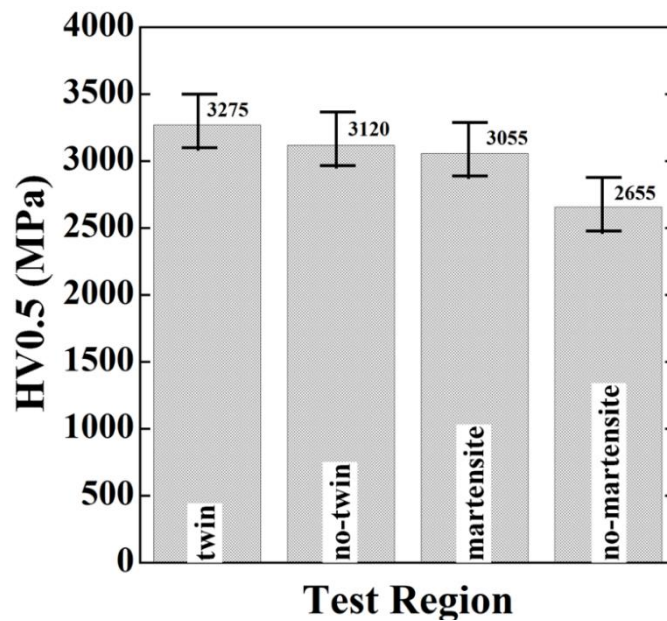


Figure 4.18. Hardness value (HV0.5) of tested SLM-316L and C-316L specimens applied to twin, no-twin, martensite and no-martensite region, respectively.

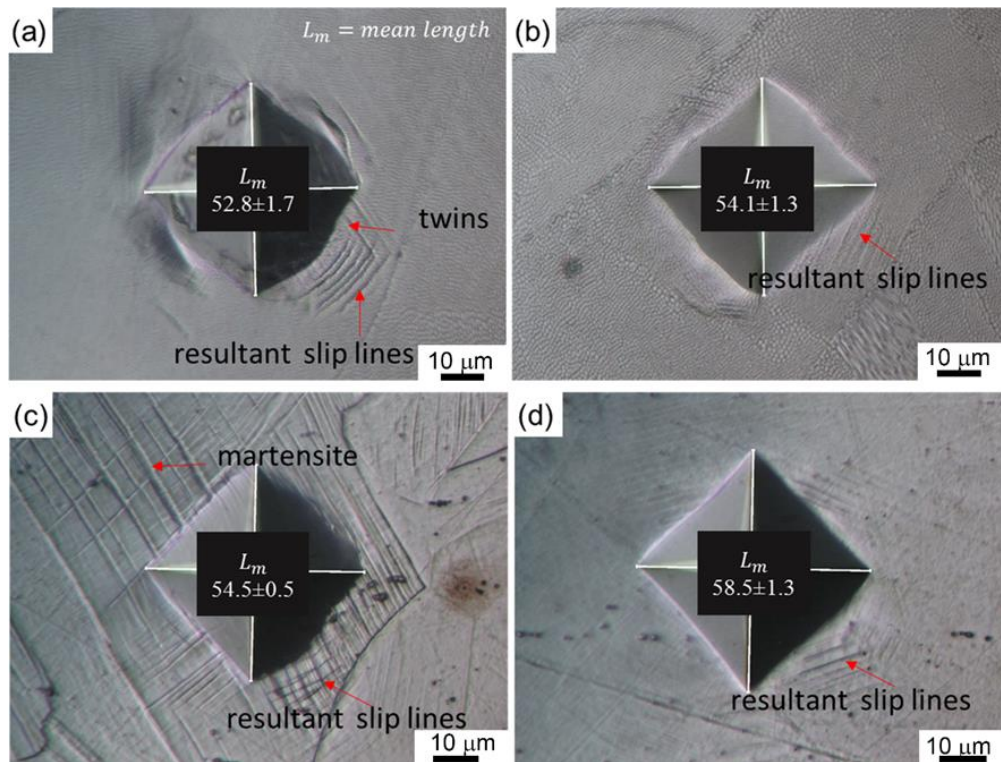
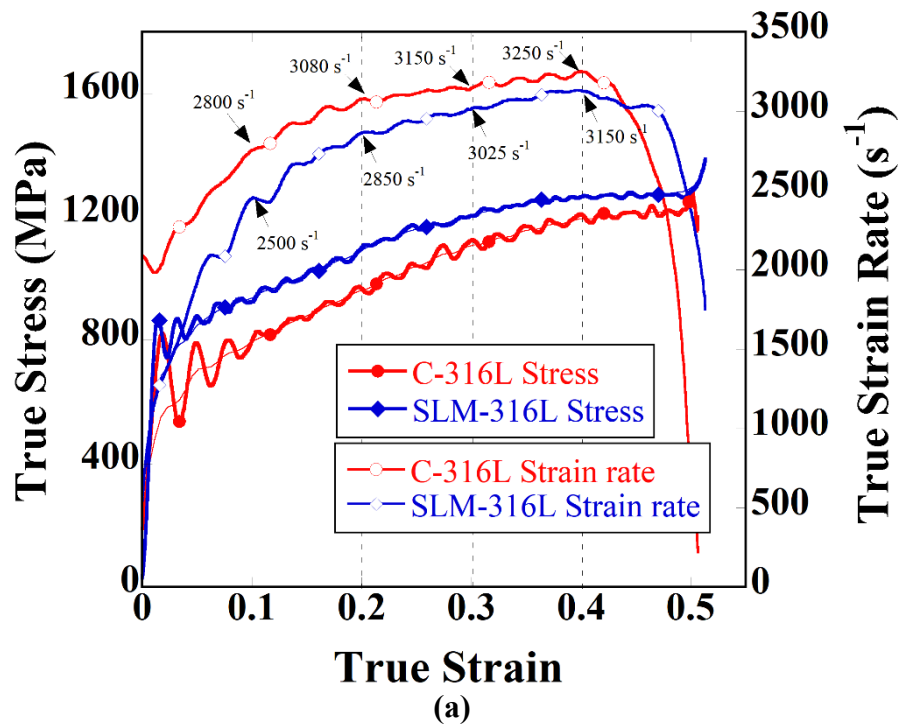


Figure 4.19. The optical pictures of hardness tests of tested SLM-316L and C-316L specimens applied to (a) twin, (b) no-twin, (c) martensite and (d) no-martensite region, respectively.

### 4.3. SHPB Tests and the Effect of Strain Rate

Figure 4.20(a) shows the representative compression true stress-true strain curves and true strain rate-true strain curves of both alloys. Since SHPB tests were performed at the same gas gun pressure; hence, under the same incident stress, softer C-316L exhibited higher strain rates than SLM-316L as seen in Figure 4.20(a). The strain rate is not constant in the SHPB tests, varying between 2500 and 3150  $s^{-1}$  for SLM-316L and between 2800 and 3250  $s^{-1}$  for C-316L, between 0.11 and 0.51 true strain (Figure 4.20(a)). As with the quasi-static tests, dynamically tested SLM-316L specimens have a higher yield point ( $795 \pm 35$  MPa) than dynamically tested C-316L ( $624 \pm 26$  MPa). Figure 4.20(b) shows the true-stress-true strain curves of SLM-316L at quasi-static and dynamic strain rates (three tests at each strain rate). In the high strain rate tests (2500-3150  $s^{-1}$ ), the sudden increase of stress is due to a higher mechanical impedance of the ring deformation after a

prescribed strain, as marked in Figure 4.20(b). Figure 4.20(c) shows the true-stress-true strain curves of C-316L at quasi-static and dynamic strain rates. Note that SHPB tests give unreliable strains at the beginning of the deformation, partly due to the geometrical artifacts induced by the specimen-bar contacts and partly due to the non-equilibrium stress condition at these initial strains<sup>93, 94</sup>. Nevertheless, it is clearly seen in Figures 4.20(b) and (c), both alloys show a strain rate sensitive flow stress behavior: as the strain rate increases from quasi-static to high strain rates, the flow stress increases. Moreover, both SLM-316L and C-316L specimens also did not show fracture until about 0.51 strain as with the quasi-statically tested specimens. Figures 2.1 (a) and (b) show SLM-316L and C-316L dynamically tested specimens for each strain value and untested specimens, respectively. A higher lateral deformation through z-direction than y-direction in the tested SLM-316L specimens is clearly seen in Figure 4.21(a), proving the anisotropy between building direction and perpendicular to building direction. But, the tested C-316L specimens show homogeneous lateral deformations as seen in Figure 4.21(b), which proves the isotropic mechanical properties.



(cont. on next page)

Figure 4.20. (a) compression true stress and true strain curves in the SHPB tests, (b) true stress-true strain curves of (b) SLM-316L and (c) C-316L at quasi-static and dynamic strains rates.

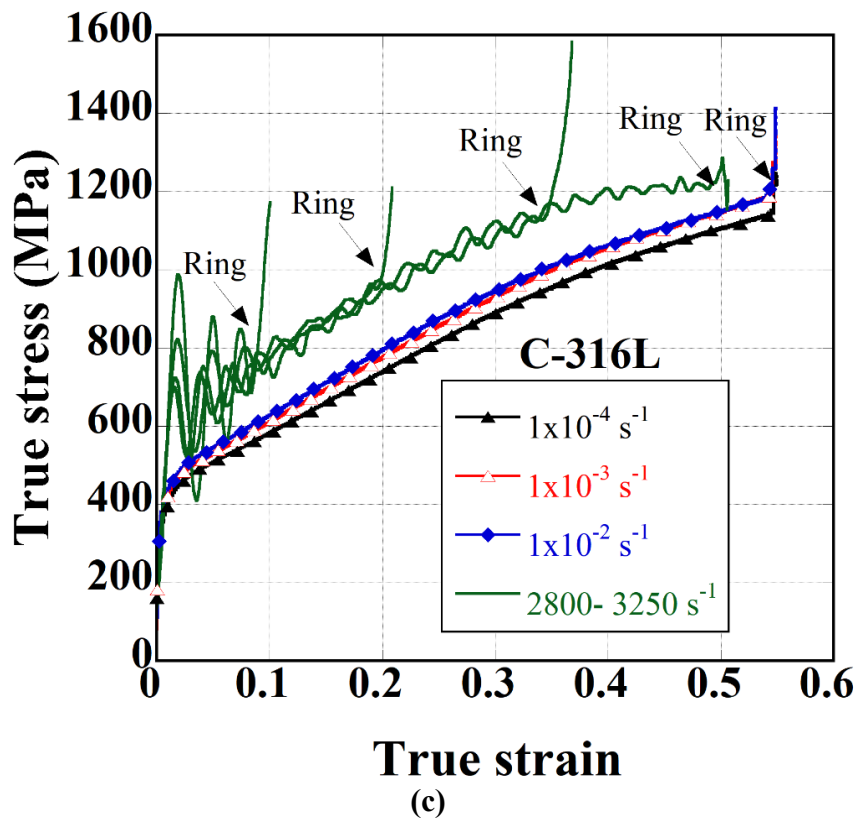
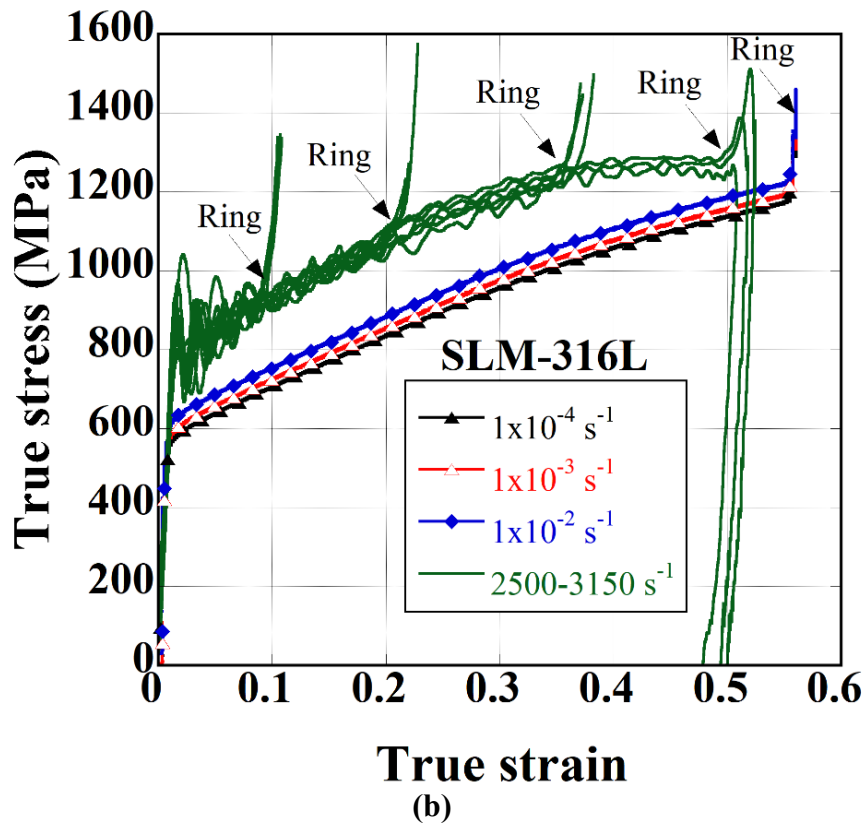


Figure 4.20. (cont.)

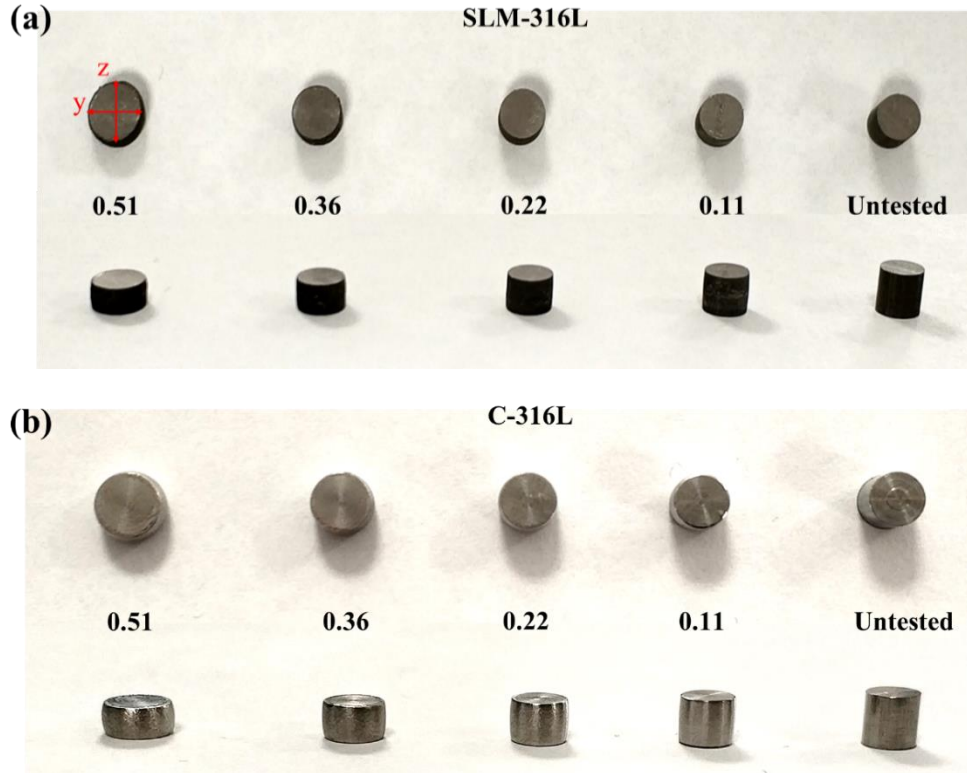


Figure 4.21. The pictures of untested and dynamically tested specimens (a) SLM-316L and (b) C-316L.

The work hardening behavior of both alloys at quasi-static and high strain rates are shown in Figure 4.22. The quasi-static WH of C-316L is seen in the same figure higher than that of SLM-316L. The quasi-work hardening of both alloys maybe considered in three distinct deformation regions. These regions corresponded to (I) a rapidly reduced WH region at about 0.1 strain (II) a more slowly reduced WH region between 0.1 and 0.3 strain at and (III) again a rapidly reduced WH region at the strains above 0.3. Although, the dynamic work hardening of C-316L is higher than the quasi-static work hardening at low strains, both become equal to each other between 0.14 and 0.23 strain. After 0.23 strain, the dynamic work hardening decreases rapidly below the quasi-static hardening. The dynamic hardening of SLM-316L alloy is higher than the quasi-static hardening until about 0.23 strain as seen in Figure 4.22. The dynamic hardening of SLM-316L alloy reaches the quasi-static dynamic hardening of C-316L at about 0.18 strain. The rapid reduction of the dynamic work hardening of both alloys as compared with the quasi-static work hardening after about 0.20-0.23 strain may be due to the adiabatic heating of the dynamically tested specimens, which reduces the resistance to the deformation. It is also noted dynamic loading increases the extent of region I, while decreases the extent of

region II. Previously it was shown that, for the quasi-static loading of the same alloys, the region I was slip dominated, region II was twinning and/or martensite transformation-induced slip deformation dominated, and region III was again slip dominated which also reported in ref. <sup>95</sup>. The twinning-dominated deformation of SLM-316L and the martensite transformation-dominated deformation of C-316L was shown to start at 0.07 strain and continue until about  $\sim 0.3$  strain.

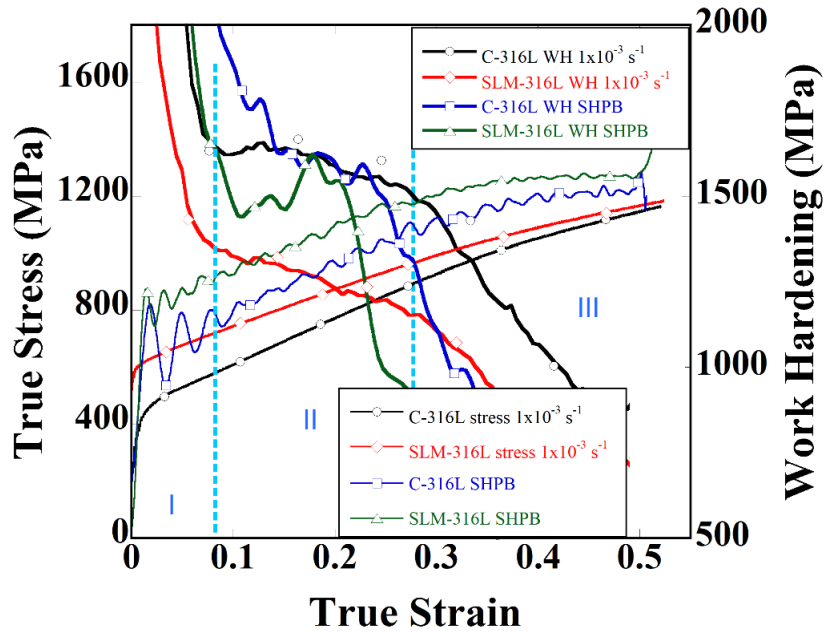


Figure 4.22. Representative work hardening-true strain curves of SLM-316L and C-316L with quasi-static and high strain rate true stress-true strain curves and three distinct regions.

The SEM and optical microscope of the deformation microstructure images of SLM-316L and C-316L alloys at 0.36 strain value are shown in Figures 4.23(a) and (b), and Figures 4.24(a) and (b), respectively. As seen in Figure 4.23(b) and Figure 4.24(b) deformation martensite and twins are seen together in SHPB tested C-316L as opposite to only deformation martensite is seen in quasi-statically tested specimens. The SHPB tested SLM-316L specimens show deformation twins solely as with quasi-statically tested specimens. Twin and martensite deformations are not always intertwined, they are also found in different grains. Morphologically, it is very difficult to distinguish between twins and martensite. The twin deformations are more widely spaced but thinner, while the martensite deformations are observed more frequently but as thicker platelets. Also, generally, martensite continues through the grain, while twins end at grain boundaries.

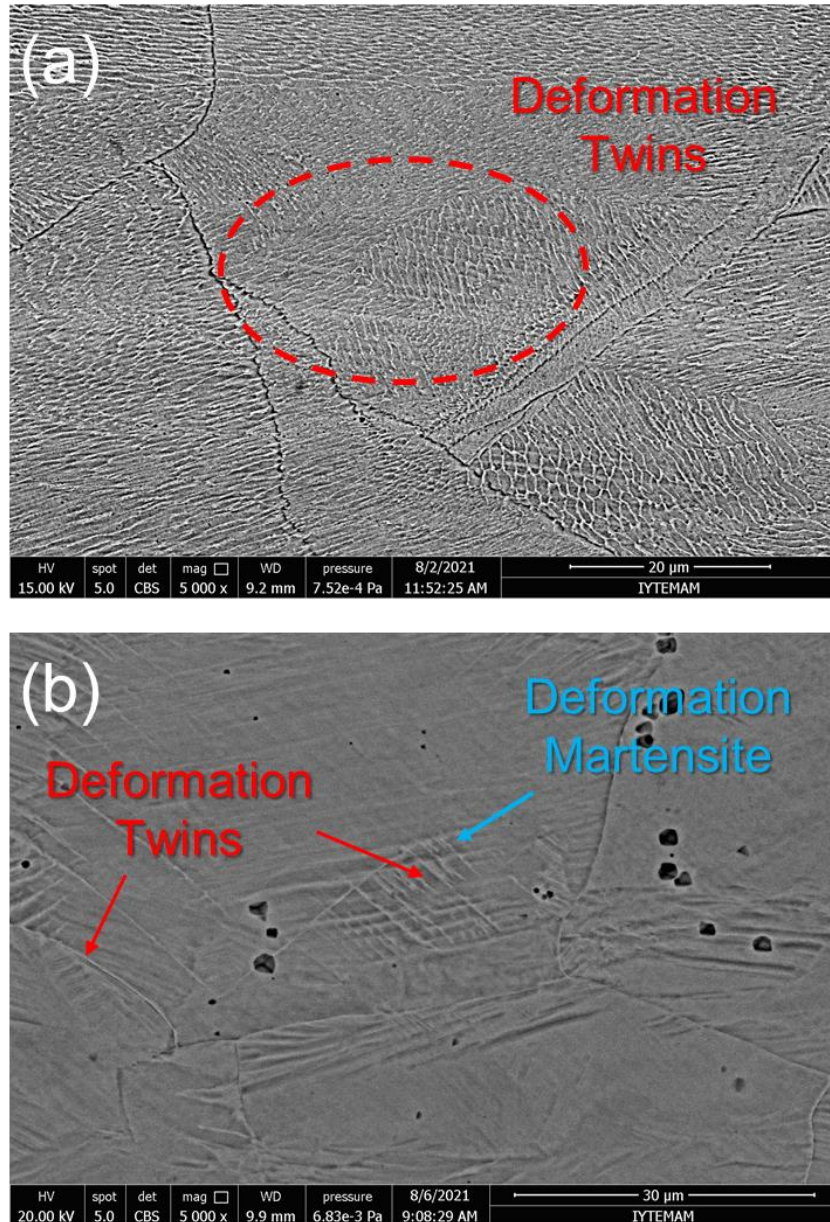


Figure 4.23. The SEM picture of SHPB tested (a) SLM-316L and (b) C-316L until 0.36 strain.

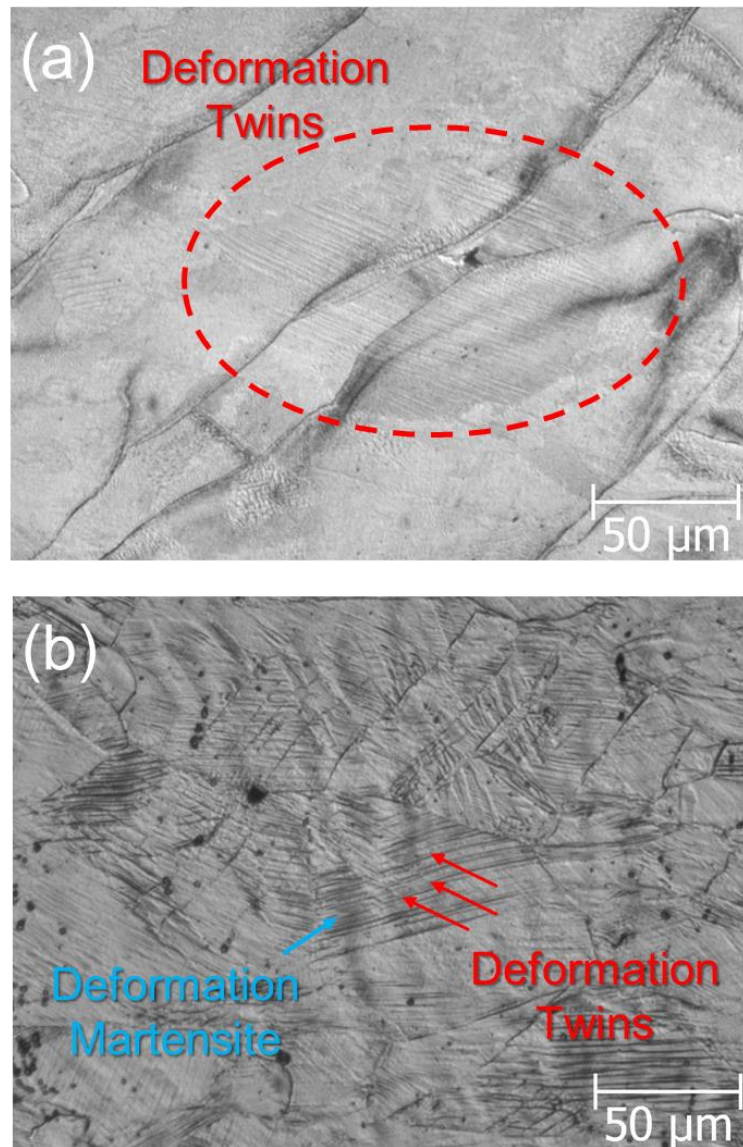


Figure 4.24. The optic picture of SHPB tested (a) SLM-316L and (b) C-316L until 0.36 strain.

At a large scale, visible twins are actually seen as a combination of multiple nano twins as with the quasi-statically tested specimens. The amount of martensite in SHPB tested C-316L specimens decreases observably compared to the quasi-static test, but there is no morphological difference in the formed martensite platelets. On the other hand, it is observed that the twin deformation in SHPB tested SLM-316L specimens are shorter and more frequent than the quasi-static tested specimens.

The XRD spectra of SHPB tested C-316L and SLM 316L specimens are shown in Figure 4.25(a). It is seen in the same figure, the relative peak intensity of martensite deformation in the SHPB test decreases compared to that of the static test (Figure

4.25(b)). The XRD spectra of SHPB tested C-316L becomes very much similar to that of SLM-316L in terms of peak profile as seen in Figure 4.25(a). This further proves the twin deformation in the SHPB tested C-316L specimens. The XRD peaks of SHPB tested SLM-316L increase as the strain increases, similar to quasi-static tested one. More, the previously invisible (220) peak of the austenitic phase become visible in SHPB tested C-316L specimens.

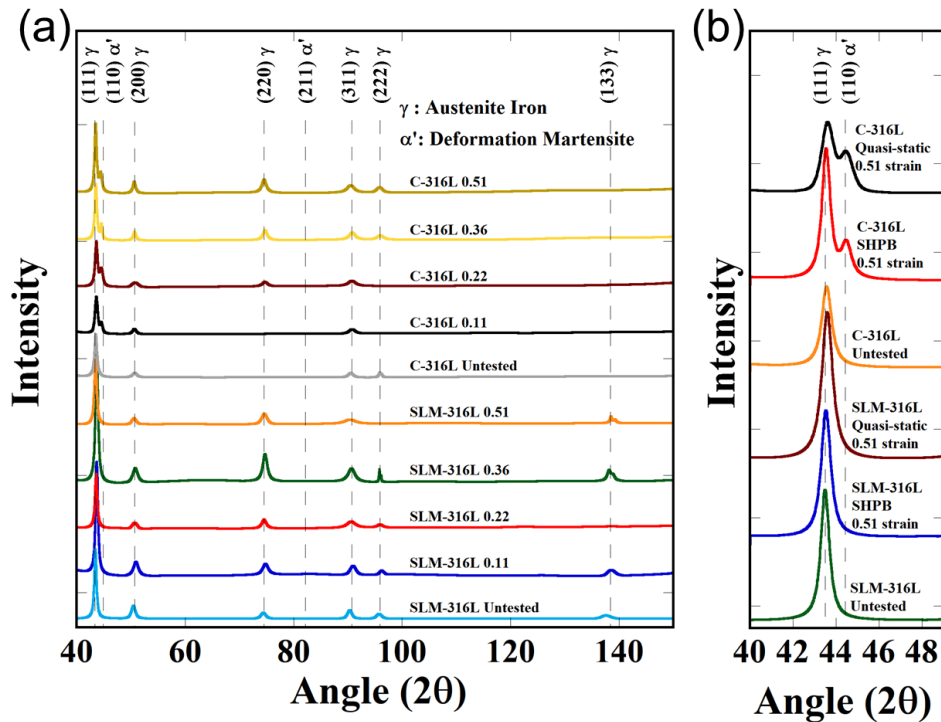


Figure 4.25. The XRD spectra (a) of SHPB tested SLM-316L and C-316L and (b) comparison with quasi-static tested specimens.

The pictures of the optical measurement of SHPB martensite formation at 0.11, 0.22, 0.36 and 0.51 true strain are shown in Figures 4.26(a-d), respectively. The martensite content measured optically and by XRD are further tabulated in Table 4.3. again, the martensite content measured by XRD is higher than that measured optically. At 0.11, 0.22, 0.36 and 0.51 strain, the martensite contents are 4.3, 5.3, 7.2 and 14.6% in optical measurement and 21.4, 27, 25 and 23.5% in the XRD measurement, respectively. Despite the slight increase in the martensite content with increasing strain in the optical measurements, almost a constant amount of martensite formation is seen in the XRD measurements. The amount of twin deformation could not be calculated with the XRD

phase analysis measurement because the twinning is actually a crystal disorientation, not a phase change<sup>95, 96</sup>.

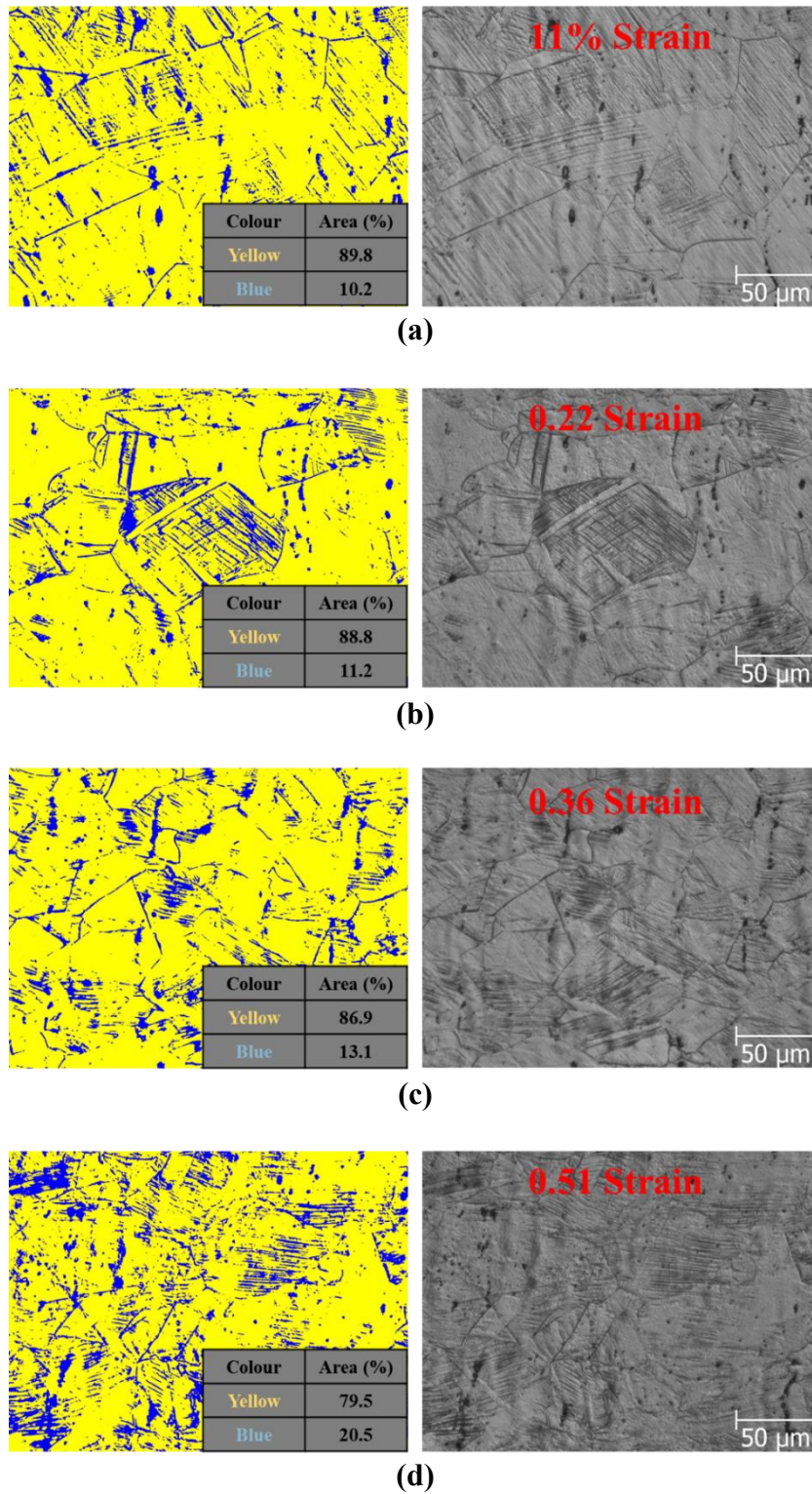


Figure 4.26. Optically measured martensite volume at (a) 0.11, (b) 0.22, (c) 0.36 and (d) 0.51 true strain value for SHPB tests.

Table 4.3. The average martensite amount of SHPB tested C-316L.

<b>Martensite Volume</b>	<b>Optical Picture (area%)</b>	<b>XRD Result (wt%)</b>
C 316L Untested	(Grain 5.9%)	2.6
C-316L 0.11 Strain	4.3	21.4
C-316L 0.22 Strain	5.3	27
C-316L 0.36 Strain	7.2	25
C-316L 0.51 Strain	14.6	23.5

The average hardness of SHPB and quasi-statically tested SLM-316L and C-316L specimens are shown together in Figure 4.27 as function of final deformation strain. After about 0.2 strain, the hardness of quasi-statically tested specimens become higher those of SHPB tested specimens. The hardness value of quasi-static and SHPB tested SLM-316L and C-316L specimens at 0.51 strain value are tabulated in Table 4.4. As tabulated in Table 4.4, for both SLM-316L and C-316L specimens, the hardnesses of static tested specimens are higher those SHPB tested ones. As seen in Figure 4.27 and tabulated in Table 4.4, C-316L specimens have slightly higher hardness values than SLM-316L when the strain value reaches 0.51 in both SHPB and quasi-static tests. This indicates that the work hardening rate of C-316L alloy is higher than SLM-316L for both SHPB and quasi-static tests. SHPB tested C-316L specimens reach higher compressive strength than quasi-static tested C-316L as shown in Figure 4.20(c). Nevertheless, quasi-static tested C-316L reach a higher hardness value while strain value increases compared to SHPB tested C-316L.

As shown in Figure 4.28, the amount of martensite decreases after the strain value of 0.22 in SHPB tested C-316L. Three types of deformations were observed in SHPB tested C-316L: slip, twins and martensite as shown in Figure 4.23(a) and Figure 4.24(a) due to high SFE as a result of adiabatic heating<sup>68, 74, 97</sup>. Due to the higher SFE, the measured amount of martensite could be decreases and deformation behavior shifted from martensite to twin deformation. Also, twins partially encourage the slip motion as it exhibits a nucleation-like behavior<sup>37</sup>. This phenomenon can be explained as above. In the SHPB tested SLM-316L specimens, the higher SFE energy due to adiabatic heating could be reduces the twins formed. Deformation behavior was partially shifted from TWIP to slip deformation. In the C-316L alloys, the variation from the deformation behavior is clearly seen in Figure 4.28 at the strain value between 0.18-0.35. This strain range corresponds to Stage II as seen in Figure 4.18.

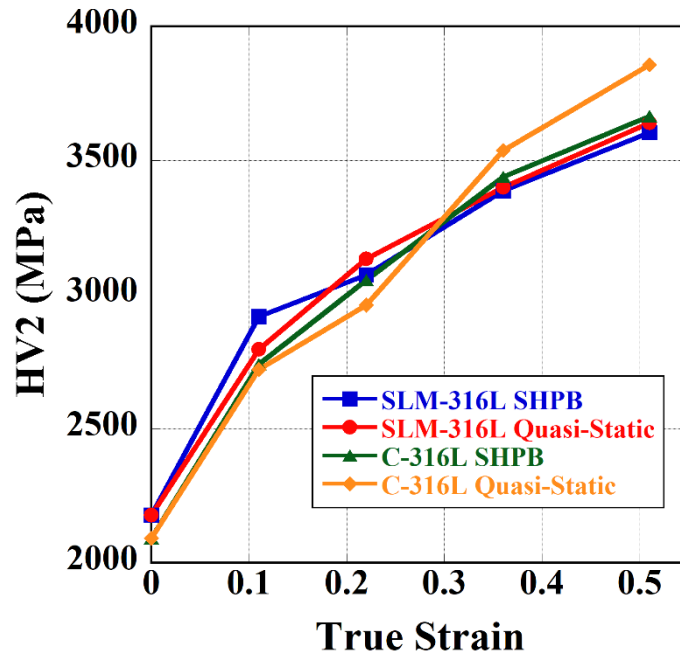


Figure 4.27. The hardness values (HV2) of SHPB and quasi-static tested SLM-316L and C-316L.

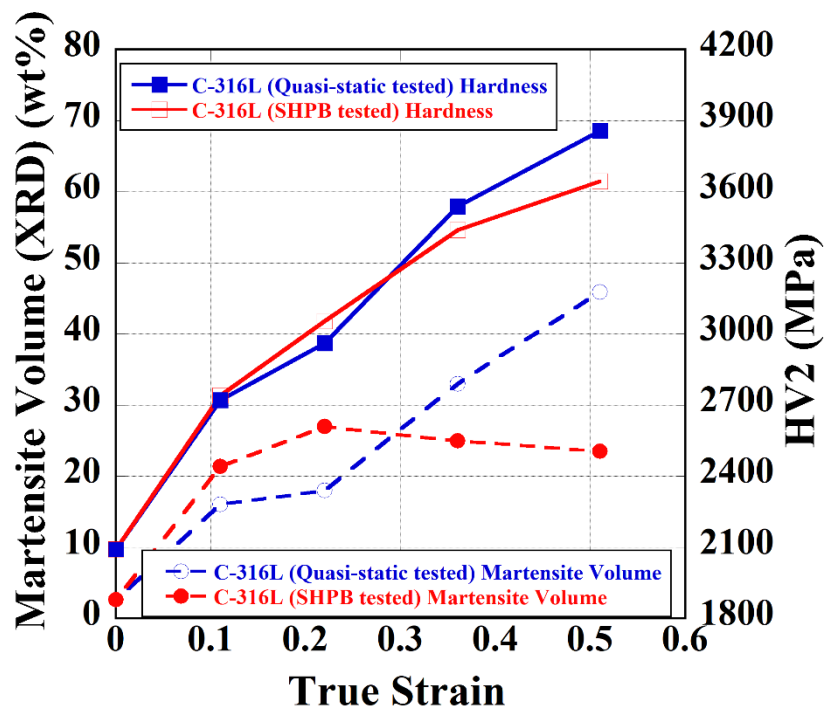


Figure 4.28. The martensite volume and hardness values of SHPB and quasi-static tested C-316L specimens.

Table 4.4. The hardness of SHPB and quasi-static tested C-316L and SLM-316L at 0.51

Specimen	Quasi-static tested (HV2/MPa)	SHPB tested (HV2/MPa)
C-316L 0.51 Strain	3860±260	3660±150
SLM-316L 0.51 Strain	3640±210	3605±170

#### 4.4. Constitutive relations and strain rate sensitivity

The flow stresses of both alloys were fitted with the Johnson and Cook (JC) flow stress equation <sup>98</sup> as

$$\sigma = (A + B\varepsilon^n)[1 + c \ln\left(\frac{\dot{\varepsilon}}{\dot{\varepsilon}_0}\right)] \left(1 - \left[\frac{T - T_r}{T_m - T_r}\right]^m\right) \quad (4.2)$$

where,  $\sigma$  and  $\varepsilon$  are the equivalent true stress and true plastic strain, respectively.  $A$ ,  $B$ ,  $n$ ,  $c$  and  $m$  are the JC parameters;  $n$  is the strain hardening,  $c$  strain rate sensitivity,  $T$  is the deformation temperature,  $T_r$  is the deformation temperature (room) at the reference strain rate,  $T_m$  is the melting temperature,  $m$  is softening parameter, and  $\dot{\varepsilon}$  and  $\dot{\varepsilon}_0$  are sequentially the strain rate and reference strain rate ( $1 \times 10^{-3} \text{ s}^{-1}$ ). Eqn. 4.2 is modified by replacing  $(A + B\varepsilon^n)$  with the stress-strain curve ( $\sigma_o(\varepsilon)$ ). The values of  $\sigma_o(\varepsilon)$  were determined by interpolating the experimental true stresses with true strain at  $1 \times 10^{-3} \text{ s}^{-1}$ . To calculate the strain rate sensitivity parameter  $c$ , the true flow stresses at 0.1, 0.2, 0.3 and 0.4 strain are drawn against the logarithm of true strain rate and then the true flow stresses are fitted with Eqn. 4.2 as shown in Figures 4.29(a) and (b), sequentially for SLM-316L and C-316L. The  $c$  values of SLM-316L decreases from 0.18 to 0.011 when the true strain increases from 0.1 to 0.4, as seen in Figure 4.29(a). A similar reduction of the  $c$  values is also seen in C-316L within the same strain range from 0.0185 to 0.009 (Figure 4.29(b)). Different from SLM-316L, the  $c$  value of C-316L decreases from 0.0185 and 0.0155 at 0.1 and 0.2 strain to a value of 0.013 when the flow stress is fitted between  $1 \times 10^{-4} \text{ s}^{-1}$  and  $1 \times 10^{-2} \text{ s}^{-1}$  as tabulated in the table in Figure 4.29(b). The relatively lower values of  $c$  at increasing strains are partly due to increased adiabatic heating at increasing strains at high strain rates. The values of  $c$  for commercially produced 316L listed in ref. <sup>99</sup> between 0.042 and 0.1 are higher than the values determined in present study. The rate

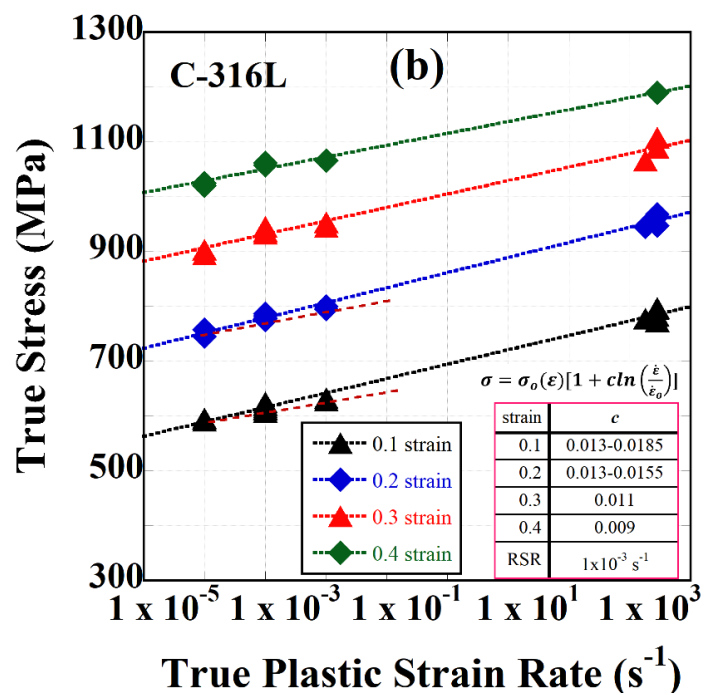
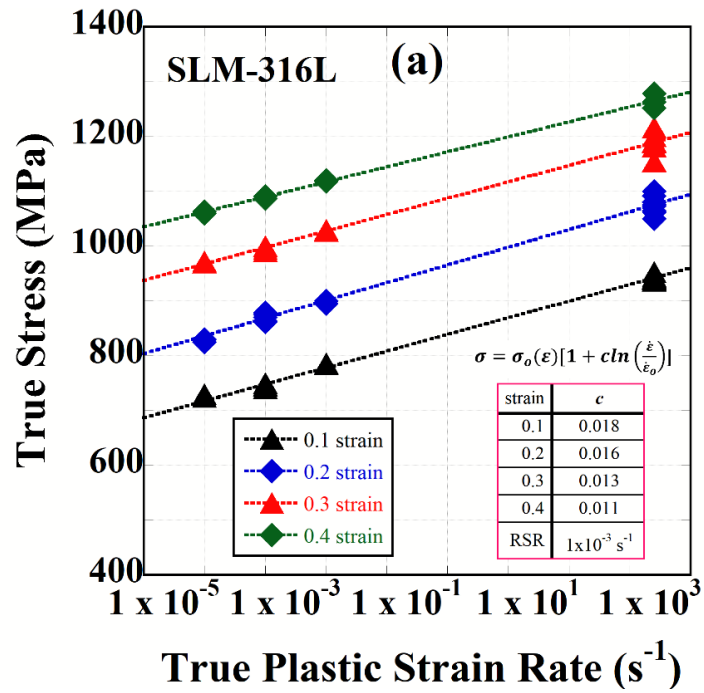
sensitivity parameters of SLM-316L and C-316L as tabulated in Figures 4.29(a) and (b) are very similar to each other at low strains, 0.1 and 0.2, while at increasing strains the rate sensitivity of SLM-316L becomes slightly higher than that of C-316L. In the quasi-static strain rate regime, however, the rate sensitivity of SLM-316L (0.018) is higher than that of C-316L (0.013) at low strains, 0.1 and 0.2. For comparison, the data in Figures 4.29(a) and (b) were also fitted by the following relation <sup>90</sup>,

$$\sigma = K \dot{\varepsilon}^{m'} \quad (4.3)$$

where  $K$  is a constant and  $m'$  is the strain rate sensitivity parameter and is

$$m' = \left. \frac{d \ln(\sigma)}{d \ln(\dot{\varepsilon})} \right|_{T, \varepsilon} \quad (4.4)$$

The fitted results of the flow stress to Eqn. 4.3 are shown in Figure 4.29(c) for SLM-316L and C-316L, respectively. The  $m'$  values tabulated in the same figure are determined sequentially with the quasi-static strain rate regime ( $1 \times 10^{-4}$ - $1 \times 10^{-2}$  s<sup>-1</sup>) and within the quasi-static and high strain rate regime ( $1 \times 10^{-4}$ - up to 3150 and 3250 s<sup>-1</sup>). The  $m'$  values of SLM-316L and C-316L as seen in Figure 4.29(c) are very similar; for SLM-316L ranging 0.0166-0.051 at 0.1 strain and 0.0177-0.0147 at 0.2 strain and for C-316L ranging 0.0131-0.0164 at 0.1 strain and 0.0129-0.0139 at 0.2 strain. Again, SLM-316 shows a higher  $m'$  value in the quasi-static strain rate regime. Eqn. 4.3 was previously fitted with the experimental tensile stress data of an SLM-316L and the value of  $m'$  was reported 0.0248 based on the yield strength between  $10^{-5}$  and  $10^{-1}$  s<sup>-1</sup> <sup>14</sup>. Comparably a lower  $m'$  value has been recently reported for an laser LAM deposited 316L within the similar strain rate regime, 0.0102 <sup>100</sup>. In the same study, the rate sensitivity parameter of a commercial rolled 316L was determined 0.0065, which is in contradict with the  $c$  values of commercial 316L listed in ref. <sup>99</sup> and  $m'$  values determined in the present study. The differences in  $m'$  values between the present and above studies are most likely due to the difference in the strain rate regime studied, in the developed microstructure and applied testing methods (compression and tension). More, the adiabatic heating of the specimens in the present study may lead to a lower strain rate sensitivity parameter.



(cont. on next page)

Figure 4.29. The true stress vs.  $\ln$  true plastic strain rate at different strains and the variation of  $c$  value with strain and strain rate (a) SLM-316L and (b) C-316L and (c)  $\ln$  true stress vs.  $\ln$  true plastic strain rate and  $m$  values at different strains for SLM-316L and C-316L.

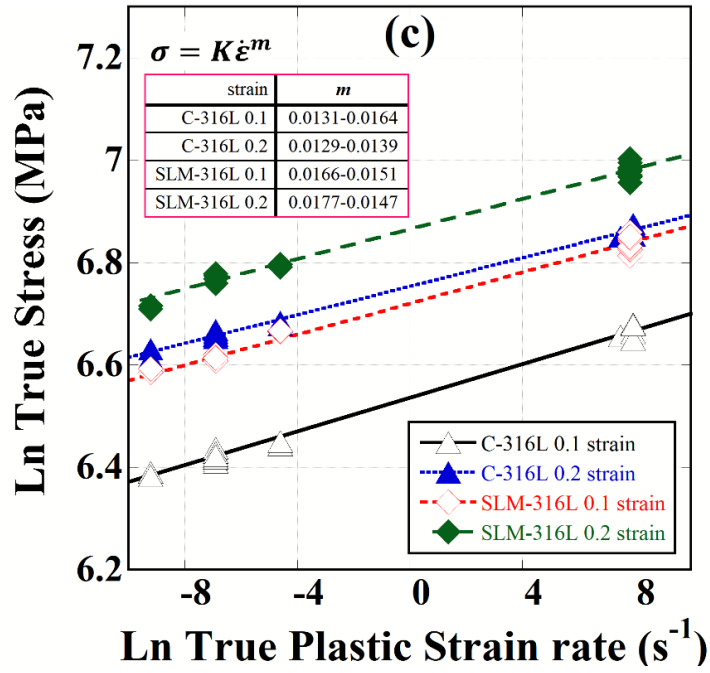


Figure 4.29. (cont.)

The  $c$  parameters of SLM-316L and C-316L were fitted with true strain into a polynomial equation, as shown in Figure 4.30(a). As noted in the same figure, the  $c$  parameters of both alloys are almost the same at 0.1 strain, while at increasing strains a more rapid decline is seen in the  $c$  parameter of C-316L. The  $m$  parameters of both alloys were determined by fitting the quasi-static compression yield strengths (taken from the literature) with the flowing relation:  $\sigma = \sigma_r \left(1 - \left[\frac{T-T_r}{T_m-T_r}\right]^m\right)$ , where  $\sigma_r$  is the room temperature yield strength. As is seen Figure 4.30(b), taking the  $m$  value equal to 1 for both alloys, results in a good match with the strength-temperature curve.

The predicted JC and experimental true stress-true strain curves at quasi-static strain rates ( $1 \times 10^{-4}$  and  $1 \times 10^{-2}$  s<sup>-1</sup>) and SHPB are shown in Figures 4.31(a) and (b) for SLM-316L and C-316L, respectively. Using determined  $c$  values, adiabatic stress-strain curves were predicted by taking  $m=1$ , while isothermal curves were calculated using the following and  $T=T_r$

$$\sigma = \frac{(A+B\epsilon^n) \left[1 + c \ln\left(\frac{\dot{\epsilon}}{\dot{\epsilon}_0}\right)\right]}{\left(1 - \left[\frac{T-T_r}{T_m-T_r}\right]^m\right)}$$

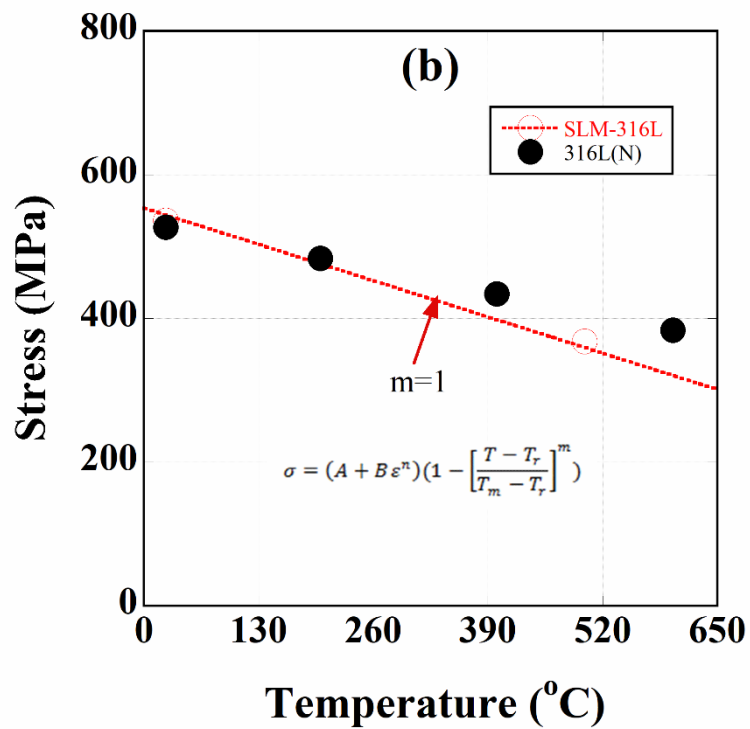
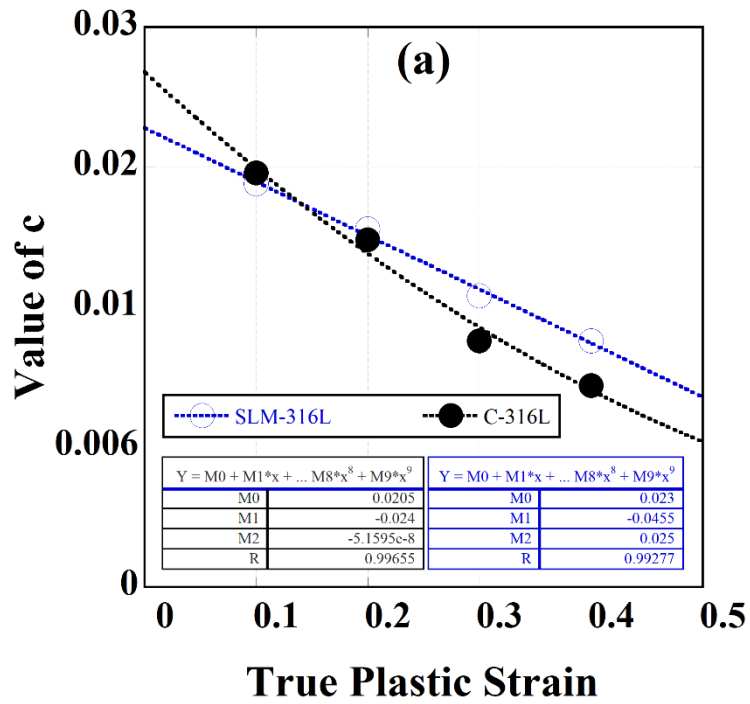


Figure 4.30. The fitted value of (a)  $c$  with strain and (b) compression stress vs. temperature and fitted curve when  $m=1$ , for SLM-316L ( $\circ^{101}$ ) and C-316L ( $\bullet^{73}$ ).

In the same curves in Figures 4.31(a) and (b), the temperature rise ( $\Delta T$ ) was calculated using the following relation,

$$\Delta T = \frac{\beta \int \sigma d\varepsilon}{\rho c_p} \quad (4.5)$$

where  $\beta$  and  $c_p$  are the Taylor–Quinney coefficient<sup>102</sup> (fraction of deformation work converted into heat) and the heat capacity, respectively. The value of  $c_p$  was taken 500 J kg<sup>-1</sup> K<sup>-1</sup><sup>103</sup> and  $T_m$  1425 °C. The value of  $\beta$  is usually taken 0.9. The value of  $\beta$  for a cold rolled 316L specimen was however reported to increase with increasing strain and was below 0.9<sup>104</sup>. The measured  $\beta$  values of some metals and alloys have shown that the value dependent on the types of the material and test<sup>105</sup>. For example, the value was found higher in compression (0.7-0.9) and shear than in tension for a CP-Ti. It was claimed that the formation of twin boundaries stored less significant deformation energy and therefore the value of  $\beta$  was higher in the compression tested specimen which exhibited larger fractions of twinning deformation. As will be explained later, the tested SLM-316L deforms under compression by the TWIP and C-316L by the Transformation-Induced-Plasticity (TRIP). Therefore, the values of  $\beta$  was taken 0.8 as an average for both alloys. The calculated isothermal and adiabatic curves in Figures 4.31(a) and (b) indicate that adiabatic heating becomes nearly effective after about 0.1 strain. The predicted and experimental SHPB true stress-true strain curves show well agreements with each other until about the point A in the same graphs. After the point A which corresponds to an adiabatic temperature of 110 °C, experimental stress-strain curves show a reduced work hardening. The reduced work hardening of experimental stress-strain curves after the point A is attributed to a decrease in the  $m$  value after about 100 °C which is also reported for 316L and 316LN alloys in ref.<sup>65</sup>.

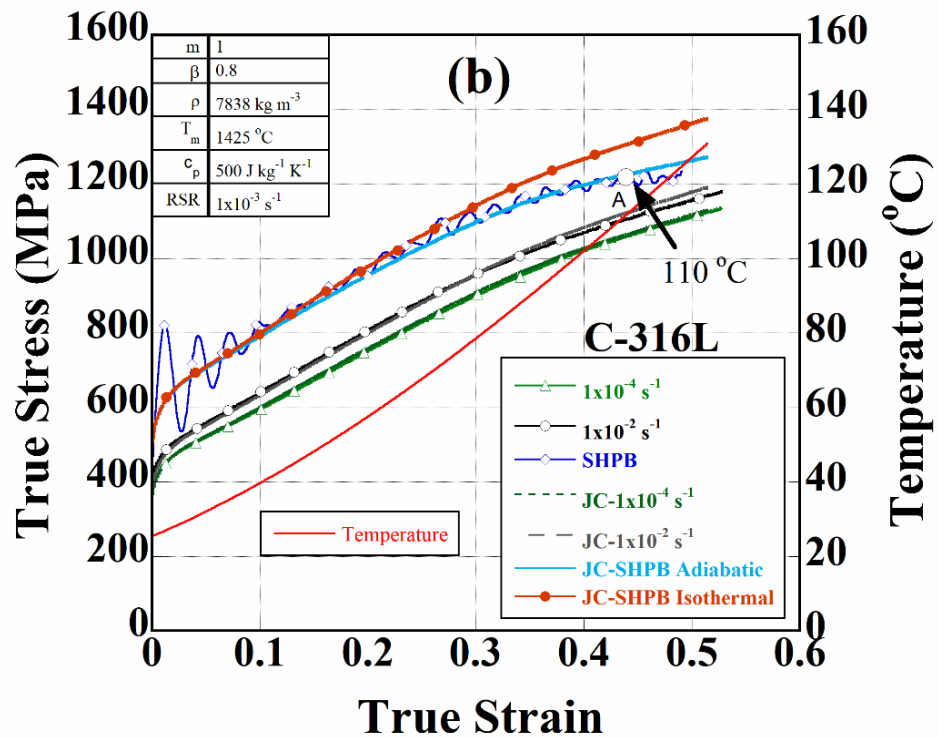
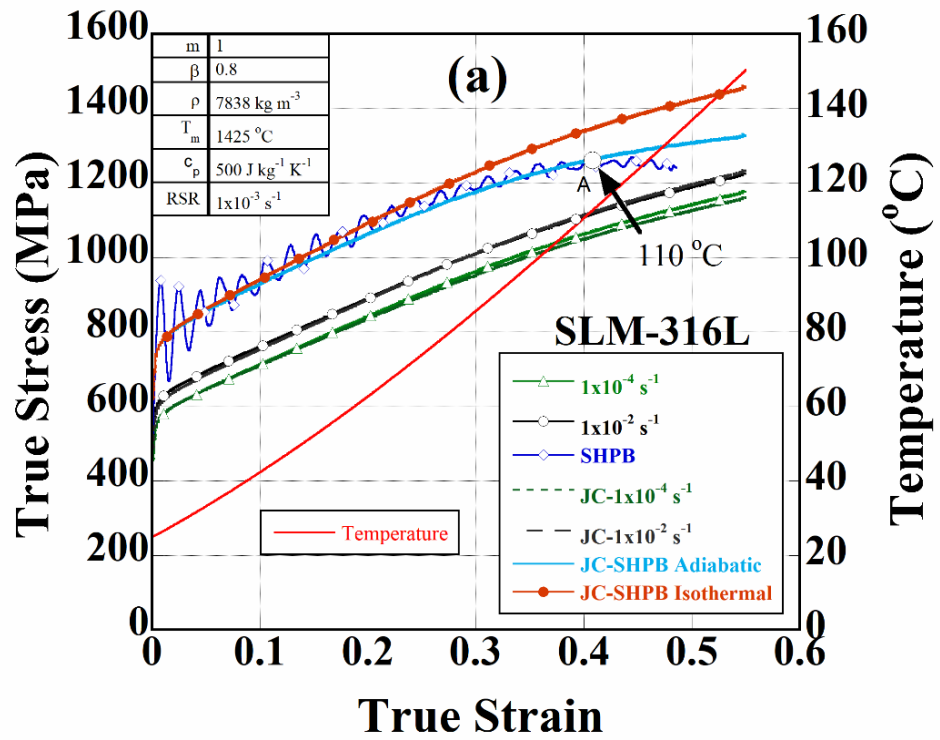


Figure 4.31. Experimental and predicted JC true stress-true strain curves with temperature rise (a) SLM-316L and (b) C-316L.

## 4.5. Effect of Strain Rate

The tested SLM-fabricated 316L specimens deform via twinning and slip similar to TWIP steels<sup>85</sup>. The formation of mechanical twinning proposed to depend on the applied stress and the stacking fault energy (SFE)<sup>86</sup>. The twinning occurs when the applied shear stress is greater than a critical stress for twinning on a highly stressed plane as similar with slip<sup>106</sup>. The typical range of SFEs for slip was reported as >45 mJ/m<sup>2</sup>, for twinning 20–45 mJ/m<sup>2</sup> and/or phase transformation <20 mJ/m<sup>2</sup> for stainless steels<sup>87</sup>. The low values of SFE induces a large separation between the Shockley partials which prevents the cross-slip. The stacking faults were proposed to serve for the nucleation twinning<sup>107</sup>. Twin planes act as an obstacle to the dislocation motion and has an influence on the flow stresses similar to the grain size, Hall-Petch relation<sup>58</sup>. As the deformation twins are continuously formed with increasing strain, the distance between twin planes decreases; hence the distance taken by the dislocations and this results in increase in the flow stress. A slight positive temperature dependency<sup>89</sup> or no temperature and strain rate dependency<sup>90</sup> were reported for the twinning stress. Simply, deformation twinning was presumed not a thermally activated process opposite to the slip by dislocation motion. The thermally activated deformation<sup>88</sup> stress ( $\sigma$ ) is given by the following relation<sup>108, 109</sup>

$$\sigma = \frac{M(\Delta G_o - kT \ln \dot{\epsilon}_o)}{V^*} + \frac{MkT}{V^*} \ln \dot{\epsilon} = \sigma_i + k_1 \ln \dot{\epsilon} \quad (4.6)$$

In Eqn. 4.6,  $\Delta G_o$  is the activation free energy,  $M$  is the Taylor's factor,  $k$  is the Boltzmann's constant,  $V$  is the activation volume and  $k_1$  is the slope of  $\sigma - \ln \dot{\epsilon}$  curve,  $k_1 = \left(\frac{\partial \sigma}{\partial \ln \dot{\epsilon}}\right)_{T, \epsilon} = \frac{MkT}{V^*}$ . The strain rate sensitivity in the thermal activation-controlled deformation region will be inversely proportional to the activation volume. The calculated activation volumes of tested SLM-316L and C-316L are tabulated in Table 1 at different strains and strain rate regimes (between 1x10<sup>-4</sup> and 1x10<sup>-2</sup> s<sup>-1</sup> and between 1x10<sup>-4</sup> and 2500-2800 s<sup>-1</sup>). In the quasi-static strain rate range, the activation volumes of SLM-316L are lower than those of C-316L and the activation volumes decrease as the strain increases from 0.11 to 0.22 strain. In the quasi-static-high strain rate regime, the activation volumes of both alloys become very much similar. The activation volume of SLM-316L between two strain rate regimes are similar, while the activation volume of C-316L is slightly reduced

in the quasi-static-high strain rate regime. The similar strain rate sensitivity of C-316L indicates a similar thermally activated deformation process (slip by dislocation) involvement in both alloys.

Table 4.5. Activation volume of SLM-316L and C-316L at different strain rate range.

Specimen/strain	Strain rate range	$MkT/V^*$ (MPa/s)	$V^*$ (nm <sup>3</sup> )	$V^*b^3$
C-316L 0.1	$1 \times 10^{-4}$ - $1 \times 10^{-2}$ s <sup>-1</sup>	8.03	1.49	89.8
C-316L 0.2	$1 \times 10^{-4}$ - $1 \times 10^{-2}$ s <sup>-1</sup>	9.98	1.20	72.2
SLM-316L 0.2	$1 \times 10^{-4}$ - $1 \times 10^{-2}$ s <sup>-1</sup>	12.59	0.95	57.3
SLM-316L 0.2	$1 \times 10^{-4}$ - $1 \times 10^{-2}$ s <sup>-1</sup>	15.20	0.79	47.4
C-316L 0.1	$1 \times 10^{-4}$ -2800 s <sup>-1</sup>	11.42	1.05	63.1
C-316L 0.2	$1 \times 10^{-4}$ -2800 s <sup>-1</sup>	11.97	0.10	60.2
SLM-316L 0.1	$1 \times 10^{-4}$ -2500 s <sup>-1</sup>	12.62	0.95	57.1
SLM-316L 0.2	$1 \times 10^{-4}$ -2500 s <sup>-1</sup>	14.15	0.84	50.9

#### 4.6. Unloading-Reloading Compression Tests

Strain rate and strain rate history effects dependencies of commercial and additive manufactured alloys were subjected to a kind of unload-reload process to be examined. Unlike strain rate sensitivity, strain rate sensitive alloys can show the effects of the previous test rate when tested at different strain rates. This situation is called strain rate history dependency<sup>68, 110</sup>. On the other hand, strain rate-independent materials show reload deformation behavior independent of the rate of the previous test<sup>110</sup>. SLM-316L and C-316L specimens, which were previously quasi-static tested and comes to strain values of 0.11, 0.22, 0.36, 0.51, respectively, were SHPB reloaded as shown in Figures 4.25(a-b). For SLM-316L specimens, all specimens tested at up to 0.51 strain had a lower yield strength at baseline compared to the reference SHPB tested specimen. It was observed that as the strain value increased, the reloaded specimens reach the reference plastic curve as shown in Figure 4.25(a). For C-316L specimens, all tested specimens had nearly the same yield strength when compared to the reference SHPB tested specimens as shown in Figure 4.25(b). After ~0.36 strain value, a decrease in stress and softening is observed in the reference SHPB test curves. This is due to adiabatic heating, as mentioned earlier.

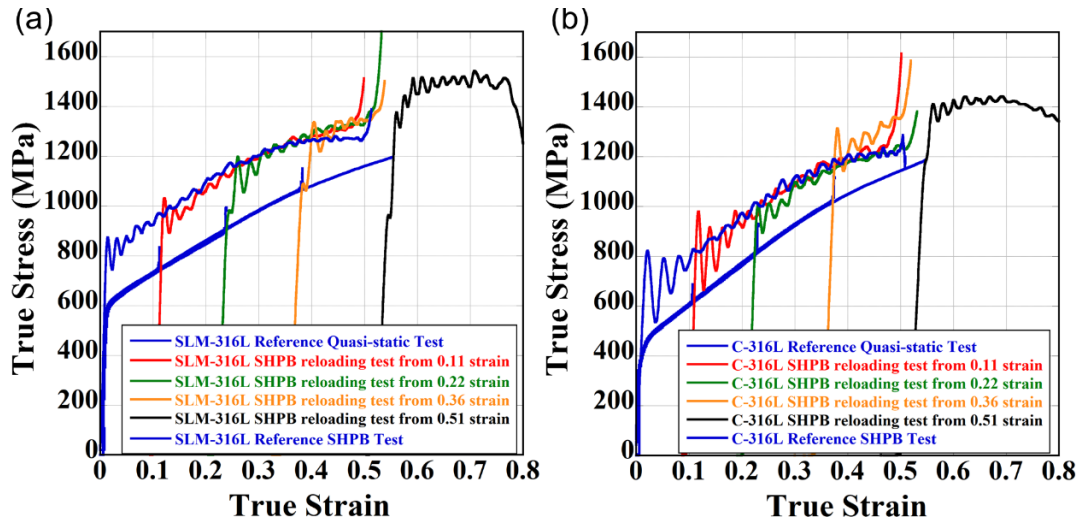


Figure 4.32. SHPB reloading tests of previously quasi-static tested (a) SLM-316L and (b) C-316L specimens.

The quasi-static reloading stress-strain curves of the dynamically tested SLM-316L and C-316L specimens are shown in Figures 4.26(a-b). In contrast to dynamically reloaded quasi-statically tested specimens, quasi-statically statically reloaded samples show higher stress values than the reference quasi-static curve as shown in Figure 4.26(a). As is seen in Figure 4.16(a), the quasi-statically reloaded specimen clearly shows strain rate history dependent flow stresses. While quasi-statically reloaded C-316L specimens exhibit no strain rate history effect, depicted in Figure 4.26(b). The reasons for this behavior will be further investigated in a future study.

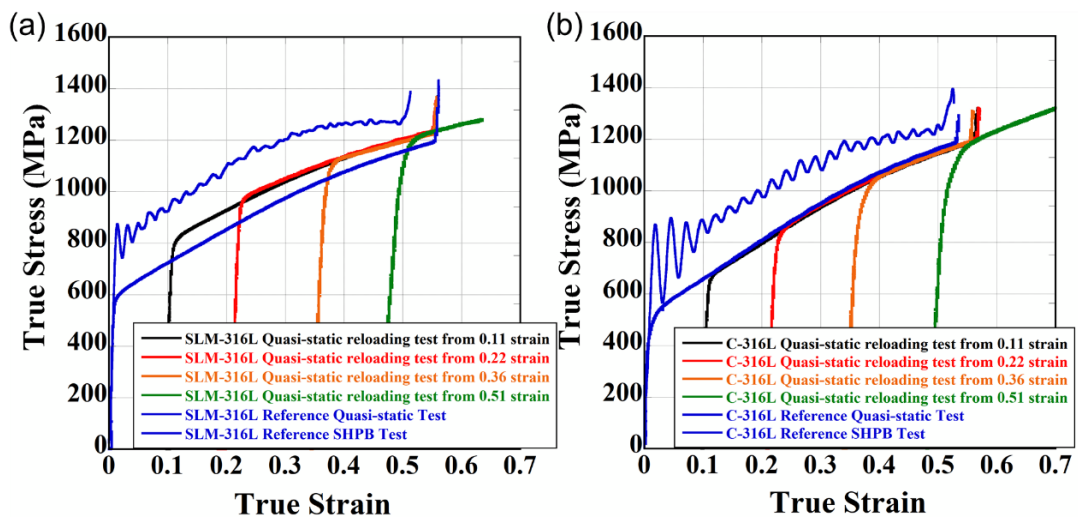


Figure 4.33. Quasi-static reloading tests of previously SHPB tested (a) SLM-316L and (b) C-316L specimens.

## CHAPTER 5

### CONCLUSIONS

The compression stress-strain behavior of an SLM-316L alloy was determined x-axis (perpendicular to the building direction) between  $1 \times 10^{-3}$  and  $2500-3150 \text{ s}^{-1}$ . For comparison, annealed and extruded a C-316L alloy was also compression tested at the same strain rate interval. The undeformed and deformed microstructures of the tested SLM-316L and C-316L specimens were analyzed using optical microscope, SEM, EBDS and XRD. The martensite content of the undeformed and deformed C-316L specimens was calculated using Rietveld method.

The average densities of SLM-316L and C-316L were sequentially  $7821 \pm 5 \text{ kg m}^{-3}$  and  $7838.5 \pm 5 \text{ kg m}^{-3}$ . The percent porosity in SLM-316L was calculated 0.22. The XRD spectra of the untested specimens of SLM-316L and C-316L confirmed a fully austenitic phase in both alloys, while the compression tested C-316L specimen exhibited martensite phase because of TRIP deformation behavior.

The microscopic analysis of SLM-316L revealed a strong  $\langle 110 \rangle$  fiber texture orientation along the building direction (the loading axis of  $0^\circ$  inclined specimens) and a weak  $\langle 111 \rangle$  texture or nearly random distribution of directions in the perpendicular to the building direction. The use of rotation scanning strategy resulted in a mismatch in the positions of melt layers and led to the development of interrupted grains. The average width of the columnar grains was 20-50  $\mu\text{m}$ . Within the melt pools inside the columnar-like grains, a cellular microstructure/sub-structure development in 0.7-1  $\mu\text{m}$  size was found. The sub-grains resembled 5–6-sided honeycomb-like structure and were oriented in-plane and out of plane inside the columnar grains. The average grains size of C-316L was found 24.3  $\mu\text{m}$ .

SLM-316L was found to have a higher average hardness ( $\sim 2300 \text{ MPa}$ ) than C-316L ( $\sim 2100 \text{ MPa}$ ). The higher hardness of SLM-316L was attributed to higher dislocation density calculated using the Williamson and Hall method ( $1.04 \times 10^{15} \text{ m}^{-2}$ ). SLM-316L specimens also exhibited a higher hardness in the z-direction than in perpendicular to the z-direction. This anisotropy was probably due to size and morphological differences in microstructure resulting from the scanning strategy.

Moreover, a higher hardness was found near to supports in the SLM-316L specimen, because of the faster cooling near to the support. Hardness test was also applied to SLM-316L specimens manufactured with higher and lower laser power in similar grain sizes but different sub-grain sizes.

In the quasi-static tests, both SLM-316L and C-316L showed high ductility; no fracture was observed until about 0.51 strain. SLM-316L had a higher quasi-static yield strength (510 MPa) than C-316L (360 MPa). While the work hardening rate of the C-316L alloy was higher at low strains and reached the same work hardening rate as the SLM-316L as the strain increased. The high work hardening of C-316L than SLM-316L was ascribed to the higher resistance of martensite plate than twin boundary to the dislocation motion. This was confirmed by applying hardness tests on the twin and martensite formed sections of the deformed specimens.

Both alloys showed strain rate sensitive flow stresses. As the strain rate increased, flow stress increased. Due to the more formation of dislocation slip at high strain rates in the SLM-316L alloys, SLM-316L was found to be slightly more strain rate sensitive than the C-316L. The rate sensitivities of both alloys however declined as the strain increased. This was attributed to the adiabatic heating of the specimens tested in the SHPB. Using the quasi-static and dynamic strain rate compression stress-strain curves, the JC flow stresses of both alloys were determined at the adiabatic condition and then both were converted for the isothermal condition.

Extensive microscopic observations showed that tested SLM-316L deformed dominantly by twinning and slip similar to TWIP steels, while C-316L by martensitic transformation and slip similar to TRIP steel. As the strain increased, the amount of martensite and deformation twins increased in the C-316L and SLM-316L alloys, respectively. The distance between twins was in an order of 100 nm, which was less than the intercellular cell size (0.7-1  $\mu\text{m}$ ) in SLM-316L. Twins were continuously divided cell size, inducing an increasing effect of cell size on the flow stress. On the other hand, the martensite formation in C-316L specimens and twinning formation in SLM-316L alloys decreased at high strain rates compared to quasi-static strain rates. The XRD spectra of C-316L also confirmed the reduced martensite formation at high strain rates. The reduced twin and martensite formation at high strain rates were attributed to the increased SFE due to the adiabatic heating of the test specimens. The increase of SFE at high strain rates promoted a higher fraction of the deformation by slip. Lastly, the reloading tests revealed a strain rate history effect in SLM-316L and no strain rate history effect in C-316L.

## REFERENCES

1. Peckner, D.; Bernstein, I. M.; Peckner, D., *Handbook of stainless steels*. McGraw-Hill New York: 1977.
2. Lodhi, M.; Deen, K.; Greenlee-Wacker, M.; Haider, W., Additively manufactured 316L stainless steel with improved corrosion resistance and biological response for biomedical applications. *Addit. Manuf.* **2019**, *27*, 8-19.
3. Wohlers, T.; Gornet, T., History of additive manufacturing. *Wohlers report* **2014**, *24* (2014), 118.
4. Bourell, D. L.; Beaman, J. J.; Leu, M. C.; Rosen, D. W., A brief history of additive manufacturing and the 2009 roadmap for additive manufacturing: looking back and looking ahead. *Proceedings of RapidTech* **2009**, 24-25.
5. Dilberoglu, U. M.; Gharehpapagh, B.; Yaman, U.; Dolen, M., The role of additive manufacturing in the era of industry 4.0. *Procedia Manufacturing* **2017**, *11*, 545-554.
6. Dehghanghadikolaei, A.; Namdari, N.; Mohammadian, B.; Fotovvati, B., Additive manufacturing methods: a brief overview. *J. Sci. Eng. Res* **2018**, *5*, 123-131.
7. Song, B.; Zhao, X.; Li, S.; Han, C.; Wei, Q.; Wen, S.; Liu, J.; Shi, Y., Differences in microstructure and properties between selective laser melting and traditional manufacturing for fabrication of metal parts: A review. *Frontiers of Mechanical Engineering* **2015**, *10* (2), 111-125.
8. Cao, Y. F.; Moumni, Z.; Zhu, J. H.; Zhang, Y. H.; You, Y. J.; Zhang, W. H., Comparative investigation of the fatigue limit of additive-manufactured and rolled 316 steel based on self-heating approach. *Eng. Fract. Mech.* **2020**, *223*, 11.
9. Ahmadi, A.; Mirzaeifar, R.; Moghaddam, N. S.; Turabi, A. S.; Karaca, H. E.; Elahinia, M., Effect of manufacturing parameters on mechanical properties of 316L stainless steel parts fabricated by selective laser melting: A computational framework. *Materials & Design* **2016**, *112*, 328-338.
10. Kumar, D.; Shankar, G.; Prashanth, K.; Suwas, S., Texture dependent strain hardening in additively manufactured stainless steel 316L. *Materials Science and Engineering: A* **2021**, 141483.
11. Liverani, E.; Toschi, S.; Ceschini, L.; Fortunato, A., Effect of selective laser melting (SLM) process parameters on microstructure and mechanical properties of 316L austenitic stainless steel. *J. Mater. Process. Technol.* **2017**, *249*, 255-263.
12. Marattukalam, J. J.; Karlsson, D.; Pacheco, V.; Beran, P.; Wiklund, U.; Jansson, U.; Hjörvarsson, B.; Sahlberg, M., The effect of laser scanning strategies on

- texture, mechanical properties, and site-specific grain orientation in selective laser melted 316L SS. *Materials & Design* **2020**, *193*, 108852.
13. Kneen, T. J.; Barrett, C.; Manogharan, G. P.; Carlson, P. R.; Dimon, J.; Conner, B. P., Mechanical behaviour and high strain rate deformation of stainless steel 316L processed by selective laser melting. *International Journal of Rapid Manufacturing* **2020**, *9* (1), 84-103.
  14. Li, Z.; Voisin, T.; McKeown, J. T.; Ye, J. C.; Braun, T.; Kamath, C.; King, W. E.; Wang, Y. M., Tensile properties, strain rate sensitivity, and activation volume of additively manufactured 316L stainless steels. *Int. J. Plast.* **2019**, *120*, 395-410.
  15. Parr, J. G.; Hanson, A.; Lula, R., *Stainless steel*. ASM: 1989.
  16. Davis, J. R., *Alloy digest sourcebook: stainless steels*. ASM international: 2000.
  17. Parr, J. G.; Hanson, A., An introduction to stainless steel. *1965, 147 P. American Society For Metals, Metals Park, OHIO 1966*.
  18. Bailey, A.; Merriman, A.; Elliott, A.; Basti, M. In *Preliminary testing of nanoparticle effectiveness in binder jetting applications*, 27th Annual International Solid Freeform Fabrication Symposium, 2016; pp 1069-1077.
  19. Gibson, I.; Rosen, D. W.; Stucker, B.; Khorasani, M., *Additive manufacturing technologies*. Springer: 2021; Vol. 17.
  20. Haghdad, N.; Laleh, M.; Moyle, M.; Primig, S., Additive manufacturing of steels: a review of achievements and challenges. *J. Mater. Sci.* **2021**, *56* (1), 64-107.
  21. Mercelis, P.; Kruth, J. P., Residual stresses in selective laser sintering and selective laser melting. *Rapid prototyping journal* **2006**.
  22. Lewandowski, J. J.; Seifi, M., Metal additive manufacturing: a review of mechanical properties. *Annual review of materials research* **2016**, *46*, 151-186.
  23. Fayazfar, H.; Salarian, M.; Rogalsky, A.; Sarker, D.; Russo, P.; Paserin, V.; Toyserkani, E., A critical review of powder-based additive manufacturing of ferrous alloys: Process parameters, microstructure and mechanical properties. *Materials & Design* **2018**, *144*, 98-128.
  24. Kim, T.; Ha, K.; Cho, Y. R.; Jeon, J. B.; Lee, W., Analysis of residual stress evolution during powder bed fusion process of AISI 316L stainless steel with experiment and numerical modeling. *Int. J. Adv. Manuf. Technol.* **2019**, *105* (1-4), 309-323.
  25. Bajaj, P.; Hariharan, A.; Kini, A.; Kürnsteiner, P.; Raabe, D.; Jäggle, E. A., Steels in additive manufacturing: A review of their microstructure and properties. *Materials Science and Engineering: A* **2020**, *772*, 138633.

26. Fang, Z.-C.; Wu, Z.-L.; Huang, C.-G.; Wu, C.-W., Review on residual stress in selective laser melting additive manufacturing of alloy parts. *Optics & Laser Technology* **2020**, *129*, 106283.
27. Yap, C. Y.; Chua, C. K.; Dong, Z. L.; Liu, Z. H.; Zhang, D. Q.; Loh, L. E.; Sing, S. L., Review of selective laser melting: Materials and applications. *Applied physics reviews* **2015**, *2* (4), 041101.
28. Astm, I., ASTM52900-15 standard terminology for additive manufacturing—general principles—terminology. *ASTM International, West Conshohocken, PA* **2015**, *3* (4), 5.
29. Murr, L. E.; Gaytan, S.; Ceylan, A.; Martinez, E.; Martinez, J.; Hernandez, D.; Machado, B.; Ramirez, D.; Medina, F.; Collins, S., Characterization of titanium aluminide alloy components fabricated by additive manufacturing using electron beam melting. *Acta Mater.* **2010**, *58* (5), 1887-1894.
30. Cunningham, R.; Zhao, C.; Parab, N.; Kantzos, C.; Pauza, J.; Fezzaa, K.; Sun, T.; Rollett, A. D., Keyhole threshold and morphology in laser melting revealed by ultrahigh-speed x-ray imaging. *Science* **2019**, *363* (6429), 849-852.
31. Pham, M. S.; Dovgyy, B.; Hooper, P. A., Twinning induced plasticity in austenitic stainless steel 316L made by additive manufacturing. *Mater. Sci. Eng. A-Struct. Mater. Prop. Microstruct. Process.* **2017**, *704*, 102-111.
32. Tan, C.; Zhou, K.; Ma, W.; Attard, B.; Zhang, P.; Kuang, T., Selective laser melting of high-performance pure tungsten: parameter design, densification behavior and mechanical properties. *Science and Technology of advanced MaTeriaLS* **2018**, *19* (1), 370-380.
33. Pauzon, C.; Hryha, E.; Foret, P.; Nyborg, L., Effect of argon and nitrogen atmospheres on the properties of stainless steel 316 L parts produced by laser-powder bed fusion. *Materials & Design* **2019**, *179*, 10.
34. Zhang, X.; Yocom, C. J.; Mao, B.; Liao, Y., Microstructure evolution during selective laser melting of metallic materials: A review. *Journal of Laser Applications* **2019**, *31* (3), 031201.
35. Gorsse, S.; Hutchinson, C.; Gouné, M.; Banerjee, R., Additive manufacturing of metals: a brief review of the characteristic microstructures and properties of steels, Ti-6Al-4V and high-entropy alloys. *Science and Technology of advanced MaTeriaLS* **2017**, *18* (1), 584-610.
36. Pham, M.-S.; Hooper, P. In *Roles of microstructures on deformation response of 316 stainless steel made by 3D printing*, AIP Conference Proceedings, AIP Publishing LLC: 2017; p 040017.

37. Yin, Y. J.; Sun, J. Q.; Guo, J.; Kan, X. F.; Yang, D. C., Mechanism of high yield strength and yield ratio of 316 L stainless steel by additive manufacturing. *Mater. Sci. Eng. A-Struct. Mater. Prop. Microstruct. Process.* **2019**, *744*, 773-777.
38. Wang, X. L.; Muniz-Lerma, J. A.; Shandiz, M. A.; Sanchez-Mata, O.; Brochu, M., Crystallographic-orientation-dependent tensile behaviours of stainless steel 316L fabricated by laser powder bed fusion. *Mater. Sci. Eng. A-Struct. Mater. Prop. Microstruct. Process.* **2019**, *766*, 16.
39. Wang, Y. M.; Voisin, T.; McKeown, J. T.; Ye, J.; Calta, N. P.; Li, Z.; Zeng, Z.; Zhang, Y.; Chen, W.; Roehling, T. T.; Ott, R. T.; Santala, M. K.; Depond, Philip J.; Matthews, M. J.; Hamza, A. V.; Zhu, T., Additively manufactured hierarchical stainless steels with high strength and ductility. **2017**, Medium: X; Size: 63-71.
40. Zhong, Y.; Liu, L.; Wikman, S.; Cui, D.; Shen, Z., Intragranular cellular segregation network structure strengthening 316L stainless steel prepared by selective laser melting. *Journal of Nuclear Materials* **2016**, *470*, 170-178.
41. Saeidi, K.; Gao, X.; Zhong, Y.; Shen, Z. J., Hardened austenite steel with columnar sub-grain structure formed by laser melting. *Mater. Sci. Eng. A-Struct. Mater. Prop. Microstruct. Process.* **2015**, *625*, 221-229.
42. Sun, J. Y.; Zhao, Y.; Yang, L.; Zhao, X. F.; Qu, W. R.; Yu, T. B., Effect of shielding gas flow rate on cladding quality of direct laser fabrication AISI 316L stainless steel. *J. Manuf. Process.* **2019**, *48*, 51-65.
43. Andreau, O.; Koutiri, I.; Peyre, P.; Penot, J.-D.; Saintier, N.; Pessard, E.; De Terris, T.; Dupuy, C.; Baudin, T., Texture control of 316L parts by modulation of the melt pool morphology in selective laser melting. *J. Mater. Process. Technol.* **2019**, *264*, 21-31.
44. Sun, Z.; Tan, X.; Tor, S. B.; Chua, C. K., Simultaneously enhanced strength and ductility for 3D-printed stainless steel 316L by selective laser melting. *NPG Asia Materials* **2018**, *10* (4), 127-136.
45. Niendorf, T.; Leuders, S.; Riemer, A.; Brenne, F.; Tröster, T.; Richard, H. A.; Schwarze, D., Functionally graded alloys obtained by additive manufacturing. *Advanced engineering materials* **2014**, *16* (7), 857-861.
46. Niendorf, T.; Leuders, S.; Riemer, A.; Richard, H. A.; Tröster, T.; Schwarze, D., Highly anisotropic steel processed by selective laser melting. *Metallurgical and Materials Transactions B* **2013**, *44* (4), 794-796.
47. Zhong, Y. Sub-grain structure in additive manufactured stainless steel 316L. Department of Materials and Environmental Chemistry, Stockholm University, 2017.

48. Ishimoto, T.; Wu, S.; Ito, Y.; Sun, S.-H.; Amano, H.; Nakano, T., Crystallographic orientation control of 316L austenitic stainless steel via selective laser melting. *ISIJ International* **2020**, *60* (8), 1758-1764.
49. Ma, M. M.; Wang, Z. M.; Zeng, X. Y., A comparison on metallurgical behaviors of 316L stainless steel by selective laser melting and laser cladding deposition. *Mater. Sci. Eng. A-Struct. Mater. Prop. Microstruct. Process.* **2017**, *685*, 265-273.
50. Montero-Sistiaga, M. L.; Godino-Martinez, M.; Boschmans, K.; Kruth, J. P.; Van Humbeeck, J.; Vanmeensel, K., Microstructure evolution of 316L produced by HP-SLM (high power selective laser melting). *Addit. Manuf.* **2018**, *23*, 402-410.
51. Hong, Y.; Zhou, C.; Zheng, Y.; Zhang, L.; Zheng, J.; Chen, X.; An, B., Formation of strain-induced martensite in selective laser melting austenitic stainless steel. *Materials Science and Engineering: A* **2019**, *740*, 420-426.
52. Zhang, Y. Z.; Wang, J. J.; Tao, N. R., Tensile ductility and deformation mechanisms of a nanotwinned 316L austenitic stainless steel. *J. Mater. Sci. Technol.* **2020**, *36*, 65-69.
53. Salman, O. O.; Brenne, F.; Niendorf, T.; Eckert, J.; Prashanth, K. G.; He, T.; Scudino, S., Impact of the scanning strategy on the mechanical behavior of 316L steel synthesized by selective laser melting. *J. Manuf. Process.* **2019**, *45*, 255-261.
54. Meyers, M. A.; Chawla, K. K., *Mechanical behavior of materials*. Cambridge university press: 2008.
55. Rahman, K. M. Mechanical Behaviour of Twinning Induced Plasticity (TWIP) Steels. Imperial College London, 2013.
56. Solomon, N.; Solomon, I., Deformation induced martensite in AISI 316 stainless steel. *Rev. Metal.* **2010**, *46* (2), 121-128.
57. Pozuelo, M.; Wittig, J.; Jiménez, J. A.; Frommeyer, G., Enhanced mechanical properties of a novel high-nitrogen Cr-Mn-Ni-Si austenitic stainless steel via TWIP/TRIP effects. *Metallurgical and Materials Transactions A* **2009**, *40* (8), 1826-1834.
58. Remy, L.; Pineau, A., Twinning and strain-induced fcc→ hcp transformation on the mechanical properties of Co · Ni · Cr · Mo alloys. *Materials Science and Engineering* **1976**, *26* (1), 123-132.
59. Dash, J.; Otte, H., The martensite transformation in stainless steel. *Acta Metallurgica* **1963**, *11* (10), 1169-1178.
60. Withers, P. J.; Bhadeshia, H., Residual stress. Part 2–Nature and origins. *Mater. Sci. Technol.* **2001**, *17* (4), 366-375.

61. Mendelson, S., The Kurdjumov-Sachs, Bogers-Burgers, Nishiyama, and Zener models for martensite formation in FCC → BCC. *Scripta Metallurgica* **1977**, *11* (5), 375-382.
62. Christian, J. W.; Mahajan, S., Deformation twinning. *Progress in materials science* **1995**, *39* (1-2), 1-157.
63. Reed-Hill, R. E., *Physical Metallurgy Principles*. D Van Nostrand Company: Princeton, 1964.
64. Cottrel, A., *Dislocations and Plastic Flow in Crystals*. Oxford University Press: 1953.
65. Byun, T. S.; Hashimoto, N.; Farrell, K., Temperature dependence of strain hardening and plastic instability behaviors in austenitic stainless steels. *Acta Mater.* **2004**, *52* (13), 3889-3899.
66. Karaman, I.; Sehitoglu, H.; Gall, K.; Chumlyakov, Y. I., On the deformation mechanisms in single crystal Hadfield manganese steels. *Scripta materialia* **1998**, *38* (6), 1009-1015.
67. Kireeva, I.; Chumlyakov, Y. I.; Pobedennaya, Z.; Kuksgausen, I.; Karaman, I., Orientation dependence of twinning in single crystalline CoCrFeMnNi high-entropy alloy. *Materials Science and Engineering: A* **2017**, *705*, 176-181.
68. Eleiche, A. M.; Albertini, C.; Montagnani, M., The Influence Of Strain-Rate History On The Ambient Tensile-Strength Of Aisi Type-316 Stainless-Steel. *Nucl. Eng. Des.* **1985**, *88* (2), 131-141.
69. Langdon, G. S.; Schleyer, G. K., Unusual strain rate sensitive behaviour of AISI 316L austenitic stainless steel. **2004**, *39* (1), 71-86.
70. Xue, Q.; Cerreta, E. K.; Gray, G. T., Microstructural characteristics of post-shear localization in cold-rolled 316L stainless steel. *Acta Mater.* **2007**, *55* (2), 691-704.
71. Xue, Q.; Gray, G. T., Development of adiabatic shear bands in annealed 316L stainless steel: Part I. Correlation between evolving microstructure and mechanical behavior. *Metallurgical and Materials Transactions A* **2006**, *37* (8), 2435-2446.
72. Lee, W.-S.; Chen, T.-H.; Lin, C.-F.; Luo, W.-Z., Dynamic Mechanical Response of Biomedical 316L Stainless Steel as Function of Strain Rate and Temperature %J Bioinorganic Chemistry and Applications. **2011**, *2011*, 13.
73. Lee, W.-S.; Lin, C.-F.; Chen, T.-H.; Luo, W.-Z., High temperature deformation and fracture behaviour of 316L stainless steel under high strain rate loading. *Journal of Nuclear Materials* **2012**, *420* (1), 226-234.

74. Lee, W.-S.; Lin, C.-F.; Liu, T.-J., Strain rate dependence of impact properties of sintered 316L stainless steel. *Journal of Nuclear Materials* **2006**, *359* (3), 247-257.
75. Bish, D. L.; Howard, S., Quantitative phase analysis using the Rietveld method. *Journal of Applied Crystallography* **1988**, *21* (2), 86-91.
76. Degen, T.; Sadki, M.; Bron, E.; König, U.; Nénert, G., The HighScore suite. *Powder Diffraction* **2014**, *29*, S13 - S18.
77. Suryanarayana, C.; Norton, M. G., *X-ray diffraction: a practical approach*. Springer Science & Business Media: 2013.
78. Williamson, G.; Smallman, R., III. Dislocation densities in some annealed and cold-worked metals from measurements on the X-ray debye-scherrer spectrum. *Philosophical magazine* **1956**, *1* (1), 34-46.
79. Beausir, B.; Fundenberger, J., Analysis Tools for Electron and X-ray diffraction. *ATEX-software, www. atex-software. eu, Université de Lorraine-Metz* **2017**.
80. Standard, A., ASTM E112-10: Standard Test Methods for Determining Average Grain Size. *ASTM International: West Conshohocken, PA, USA* **2010**.
81. Marattukalam, J. J.; Karlsson, D.; Pacheco, V.; Beran, P.; Wiklund, U.; Jansson, U.; Hjorvarsson, B.; Sahlberg, M., The effect of laser scanning strategies on texture, mechanical properties, and site-specific grain orientation in selective laser melted 316L SS. *Materials & Design* **2020**, *193*, 11.
82. Shamsujjoha, M.; Agnew, S. R.; Fitz-Gerald, J. M.; Moore, W. R.; Newman, T. A., High Strength and Ductility of Additively Manufactured 316L Stainless Steel Explained. *Metall. Mater. Trans. A-Phys. Metall. Mater. Sci.* **2018**, *49A* (7), 3011-3027.
83. He, B. B.; Hu, B.; Yen, H. W.; Cheng, G. J.; Wang, Z. K.; Luo, H. W.; Huang, M. X., High dislocation density-induced large ductility in deformed and partitioned steels. *Science* **2017**, *357* (6355), 1029-1032.
84. Morito, S.; Nishikawa, J.; Maki, T., Dislocation Density within Lath Martensite in Fe-C and Fe-Ni Alloys. *ISIJ International* **2003**, *43* (9), 1475-1477.
85. Hadfield, R. A., Some Newly Discovered Properties Of Iron And Manganese. *Minutes of the Proceedings of the Institution of Civil Engineers* **1888**, *93* (1888), 61-75.
86. Rémy, L.; Pineau, A., Twinning and strain-induced f.c.c. → h.c.p. transformation on the mechanical properties of Co · Ni · Cr · Mo alloys. *Materials Science and Engineering* **1976**, *26* (1), 123-132.
87. Woo, W.; Jeong, J. S.; Kim, D. K.; Lee, C. M.; Choi, S. H.; Suh, J. Y.; Lee, S. Y.; Harjo, S.; Kawasaki, T., Stacking Fault Energy Analyses of Additively

- Manufactured Stainless Steel 316L and CrCoNi Medium Entropy Alloy Using In Situ Neutron Diffraction. *Sci Rep* **2020**, *10* (1), 15.
88. Conrad, H.; Wiedersich, H., Activation energy for deformation of metals at low temperatures. *Acta Metallurgica* **1960**, *8* (2), 128-130.
  89. Mahajan, S.; Williams, D. F., Deformation Twinning in Metals and Alloys. *International Metallurgical Reviews* **1973**, *18* (2), 43-61.
  90. Meyers, M. A.; Chawla, K. K., *Mechanical Behavior of Materials*. Cambridge University Press 2009.
  91. Meyers, M. A.; Vöhringer, O.; Lubarda, V. A., The onset of twinning in metals: a constitutive description. *Acta Mater.* **2001**, *49* (19), 4025-4039.
  92. Li, Y. Z.; Huang, M. X., Carbon-Dislocation Interaction-Induced Abnormal Strain-Rate Sensitivity in Twinning-Induced Plasticity Steels. *Metall. Mater. Trans. A-Phys. Metall. Mater. Sci.* **2019**, *50A* (6), 2570-2575.
  93. E.D.H. Davies; Hunter, S. C., The dynamic compression testing of solids by the method of the split Hopkinson pressure bar. *Journal of the Mechanics and Physics of Solids* **1963**, *11* (3), 155-179.
  94. Kolsky, H., An Investigation of the Mechanical Properties of Materials at very High Rates of Loading. *Proceedings of the Physical Society. Section B* **1949**, *62* (11), 676.
  95. De Cooman, B. C.; Estrin, Y.; Kim, S. K., Twinning-induced plasticity (TWIP) steels. *Acta Mater.* **2018**, *142*, 283-362.
  96. Soleimani, M.; Kalhor, A.; Mirzadeh, H., Transformation-induced plasticity (TRIP) in advanced steels: a review. *Materials Science and Engineering: A* **2020**, 140023.
  97. Shen, Y.; Jia, N.; Misra, R.; Zuo, L., Softening behavior by excessive twinning and adiabatic heating at high strain rate in a Fe–20Mn–0.6 C TWIP steel. *Acta Mater.* **2016**, *103*, 229-242.
  98. Johnson, G. R.; W.H., C. In *A constitutive model and data for metals subjected to large strains, high strain rates and high temperatures* Proceedings of the 7th International Symposium on Ballistics, The Hague, The Netherlands, The Hague, The Netherlands, 1983; p 541.
  99. Karkalos, N. E.; Markopoulos, A. P., Determination of Johnson-Cook material model parameters by an optimization approach using the fireworks algorithm. *Procedia Manufacturing* **2018**, *22*, 107-113.
  100. Khodabakhshi, F.; Farshidianfar, M. H.; Gerlich, A. P.; Nosko, M.; Trembošová, V.; Khajepour, A., Microstructure, strain-rate sensitivity, work hardening, and fracture behavior of laser additive manufactured austenitic and

- martensitic stainless steel structures. *Materials Science and Engineering: A* **2019**, 756, 545-561.
101. Ham, G.-S.; Lee, K.-A.; Park, S.-H., Room and Elevated Temperature Compressive Deformation Behavior of AISI 316L Alloy Fabricated by Selective Laser Melting Process. *Journal of the Korean Institute of Metals and Materials* **2019**, 57 (5), 295-303.
  102. Taylor, G. I.; Quinney, H., The Latent Energy Remaining in a Metal after Cold Working. **1934**, 143 (849), 307-326.
  103. Samuel, K. G.; Mannan, S. L.; Radhakrishnan, V. M., The influence of temperature and prior cold work on the strain-hardening parameters of a type 316 LN stainless steel. *International Journal of Pressure Vessels and Piping* **1992**, 52 (2), 151-157.
  104. Vazquez-Fernandez, N.; Soares, G.; Smith, J.; Seidt, J.; Isakov, M.; Gilat, A.; Kuokkala, V.; Hokka, M., Adiabatic Heating of Austenitic Stainless Steels at Different Strain Rates. *Journal of Dynamic Behavior of Materials* **2019**, 5 (3), 221-229.
  105. Rittel, D.; Zhang, L. H.; Osovski, S., The dependence of the Taylor–Quinney coefficient on the dynamic loading mode. *Journal of the Mechanics and Physics of Solids* **2017**, 107, 96-114.
  106. Venables, J. A., Deformation twinning in face-centred cubic metals. *The Philosophical Magazine: A Journal of Theoretical Experimental and Applied Physics* **1961**, 6 (63), 379-396.
  107. Idrissi, H.; Renard, K.; Ryelandt, L.; Schryvers, D.; Jacques, P. J., On the mechanism of twin formation in Fe–Mn–C TWIP steels. *Acta Mater.* **2010**, 58 (7), 2464-2476.
  108. Conrad, H., Thermally activated deformation of metals. *JOM* **1964**, 16 (7), 582-588.
  109. Kocks, U. F.; Argon, A. S.; Ashby, M. F.; Chalmers, B.; Christian, J. W.; Massalski, T. B., *Progress in materials science. Vol. 19, Vol. 19*. Pergamon: Oxford (etc.), 1975.
  110. Lindholm, U., Some experiments with the split hopkinson pressure bar\*. *Journal of the Mechanics and Physics of Solids* **1964**, 12 (5), 317-335.